Isotopic Investigations of Meteoritic Materials:

From Earliest-Formed Solids to Planetary Bodies

by

Prajkta Mane

A Dissertation Presented in Partial Fulfillment
of the Requirements for the Degree
Doctor of Philosophy

Approved September 2016 by the
Graduate Supervisory Committee:

Meenakshi Wadhwa, Chair
Richard Hervig
Steven Desch
James Bell III
Laurence Garvie

ARIZONA STATE UNIVERSITY

December 2016

ABSTRACT

The beginning of our Solar System, including events such as the formation of the first solids as well as the accretion and differentiation of planetary bodies, is recorded in meteoritic material. This record can be deciphered using petrographic, geochemical and isotopic investigations of different classes of meteorites and their components. In this dissertation, I have investigated a variety of isotope systematics in chondritic and achondritic meteorites to understand processes that have shaped our Solar System. Specifically, the investigations conducted here are in two main areas: 1) Hydrogen isotope systematics in a meteorite representing the freshest known sample of the martian crust, and 2) Isotopic studies (specifically relating to high resolution chronology, nucleosynthetic anomalies and mass-dependent fractionations) in calcium-aluminum-rich inclusions, which are thought to be the earliest-formed solids in the Solar System. Chapter 1 of this dissertation presents a review of the hydrogen isotopic compositions of various planetary bodies and reservoirs in the Solar System, which could serve as tracers for the volatile sources. Chapter 2 focuses on an investigation of the hydrogen isotopic systematics in the freshest martian meteorite fall, Tissint, using the Cameca IMS-6f secondary ion mass spectrometer (SIMS). These first two chapters comprise the first part of this dissertation. The second part is comprised of chapters 3 through 6 and is focused on isotopic analyses of Calcium-Aluminum-rich Inclusions (CAIs). Chapter 3 is a review of CAIs, which record some of the earliest processes that occurred in the solar nebula. Chapter 4 presents the results of an investigation of the ^{26}Al-^{26}Mg short-lived chronometer (half-life ~0.72 Ma) in two CAIs and their Wark-Lovering (WL) rims from a CV3 carbonaceous chondrite using the Cameca NanoSIMS 50L. Chapter 5 is focused on the results of a study of the Zr isotope compositions of a suite of 15 CAIs from different carbonaceous chondrites

using multicollector inductively coupled plasma mass spectrometry (MC-ICPMS), in order to identify nucleosynthetic anomalies in the CAI-forming region. Chapter 6 focuses on the mass-dependent Mg isotopic compositions measured in 11 CAIs from the Allende CV3 carbonaceous chondrite using MC-ICPMS, to evaluate effects of thermal processing on CAIs.

ACKNOWLEDGMENTS

This thesis work would not have been possible without the help and support of many individuals. First, I would like to thank my supervisory committee, in particular my advisor Meenkshi Wadhwa for her mentoring me. I have learned counteless things under her apprenticeship within last five years that have made me a better scientist. I am deeply grateful to Rick Hervig for introducing me to the SIMS instrument and training me to experiment with this wonderful tool that turned out to be essential for my research work. I would like to thank Steve Desch for many discussions that helped me develope the understanding of astrophysical implications of my research. I would like to thank Laurence Garvie for his guidance to improve my scientific writing skills and for his contagious enthusiasm and curiosity towards scientific research, which encouraged me through out my PhD. I am grateful to Jim Bell for his encouragement to think about bigger implications of my research.

I would also like to thank Phil Janney, Kate Souders, Steve Romaniello, Vinai Rai and Rebekah Hines for all their help in the ICGL lab, as well as Maitrayee Bose, and Lynda Williams for their assistance in the NanoSIMS and SIMS lab. I have been fortunate to have a great group of friends and colleagues in the Center for Meteorite Studies and the School of Earth and Exploration including Matt Sanborn, Greg Brennecka, Curtis Williams, Karen Rieck, Daniel Dunlap, Emilie Dunham, Zack Torrano, Alice Stephant, Cameron Mercer, Kim Ward-Duong, Julie Mitchell and many more. Thank you all for countless scientific and non-scientific discussions, friendships and support that made my graduate school experience memorable. Finally, I would like to thank my family, friends and teachers back home, especially my mother, for all the encouragement and support to pursue my professional interests.

TABLE OF CONTENTS

LIST OF TABLES

LIST OF FIGURES

CHAPTER 1

HYDROGEN ISOTOPIC SYSTEMATICS IN THE SOLAR SYSTEM MATERIAL

1.1 Introduction

Hydrogen is the most abundant element in the Universe. It is also the element with the largest relative isotopic mass difference ratio (Δm/m), which leads to the largest isotopic fractionation effects observed for any element during chemical and physical reactions. Hydrogen was formed during primordial nucleosynthesis, i.e., during the first few minutes after the Big Bang (Alpher et al., 1948). As deuterium is destroyed during stellar nucleosynthesis to create heavier elements, the D/H ratio progressively should decrease along with the metal abundances over time in the universe (e. g., Linsky, 2002). On a modern galactic scale, accurate measurements of the deuterium to hydrogen (i.e., D/H) ratio are important to test the validity of assumptions of galactic chemical evolution models.

On a planetary scale D/H ratio is an indicator of sources of volatiles on different planetary bodies. Dynamic models of Solar System formation suggest that water accreted beyond ~1 to 5 AU (e.g., Morbidelli et al., 2000), causing depletion of water in the inner Solar System. The terrestrial planets accreted in this region would be depleted in water whereas giant planets would be enriched in water. The giant planets show a heliocentric gradient in their D/H signature (Figure 4), with Jupiter's D/H ratio very close to the solar value (Geiss and Gloeckler, 1998). However, the bulk terrestrial planets, although being closer to the sun have much higher D/H ratio (e.g., the bulk earth = ~ $(1.49 \pm 0.03) \times 10^{-4}$; Lécuyer et al., 1998), therefore the volatile reservoirs of the terrestrial planets may have been delivered later by comets and asteroids, containing volatiles with high D/H ratios (e.g., Alexander et al 2012; Morbidelli et al., 2000). The hydrogen isotopic compositions of comets and primitive meteorites parent bodies can be used to identify the potential provenance of volatiles

on terrestrial planets (Robert, 2000). For example, one of the recent dynamic models ('the Grand Tack model') suggests first inward and then outward migration of Jupiter, causing first depletion of the asteroidal belt and later refilling it with scattered asteroids, including some trans-Neptunian objects (Walsh et al., 2012). Since CI chondrites have D/H ratio higher than Neptune, they are thought to be trans-Neptunian objects and as their D/H ratio is very close to that of the Earth, they are predicted to be the primary source of water on the Earth (Alexander et al., 2012).

After planetary accretion and differentiation, various atmospheric processes that can alter D/H ratios of a planetary body also cause a remarkable diversity in planetary atmospheres in our Solar System. For example, Venus and Earth have comparable sizes, however Earth's atmosphere is nitrogen-rich whereas Venus has a thick carbon dioxide-rich atmosphere, resulting in a huge greenhouse effect. The Jovian moon Callisto and Saturnine moon Titan are similar in their sizes; however, Titan has a thick nitrogen-rich atmosphere, and is considered potentially hospitable for life, whereas Callisto is essentially airless. The composition and evolution of a planetary atmosphere could be indicators of the habitability of that planet. Processes that determine the fate of planetary atmospheres also affect the isotopic ratios of the gaseous species present in these atmospheres. The hydrogen isotopic composition of a planetary atmosphere can serve as a key indicator for such processes, and hence may be used to understand the conditions for habitability (e.g., Catling and Zahnle, 2009).

The hydrogen isotopic system can be applied towards understanding a variety of galactic- to planetary-scale processes. In this review chapter, sections 1.2 and 1.3 include discussions of our current understanding of galactic and solar D/H ratios. Section 1.4 discusses various processes that can fractionate hydrogen isotopes in

planetary reservoirs and environments. Section 1.5 summarizes the current state of knowledge of D/H ratios in different planetary bodies and planetary materials based on remote observations or sample analyses.

1.2 Galactic D/H ratio

Determining the primordial D/H (i.e., soon after the Big Bang) is important since it would constrain the density of baryons in the first 100 to 1000 seconds of the universe, therefore testing assumptions of theories regarding the Big Bang and nucleosynthesis (e.g., Burles et al., 2001). The best place to measure this value would be a cloud of gas where little star formation or chemical fractionation has taken place. However, finding such locations in the galaxy is very difficult (Linsky, 2002).

It is also important to determine the D/H ratio in different parts of the galaxy to test galactic chemical evolution models. As a galaxy evolves over time, stars form within molecular gas clouds, destroy deuterium and create heavier elements ('metals'). As stars die, they return the D-poor and metal-rich material to the interstellar medium (by supernova explosions and winds). The rate of this process depends on various factors such as initial stellar mass, and is important for theoretical models of galactic chemical evolution. Determination of the D/H ratio in different parts of the galaxy can help to validate these theoretical models and their underlying assumptions (Linsky, 2002). Validation of the galactic chemical evolution models is important as they can then be used to predict the initial hydrogen isotopic composition of our solar nebula.

The hydrogen isotopic composition of our galaxy is unlikely to be homogenous. Various spectroscopic techniques (summarized by Linsky, 2002) estimate the D/H ratio of our galaxy to vary from 5×10^{-6} to 2.2×10^{-5} (See Appendix 1 for different

notations to express D/H ratio). The Far Ultraviolet Spectroscopic Explorer mission (FUSE, Moos et al., 2000) measured the D/H ratio of the gas in different regions of the galaxy. Within our galaxy, the Sun is located inside a region of a very low density called the 'local bubble'. The local bubble mainly consists of small clouds of warm ionized gas formed by winds and supernovae and extends 100-200 pc[1] from the Sun. FUSE measured the D/H for the gas in the local bubble to be 1.56×10^{-5}, but beyond the local bubble the D/H ratio varied by a factor of four (Linsky, 2007). One possible explanation for this variation is different rates of astration[2]. However, if astration were the cause of this variation, other metal abundances would be expected to correlate with the D/H ratio, but no such correlation was seen (Linsky, 2002). Draine (2006) proposed the 'deuterium depletion hypothesis' to explain this variation. According to this hypothesis, when the interstellar gas is allowed to cool for a long time, deuterium preferentially deposits on to dust grains. Local variations of D/H ratio may then be caused in recently shocked regions or regions near hot stars, where deuterium has evaporated back into the gas phase (Draine, 2006). Interplanetary dust particles, considered to be the representative of interstellar dust, analyzed in laboratories show significant deuterium enrichment (D/H = ~0.008; Messenger, 2000), which supports the deuterium depletion hypothesis.

Cold interstellar clouds show very high HDO/H_2O ratio ($\sim 10^{-3}$), as determined by UV spectra from the *Hubble Space Telescope* (HST) (Linsky, 2002). An important factor to note here is that water is present as ice in these clouds, in contrast to the gas measured by FUSE. This ratio is large because deuterated molecules are more tightly bound in ice crystals than non-deuterated ones. At cold temperatures this difference in binding energies results in large mass fractionation effects. Another

[1] pc (Parsec) is an astronomical unit of distance. 1 pc = 3.08×10^{13} km.

[2] Astration is defined as the incorporation of matter into a stellar interior during star formation, especially when referring to a specific element or isotope.

factor that can cause variation in the D/H ratio in the galaxy is photo-dissociation. H_2 molecules in the interstellar clouds are self-shielded compared to HD; therefore variation in fluxes of stellar and diffused UV photo-dissociates HD to different degrees (Linsky, 2002). In the nearby local interstellar medium (LISM), the D/H ratio has been measured to be $(1.6 \pm 0.2) \times 10^{-5}$ (Linsky et al., 1996).

1.3 Solar D/H ratio

Based on solar wind implantation on lunar soils, the solar D/H ratio is estimated to be $(2 \pm 0.4) \times 10^{-5}$, which is much lower than the value estimated for the bulk Earth (Geiss and Gloecker, 1998). Another estimate for solar D/H ratio $(2.1 \pm 0.5) \times 10^{-5,}$ comes from isotopic studies of primitive meteorites, where $^3He/^4He$ is used as a proxy for D/H, (described in more detail in Section 5.5). The solar D/H ratio is significantly lower than that of the bulk Earth ($(1.49 \pm 0.03) \times 10^{-4}$; Lécuyer et al., 1998), which implies that either the Earth did not accrete water directly from the solar nebula or/and various planetary processes, such as atmospheric loss, significantly changed the D/H ratio on the Earth.

1.4 Fractionation processes on planetary bodies

1.4.1 Atmospheric Loss Processes. Planetary bodies in our Solar System show large variation in atmospheric composition and density. It is evident that planetary bodies with atmospheres have undergone a variety of atmospheric loss processes (Catling and Zahnle, 2009), which can cause significant isotopic fractionation. These processes can be broadly classified into two types: thermal and non-thermal escape. Thermal escape is the most common process of atmospheric loss on planets like the Earth. There are two important thermal escape mechanisms by which loss of atmosphere occurs: hydrodynamic escape and Jeans escape.

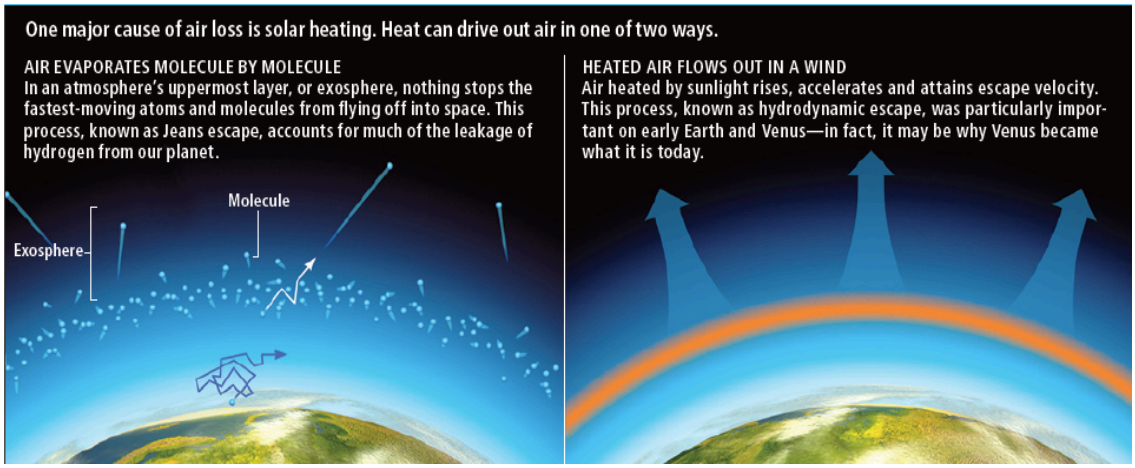

Figure 1.1. Two major processes of thermal escape. (Source: Catling & Zahnle, 2009)

1.4.1.1 Hydrodynamic Escape.

The UV radiation emitted by the Sun is absorbed by the uppermost layers of a planet's atmosphere, which expands in response. As the air molecules rise, they accelerate and some attain escape velocity. The lighter molecules like H_2 accelerate quickly, and they also drag heavier molecules like O_2 along with them. The heaviest molecular species that can be removed by this process is called the crossover mass. Hydrodynamic escape coupled with diffusion caused fractionation of hydrogen in the early history of the terrestrial planets (Hunten et. al., 1987; Pepin, 1991; Lammer et. al., 2008) (Figure 1.1).

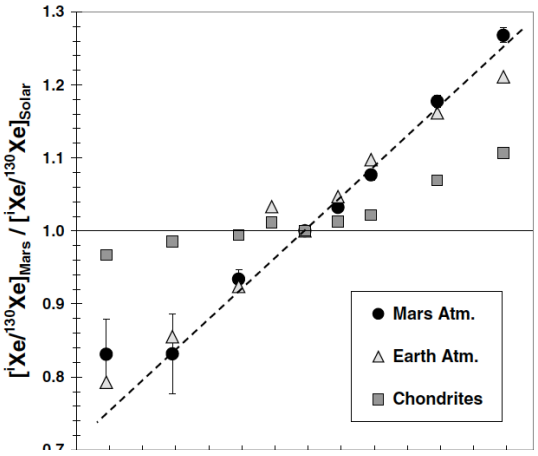

Figure 1.2. Isotopic fractionation of Xe in martian meteorites. Bogard et al., 2001)

Hydrodynamic escape requires a large source of energy and a hydrogen-rich atmosphere. Isotopic evidence suggests that early Earth, Mars, and Venus suffered significant atmospheric losses by this process, when the UV radiation from the young Sun was much more intense than

today. Hydrodynamic escape is the only process by which chemically unreactive nobles gases could fractionate (Jean's escape is effective for major species; noble gases usually makeup only a minor fraction of planetary atmospheres). Martian and terrestrial atmospheres show deficits of lighter isotopes of noble gases like Ne, Ar, and Xe, which are considered strong evidence of hydrodynamic escape in the early history of these planetary bodies (e.g., Bogard et al., 2001) (Figure 1.2).

1.4.1.2 Jeans Escape. Jean's escape is a thermal loss process where molecules are lost from the uppermost part of the atmosphere. This is a slow process, but it can cause significant isotopic mass fractionation over planetary timescales. This process is prevalent above an altitude called an 'exobase', above which the density of the air is so low that the air molecules hardly collide and can escape easily. However, below the exobase, the collisions between molecules confine them and keep them from escaping (Figure 1). This is the altitude where the scale height is equal to the mean free path of the gas molecules (Johnson, 2010). Scale height is defined as:

$$H = \frac{kT}{m_i g}$$

where k is Boltzmann's constant, T is the temperature, m_i the mass of the species and g is the gravitational acceleration and the mean free path defined as the average distance travelled by a particle between successive collisions.

At a given temperature, gas molecules will have a range of speeds (or energies) described by the Maxwell-Boltzmann distribution (described in Appendix 2). Molecules at the high-energy tail of the distribution will have higher velocities than the escape velocity of the planet ($\sqrt{(2GM/r)}$) and will escape the atmosphere. The rate of Jean's escape from a planetary atmosphere depends on the temperature

and strength of the gravitational field of that planetary body. Hydrogen being the lightest element reaches the exobase first and therefore escapes faster and is affected by this process significantly.

The escape velocities for Earth and Mars are 11.2 km/s and 5 km/s, respectively. Therefore Jeans escape is more efficient on Mars than on Earth. This process primarily affects major gases in the atmosphere and has little effect on the minor components. It is prevalent on present day Earth, Mars, and possibly Titan. However in Earth's atmosphere, most hydrogen exists as water vapor (H_2O). After being heated and evaporated, it condenses back in the form of rain. Other hydrogen-bearing species in the Earth's atmosphere include trace amounts of carbon dioxide and methane, and therefore only small amounts of hydrogen escape the Earth's atmosphere by Jean's escape (Catling and Zahnle, 2009).

Transition between hydrodynamic and Jeans escape depends on Jeans parameter (λ). It is defined as the ratio of gravitational to thermal energy of molecules in a planet's atmosphere.

$$\lambda = U_r/kT_r = r/H$$

Where U_r = molecule's gravitational energy at radius r

T_r = temperature at radius r

k = Boltzmann's constant

H = scale height (defined earlier; H = kT/mg)

For $\lambda > 2$, above the exobase of the planet, Jeans escape prevails, whereas if $\lambda \leq 2$, hydrodynamic escape is the efficient process for atmospheric loss (Hunten, 1982). The Jeans parameters for Earth, Mars and Venus are given in the Table 1.1

Table 1.1

Jeans parameter for H_2 for terrestrial planets (source: Chassefiere & Leblanc, 2004)

Planet	Exobase (km)	T at exobase (K)	λ_{ex}
Earth	500	1000	7.1
Venus	200	275	22.9
Mars	250	300	4.6

1.4.1.3 Non-thermal processes. Non-thermal escape processes are those during which chemical reactions or particle collisions cause escape of atmospheric gas molecules. Planetary magnetic fields play an important role in controlling escape rates of charged species since they usually keep charged species from escaping. The field lines for a planet with a magnetic field usually loop together at the pole; however, at higher latitudes they might remain open due to disturbance by solar wind and make the escape of charged species easier. In the case of Mars, in particular, it is easy to imagine that the loss of its magnetic field ~4 Ga ago (Connerney et al., 2001) was a non-thermal process that resulted in significant loss of charged species from its atmosphere.

Another type of non-thermal process is photochemical escape. In this process, air molecules are ionized by solar radiation; as they split or collide with each other, they gain enough velocity to escape the atmosphere. For planetary bodies without intrinsic magnetic fields, like Mars, sputtering is also an important non-thermal process where the exposed upper atmosphere is scooped away by solar wind.

Yet another significant process responsible for the loss of planetary atmospheres is impact erosion. As a projectile like an asteroid or a comet hits a planetary body, it vaporizes a significant mass from its surface. The hot plume of material then expands and rises faster than the escape velocity. Since it is a fast process, it may not be very significant for isotopic fractionation. However, during the Late Heavy Bombardment this process was likely very significant in stripping off the original atmospheres of planetary bodies and replacing them with secondary atmospheres (i.e., from volatiles brought in by comets) with different isotopic compositions. (Zahnle et al. 1998)

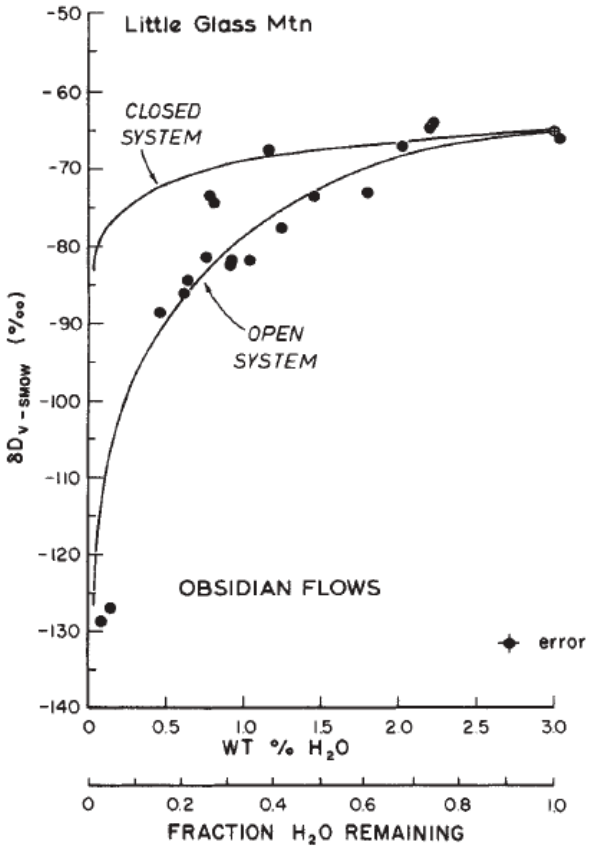

Figure 1.3. δD Vs water content in tephra from Little Glass Mountain. The solid lines show closed and open system Rayleigh fractionation curves for comparison. (Taylor et al., 1983)

1.4.2 Magmatic processes

processes. Hydrogen isotope systematics have been investigated in a variety of terrestrial igneous rock types to understand the origin and evolution of volatiles in their parent magmas. Magmatic degassing is an important process that can fractionate hydrogen isotopes (Taylor, 1986). One of the earliest attempts to understand the effects of degassing on hydrogen isotope composition of magmas was a study of rhyolitic glasses (obsidian), which showed a

correlation of δD with the water content (Figure 1.3) (Taylor et al., 1983). Similar but more detailed studies performed more recently on igneous rocks of basaltic to andesitic compositions from Indonesian arc basalts reveal that hydrogen isotopic fractionation depends on speciation of water in the magma (H_2O versus OH), water content of the magma and, to a lesser extent, temperature of the magma. Since these parameters are not constant during the degassing process, hydrogen isotopic fractionation is not constant. The δD values of these rocks vary from -109‰ to -57‰ (DeHoog et al., 2009). Open system degassing shows larger isotopic fractionation effects than closed system degassing, as seen in Figure 1.3.

1.4.3 Secondary alteration processes. Secondary alteration processes can affect the D/H ratios of rocks. When aqueous fluids are involved, one of the main factors affecting the D/H composition of the altered rocks is the composition of the fluids that cause the alteration. On Earth, these fluids are primarily seawater, meteoric water, juvenile water (primary magmatic water that has never been exposed to the surface), pore fluids, and sedimentary brines. The initial δD composition of these fluids is essential to understand the effects of secondary alteration processes on the hydrogen isotopic composition of the altered rocks. The δD composition of seawater can be directly measured and by definition is 0 ± 10 ‰ (see Appendix 1). The variation in δD of seawater in the past 2 Ga is estimated to be from -40 to 10‰ (Ohmoto et al 1983). The δD composition of meteoric water, based on analysis of clays is ~ 0‰ (Taylor 1979). The hydrogen isotope compositions of magmatic and juvenile waters, estimated from analyses of fluid inclusions, are -65 ± 20 ‰ (Taylor, 1979). Sedimentary basin brines from oil fields show higher variation in δD, varying from -150 to +20 ‰. These fluids also characterized by higher salinities and temperatures (Clayton, 1979). Kazahaya and

Matsuo (1986) studied effects of salinity on H isotopic fractionation and saw variations of up to 10‰ in the temperature range of 150 – 300 °C.

When these isotopically different fluids interact with country rock, isotopic gradients are seen in hydrothermally altered rocks. These gradients have been extensively studied in volcanic rocks affected by meteoric and hydrothermal fluids and hydrothermal ore deposits (e.g., Ohmoto, 1986). The δD zonation is also used to quantify geochemical and hydrological parameters such as the minimum water/rock ratio (from the magnitude of variations), minimum mass of the fluids and size of the heat source (Ohmoto, 1983). An extensive study of oceanic sediments and shales (δD = ~ 5.5 ± 8.7‰) has shown that these sediments are in isotopic equilibrium with the ocean water (Savin and Epstein, 1970).

1.5 D/H ratios on other planetary bodies

Hydrogen isotopic composition of different solar system objects is summarized in Figure 1.4 Starting with Jupiter with D/H ratio very close to the solar value, giant planets show a gradient, where D/H ratio increases with increasing distance from the Sun. However terrestrial planets and carbonaceous chondrites have a higher D/H ratio.

1.5.1 Earth. Earth, being one of the most dynamic planets, shows a wide range in D/H ratios in different environments and geochemical reservoirs. Various physical, chemical and biological processes in Earth's lithosphere, atmosphere, hydrosphere and biosphere affect the hydrogen isotopic composition. Direct samples relating to different processes affecting the hydrogen isotopic composition are easily accessible on Earth. Therefore, analyses of appropriate samples recording various terrestrial processes are key to understanding the behavior of hydrogen isotopes

during such processes and provides the ability to compare to data obtained for other planetary bodies (by remote analyses or through sample return missions).

Based on D/H ratio of various terrestrial reservoirs and their contribution to terrestrial water inventory, the D/H ratio for the bulk earth is estimated to be (1.49 ± 0.03) × 10^{-4} (Lécuyer et al., 1998). This value is very close to the D/H of the carbonaceous chondrites (Alexander et al., 2012).

Figure 1.5 summarizes the δD composition of various terrestrial reservoirs. Earth's oceans have a δD value of 0, by definition. However, Earth's mantle is comparatively depleted in deuterium. This is primarily because early hydrodynamic escape and ongoing Jean's escape would have fractionated the atmosphere, enriching it in the heavier isotope. Since the terrestrial oceans are in equilibrium with the atmosphere, they reflect the hydrogen isotopic composition of the atmosphere. Sedimentary rocks show a larger range of δD, as they are affected by low

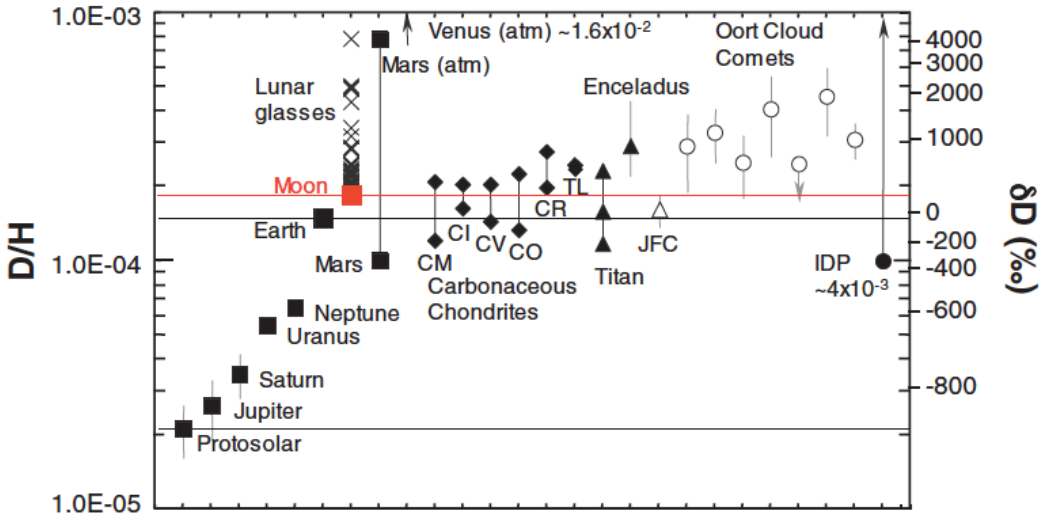

Figure 1.4. The hydrogen isotopic composition of the Solar System objects. Source: Saal et al., 2013; Data for proto-solar nebula and Jupiter: Geiss and Gloeckler, 1998; Titan: Abbas et al., 2010; Enceladus: Waite et al., 2009; Bulk Earth: Lécuyer et al., 1998; Mars: Hallis et al., 2012; Jupiter Family Comet: Hartogh et al., 2011; Oort cloud comets: Balsiger et al, 1995; Bockelée-Morvan et al., 1998; Meier et al., 1998; Biver et al., 2006; Hutsémekers et al., 2008; Villanueva et al., 2009 and IDPs: Messenger, 2010.

temperature chemical and physical processes that may have fractionated the hydrogen isotopes and altered their hydrogen isotopic composition. Biological processes on the Earth also contribute to D/H fractionation, but are not discussed here since they are beyond the scope of this paper.

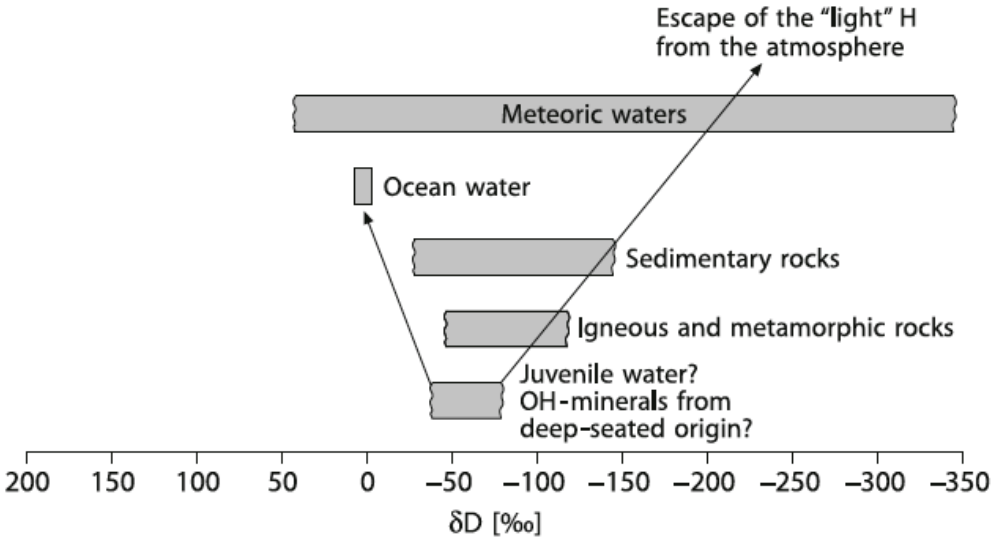

Figure 1.5. Hydrogen isotopic composition of different reservoirs on Earth. (Source: J. Hoefs, 2003)

1.5.1.2 Composition of Earth's mantle. The variation in δD shown above (from -125 to 0 ‰) has been attributed to three main processes by Kyser and O'Neil (1984); 1. degassing 2. addition of seawater at magmatic temperatures and 3. low temperature hydration of glasses.

Table 1.2

δD values for different terrestrial rock types derived from upper mantle sources

Rock-Type	***δD (‰)***	***References***
Primary Submarine basalts:	-70 to -80	Kyser and O'Neil 1984
Obsidian from Oceanic islands:	-80 ± 4	Sheppard and Harris, 1985
Hydrous minerals from xenoliths:	-95 to -65	Deloule et al 1991

Hydrous minerals from xenoliths (Hawaii):	-125	Deloule et al 1991
MORBs	-60	Clog et al 2013
Arc magmas:	-45 to -25	DeHoog et al 2009 (and references therein)
Ocean Island Basalts (Baffin Island)	<-218‰	Hallis et al 2015

These processes are especially effective for arc magmas near subduction zones, because there is a mixing of sediments and seawater with the magmas in these environments. Given that mantle-derived rocks typically have a δD value ~-70 ‰, and meteoric water has a δD of 0‰, it is difficult to explain the δD value of -125‰ for Hawaiian magmas. This suggests that there is heterogeneity in the Earth's mantle. Deloule et al. (1991) studied the variation in δD in a single pargasite grain (< 200μm) from a xenolith in a Hawaiian magma and reported that the mineral was zoned, with a δD value of -64‰ in the interior and -125‰ in the outer zones. Since meteoric waters in Hawaii have δD = ~ -5‰, this zoning cannot be explained by secondary alteration. This variation is explained in terms of multiple growth events separated by time and space and recording variation in mantle magmas (Deloule et al., 1991). Another study of southern pacific Mid Oceanic Ridge Basalts (MORBs) yielded a δD value of -60‰ for these upper mantle-derived rocks, which is 10-20 ‰, higher than previous reports and has been attributed to heterogeneity in the mantle (Clog et al., 2013). A more recent study of basalts from Baffin Island indicates much lighter D/H ratios for deep terrestrial mantle. Given the primordial nature of these rocks suggested by their high $^{3}He/^{4}He$ ratios, the lowest δD measured in these rocks -218‰, suggests that Earth's deep mantle may be lighter, inheriting volatiles with low D/H ratios, directly from the protosolar nebula (Hallis et al., 2015).

1.5.2 Moon. Until the last few years, analyses of the Apollo lunar samples had indicated that the Moon was essentially anhydrous. However, recent analyses of lunar volcanic glasses and apatites indicate that the Moon has a significant amount of indigenous water (McCubbin et al., 2010; Saal et al., 2008). Furthermore, the D/H ratio in the igneous apatites from Apollo samples shows significant variation (-215 to +1010 ‰; Greenwood et al., 2011). These apatites do not show any correlation of δD with water content; hence processes such as mixing, degassing, or diffusion cannot explain this variation. According to these authors, three main processes likely contributed to the variability in δD recorded in these apatites. Apatites from basalts from lunar highlands have δD values of +240 to +340 ‰, which are thought to be representative of the low δD mantle reservoir on the Moon. If the initial lunar mantle had a hydrogen isotopic composition similar to that of the Earth (Earth mantle δD = ~-70‰), hydrodynamic escape following the moon formation event could have elevated the primordial δD to +240‰. Cometary bombardment could be the source of the high δD component that would mix with the lunar mantle to provide higher values up to +1010‰. However, the low δD values (i.e., -215‰) in some apatites are primarily due to implantation of solar wind protons on lunar rocks that were further metamorphosed by impact processes, superimposing the solar wind signature over the initial δD.

Another recent study of Apollo samples and lunar meteorites showed that apatites in low-Ti lunar basalts have a large range of OH content but restricted δD values, whereas high-Ti basalts show a restricted range of OH content but a wider range in δD (Tartèse et al., 2013). The variation in δD seen in these apatites was interpreted by these workers to be a magma degassing effect. Specifically, high-Ti basalts that formed in reducing conditions outgassed H_2, and therefore have a restricted range in δD. In contrast, the low-Ti basalts outgassed hydrogen in the

form of H_2 followed by OH, producing a bigger range of δD. However, The initial hydrogen isotopic composition of the Moon has been estimated to be similar to that of the carbonaceous chondrites (Saal et al., 2013; Tartèse et al., 2013). Robinson et al., 2016 D/H ratios of the Moon.

1.5.3 Mars. The D/H ratios of reservoirs on Mars have been estimated from Earth-based telescopic observations, remote analyses by spacecraft (i.e., NASA's Mars Science Laboratory mission), as well as laboratory analyses of the martian meteorites (Figure 6).

Earth-based observations show that the martian atmosphere has an elevated D/H ratio that is ~5.2 times that of the Earth (Bjoraker et al., 1989). The D/H ratio of water in the present-day martian atmosphere varies as a function of latitude, peaking at a subsolar latitude (~50^0S) and decreasing towards the poles, but overall matches that of the higher values seen in the martian meteorites (Nowak et al., 2011). Recently, the SAM (Sample Analysis at Mars) instrument suite on the Mars Science Laboratory's Curiosity rover has also analyzed the isotopic composition of the martian atmosphere and of gases released from heating experiments on soils from the Rock Nest area; these data are in agreement with the D/H values estimated for the martian atmosphere and crustal rocks (Leshin et al., 2013; Webster et al., 2013) (Figure 6). The observed deuterium enrichment in the martian atmosphere is thought to be the result of loss of the martian atmosphere over geological timescales (e.g., Carr, 1990; Jakosky, 1990; Jakosky, 1991; Owen, 1992; Yung et al., 1988). The ubiquitous presence of valley networks (Bakers, 1982) and lake deposits (Squyres, 1989) on ancient martian terrains is evidence for the presence of surface water and of a thicker atmosphere in the early history of Mars. However, the present-day relatively dry conditions on Mars, with its thin CO_2-dominated atmosphere, suggest that a

significant quantity of volatiles were subsequently lost. NASA's MAVEN mission (Mars Atmosphere and Volatile EvolutioN Mission) specifically focuses on atmospheric loss processes on Mars and their early results suggest that interplanetary coronal mass ejection events may have resulted in an enhanced escape rate of ions to space and similar solar events early in martian history, likely contributing to the long-term evolution of the hydrogen isotope composition of the martian atmosphere (Chaffin et al., 2015; Jakosky et al., 2015). However, there are varied estimates of how much water was originally present in martian reservoirs, and questions relating to how and when this water may have been lost remain controversial.

Martian meteorites potentially provide a means of understanding the origin and evolution of the hydrologic cycle on Mars. The hydrogen isotopic composition of magmatic minerals in these meteorites can provide constraints on the initial composition of the primordial mantle reservoir, as well as on the process and timescales of volatile loss from this planet. Investigations of D/H ratios in minerals of the martian meteorites have shown that they record varying degrees of deuterium enrichment. (e.g., Leshin, 2000; Boctor et al., 2003; Greenwood et al., 2008; Hallis et al., 2012 and Usui et al., 2012) The proposed explanations for these observed variations in D/H ratios include: isotopic fractionation during degassing of the parent magma, fractionation during subsolidus diffusion of hydrogen, mixing between at least two distinct reservoirs having different H isotopic compositions, and varying degrees of terrestrial contamination. Isotopic fractionation during degassing of magma has been observed in terrestrial igneous rocks (e.g., De Hoog et al., 2009). However, mixing between distinct reservoirs is the favored explanation for the D/H variations in minerals of the martian meteorites since it is difficult to explain the large variations seen in their D/H ratios by other physical processes (e.g., Leshin, 2000; Boctor et al., 2003; Greenwood et al., 2008; Hallis et al., 2012 and Usui et al., 2012).

The mixing hypothesis requires at least two reservoirs with distinctly different D/H ratios. The end-member reservoir with the high D/H ratio is considered to be the crustal fluids that are in equilibrium with the atmosphere (which has a high D/H). Rocks interacting with this fluid reservoir would approach equilibrium with it and therefore will have high D/H. The other reservoir with the lower D/H ratio is thought to represent the martian mantle. Due to the cessation of plate tectonics in the early history of Mars (e.g., Sleep, 1994), crustal reservoirs will not be recycled into the mantle and therefore it is assumed that the martian mantle likely preserves its primordial hydrogen isotope composition. In situ analysis of impact glasses from some martian meteorites suggest an existence of water reservoir with intermediate D/H ratio (2-3 times D/H of earth's ocean water). This reservoir likely represents hydrated crust or ground ice inter-bedded with sediments (Usui et al., 2015). Sample Analysis on Mars (SAM) instrument on Curiosity rover analyzed D/H ratios of clay minerals from Hesparian era Gale crater sediments and these results also support a presence of intermediate D/H reservoir (Mahaffy et al., 2015). Constraints on the D/H value for the primordial martian mantle are important for inferring the ultimate source of water on Mars and the amount of water that has been lost from that planet through time.

1.5.4 Venus. There are no direct samples available from Venus for laboratory-based analyses of D/H ratios. However, spacecraft missions like Pioneer Venus Orbiter (1978) analyzed the hydrogen isotope composition of the Venusian atmosphere using the Large-probe Neutral Mass Spectrometer (LNMS). The D/H ratio of the Venusian atmosphere is 1.9×10^{-2}(McElroy et al 1982), which is 120 ± 40 times that of terrestrial value Based on these results, it was concluded that the planet had much more water in the past compared to the present-day abundance (200-300 ppm) in its atmosphere. Assuming present-day rate of hydrogen escape,

the initial water inventory on Venus was concluded to be at least ~0.3% of that represented by the terrestrial oceans (McElroy et al., 1982; Kulikov et al., 2006).

The initial water inventory and primordial D/H ratio of Venus remain controversial. There are two primary hypotheses that predict the early water inventory and loss of hydrogen. The first hypothesis predicts that since Venus accreted close to the Sun, it had much less abundant water than the Earth. Also, sputtering by energetic solar wind from the early young Sun would cause the early-unmagnetized Venus to lose its hydrogen. However, the CO_2 inventory of the planet should also be lost in this process, altering the carbon isotopic signature, but the carbon isotopic composition of Venus is comparable to that of the Earth. Therefore this phenomenon is unlikely (Kulikov et al., 2006). The second hypothesis predicts accretion of Venus with a comparable amount of water to Earth (Donahue et al., 1982). This substantial amount of water in the early history of Venus is required to explain the early onset of greenhouse effect, which is observed today. This is possible since during accretion, Venus may have captured icy planetismals from beyond the snowline. Another possibility is addition of water from comets. This leads to two different possibilities. The first is that early Venus had warm oceans on its surface, but that the runaway greenhouse effect changed the climate to extremely hot and dry. Alternatively, another scenario is the humid greenhouse effect where most of the water was present in the atmosphere in vapor phase, and hydrogen was lost by diffusion based hydrodynamic escape due to high X-ray and UV radiation (Kulikov et al., 2006).

One important observation is that the enrichment of the heavy isotopes seen in the hydrogen isotopic system is unique, as other elements like carbon, nitrogen, and oxygen show isotopic compositions for the Venusian atmosphere that are comparable to that of the Earth's atmosphere. Given that the hydrogen isotopic

system only has two stable isotopes, it does not allow one to differentiate between mass-independent and mass-dependent effects. Given this, and lacking D/H ratios for other crustal or mantle reservoirs on Venus, it limits the ability to infer the initial abundance of water and the primordial D/H ratio of this planet.

1.5.5 Jupiter. Jupiter, being a gas giant, is primarily made up of hydrogen (88-92%) and helium (8-12%) and is expected to reflect the composition of the solar nebula from which our solar system formed. An indirect method of determining the D/H ratio of the solar nebula (and therefore Jupiter) is to measure the $^{3}He/^{4}He$ ratio in the solar wind. The initial deuterium in the solar nebula (most of which was sequestered in the Sun) has been converted to ^{3}He by thermonuclear reactions. Therefore, the D/H ratio of the early solar nebula can be estimated using the following equation:

$$D/H_{SolarNebula} = (^{3}He/^{4}He_{SolarWind} - {}^{3}He/^{4}He_{SolarNebula}) \times {}^{4}He/H_{SolarNebula}$$

Where $^{3}He/^{4}He_{SolarNebula}$ can be estimated from this ratio in chondrites or Jupiter's atmosphere. Based on this approach Geiss and Gloeckler (1998) estimated the D/H ratio for Jupiter to be $(2.1 \pm 0.5) \times 10^{-5}$. However this estimate is based on the assumption that the $^{3}He/^{4}He$ ratio in chondrites or Jupiter's atmosphere is not fractionated and does not have any mass-independent effects. An actual measurement of the D/H ratio in Jovian atmosphere was made by NASA's Galileo probe and these analyses yielded a $D/H = (2.6 \pm 0.7) \times 10^{-5}$ (Mahaffy et al., 1998). The Jovian and therefore solar D/H ratio is lower than that of the Earth, other terrestrial planets and carbonaceous chondrites, which may reflect significant fractionation in these objects favoring heavier isotopes.

1.5.6 Comets. As discussed earlier, terrestrial planets are thought to have accreted from dry planetary embryos. One of the hypotheses regarding the origin of water on the Earth is delivery of water by comets (Hartogh et al., 2011). Determining the D/H ratio of comets is important for testing this hypothesis. Thus far, the D/H ratio of water in six comets (Halley, Tuttle, Hyakutake, Hale-Bopp, Ikeya-Zhang and LINEAR) originating from the Oort cloud (>5000 AU from the Sun) has been measured and is approximately two times higher than this ratio in the bulk Earth (Balsiger et al, 1995; Bockelée-Morvan et al., 1998; Meier et al., 1998; Biver et al., 2006; Hutsémekers et al., 2008 and Villanueva et al., 2009). Based on these results, the contribution of cometary water to the Earth is estimated to be less than 10% of the total water inventory on the Earth. However, a recent study of the Jupiter family comet Hartley 2, originating from the Kuiper belt (30-50 AU from the Sun) shows D/H = $(1.61 \pm 0.24) \times 10^{-4}$ (Hartogh et al., 2011), which is similar to the value for Earth and carbonaceous chondrites. This new study suggests that such comets could have contributed substantially to the Earth's volatile inventory. Another important implication of this work is that the hydrogen isotopic composition of the early solar nebula did not have a heliocentric gradient as was suggested by some previous studies.

1.5.7 Interplanetary Dust Particles (IDPs). Interplanetary Dust Particles (IDPs) are fine-grained (0.1 to 100 μm), mineralogically and chemically heterogeneous particles that are mineralogically, chemically, and texturally primitive in nature. IDPs have been collected in deep sediments, on the surface of Earth, and from Earth's stratosphere. These particles are believed to have originated from comets and asteroids, and are typically less altered by secondary processes than other known meteoritic materials. Hydrogen isotopic compositions of these particles

show significant variation, ranging from as low as 9×10^{-5} (McKeegan et al., 1985; McKeegan, 1987) to as high as 8×10^{-3} (Messenger, 2010). This large variation is likely caused by reactions in the cold regions of interstellar clouds, where deuterium-rich components condense on the dust grains (McKeegan et al., 1985; Messenger, 2010). Hydrogen isotopic studies of IDPs are complementary to astronomical observations and help to verify the hypotheses for producing hydrogen isotopic fractionation in the interstellar medium as described earlier.

1.6 Hydrogen isotope systematics in Tissint: Objectives and Motivation

Chapter 2 discusses the hydrogen isotopic composition of the newest martian meteorite fall, Tissint. The hydrogen isotopic composition of planetary reservoirs can provide key constraints on the origin and history of water on planets. The sources of water and the hydrological evolution of Mars may be inferred from the hydrogen isotopic compositions of mineral phases in martian meteorites, which are currently the only samples of Mars available for Earth-based laboratory investigations. Previous studies have shown that δD values in minerals in the martian meteorites span a large range of -250 to +6000 ‰. The highest hydrogen isotope ratios likely represent a martian atmospheric component: either interaction with a reservoir in equilibrium with the martian atmosphere (such as crustal water), or direct incorporation of the martian atmosphere due to shock processes. The lowest δD values may represent those of the martian mantle, but it has also been suggested that these values may represent terrestrial contamination in martian meteorites. Here we report the hydrogen isotopic compositions and water contents of a variety of phases (merrillites, maskelynites, olivines and an olivine-hosted melt inclusion) in Tissint, the latest martian meteorite fall that was minimally exposed to the terrestrial environment. We compared traditional sample preparation techniques with

anhydrous sample preparation methods, to evaluate their effects on hydrogen isotopes, and find that for severely shocked meteorites like Tissint, the traditional sample preparation techniques increase water content and alter the D/H ratios towards more terrestrial-like values. In the anhydrously prepared Tissint sample, we see a large range of δD values, most likely resulting from a combination of processes including magmatic degassing, secondary alteration by crustal fluids, shock-related fractionation and implantation of martian atmosphere. Based on these data, our best estimate of the δD value for the martian depleted mantle is -116 ± 94 ‰, which is the lowest value measured in a phase in the anhydrously prepared section of Tissint. This value is similar to that of the terrestrial upper mantle, suggesting that water on Mars and Earth was derived from similar sources. The water contents of phases in Tissint are highly variable, and have been affected by secondary processes. Considering the H_2O abundances reported here in the driest phases (most likely representing primary igneous compositions) and appropriate partition coefficients, we estimate the H_2O content of the Tissint parent magma to be ≤0.2 wt. %.

CHAPTER 2

HYDROGEN ISOTOPIC COMPOSITION OF THE MARTIAN MANTLE INFERRED FROM THE NEWEST MARTIAN METEORITE FALL TISSINT

2. 1 Introduction

Determining the hydrogen isotopic compositions of distinct planetary reservoirs is important for constraining the source(s) of volatiles and the processes that have affected the evolution of the atmosphere, surface and interior of a planet. Jupiter's D/H ratio is (Geiss and Gloeckler, 1998), which is thought to be representative of the primordial D/H ratio of the solar nebula. The D/H ratio estimated for the bulk Earth is significantly higher (D/H = 1.49 ± 0.03 × 10^{-4}; (Lécuyer et al., 1998). This value, however, is similar to that for CI chondrites, which are thought to have originated on parent bodies in the outer asteroid belt (Alexander et al., 2012). Therefore, much of Earth's water was likely derived from planetary embryos and planetesimals originating in the inner Solar System (Morbidelli et al., 2000; Hartogh et al., 2011; Alexander et al., 2012). Similarly, eucritic meteorites derived from the asteroid Vesta show D/H ratios similar to carbonaceous chondrites, also suggesting that water on this early-formed body was derived from planetesimals formed in the inner Solar System (Sarafian et al., 2014). However, a recent study has suggested that primordial water sequestered in the deep mantle of the Earth has a D/H ratio significantly lower than that of the upper mantle (Hallis et al., 2015). This may be indicative of the presence of a component in the Earth's interior that has a hydrogen isotope composition inherited directly from the protosolar nebula, but this needs to be verified with further investigations.

At present there is significant uncertainty regarding the origin of water on Mars. Martian meteorites provide an opportunity to estimate the D/H ratio of water in the martian interior, which could yield insights into the sources of water and other

volatiles on Mars. In situ hydrogen isotopic measurements of various phases in martian meteorites, such as phosphates (Boctor et al., 2003; Greenwood et al., 2008; Hallis et al., 2012a), kaersutite, biotite (Leshin, 2000), olivine, feldspathic glass (Boctor et al., 2003; Usui et al., 2015), and melt inclusions in olivine (Usui et al., 2012), reveal a large D/H range (δD from -250 to +6000 ‰, where δD is the measured D/H ratio relative to that of Standard Mean Ocean Water in parts per 1000). It has been suggested previously that the lower end of the range in δD recorded in magmatic minerals in the martian meteorites represents the hydrogen isotopic composition of primordial water in the martian mantle (Watson et al., 1994; Leshin et al., 1996; Leshin, 2000; Gillet et al., 2002; Hallis et al., 2012a; Usui et al., 2012). Alternatively, it has been proposed that these low δD values reflect a mixture of martian and terrestrial components (Boctor et al., 2003; Hallis et al., 2012a; Hallis et al., 2012b; Usui et al., 2012). The highest δD values recorded in the various phases of the martian meteorites, however, likely reflect martian near-surface processes. Specifically, the D enrichment in the martian atmosphere (δD ~5000-7000 ‰; Bjoraker et al., 1989; Novak et al., 2011; Webster et al., 2013; Villanueva et al., 2015) is likely indicative of substantial atmospheric loss of hydrogen through processes such as Jeans escape over time following early hydrodynamic escape on Mars (e.g., Leshin, 2000, and references therein). Early results from NASA's Martian Atmospheric and Volatile EvolutioN (MAVEN) mission suggest that interplanetary coronal mass ejection events result in an enhanced escape rate of ions to space and similar solar events early in martian history likely contributed to the long-term evolution of the hydrogen isotope composition of the martian atmosphere (Chaffin et al., 2015; Jakosky et al., 2015). Martian crustal water reservoirs, thought to be in equilibrium with the atmosphere, also show high δD as determined by the analyses of volatiles released from martian soils and sedimentary rocks by the Sample

Analysis at Mars (SAM) instrument on NASA's Mars Science Laboratory mission (Leshin et al., 2013; Webster et al., 2013; Mahaffy et al., 2015). The highest δD values in phases in the martian meteorites (including alteration products) approach those of the martian atmosphere and crustal water, and are suggested to result from exchange of hydrogen with crustal fluids or incorporation of martian atmosphere (Watson et al., 1994; Leshin et al., 1996; Leshin, 2000; Boctor et al., 2003; Greenwood et al., 2008; Usui et al., 2015). Absence of plate tectonics on Mars through much of its geologic history (Golombek et al., 2009) has effectively isolated the martian mantle from its atmospheric and crustal reservoirs; therefore, the martian mantle is considered to preserve the planet's primordial D/H ratio. As such, constraining the hydrogen isotopic composition of the martian mantle is important for inferring the source of water on Mars and evaluating different planetary accretion and formation hypotheses.

A variety of mechanisms have been proposed to explain the large δD range recorded in martian meteorites, including: isotopic fractionation during magma degassing, sub-solidus diffusion of hydrogen during cooling or impact-induced shock processes (Tyburczy et al., 2001; Minitti et al., 2008a; Minitti et al., 2008b), mixing between distinct isotopic reservoirs via crustal assimilation by the parent magma and/or alteration of erupted materials by crustal fluids on Mars (Leshin, 2000; Boctor et al., 2003; Usui et al., 2012, 2015), and terrestrial contamination (Boctor et al., 2003; Hallis et al., 2012a; Usui et al., 2012). Mixing between distinct low- and high-δD reservoirs has been the favored explanation for the large δD range observed in phases of martian meteorites, a range which is orders of magnitude larger than expected for physical processes such as degassing or diffusion.

Of the ~152 classified martian meteorites (some of which are paired), only five are observed falls, with Tissint being the most recent. Whereas meteorite finds

are exposed to various degrees of alteration depending on the environment and duration of their terrestrial residence, falls are typically only minimally affected if they are recovered soon after landing on Earth. Terrestrial contamination in meteoritic materials is evidenced by the formation of weathering products such as calcite and clays, as well as alteration of trace element patterns (Crozaz and Wadhwa, 2001) and isotopic ratios (Hallis et al., 2012a; Hallis et al., 2012b). The effects of terrestrial contamination are of particular concern for measurements of D/H ratios in meteoritic samples, because hydrogen is highly mobile and readily equilibrates between meteoritic phases and terrestrial fluids. Hence, contamination due to residence in the terrestrial environment poses a serious concern for determination of the indigenous hydrogen isotopic composition of martian meteorite phases. Another potential source of terrestrial contamination is sample handling and preparation in the laboratory. Most δD analyses of martian meteorite phases have been performed by secondary ion mass spectrometry (SIMS) on samples prepared as standard geological thin sections which are cut, ground, and polished in water or other aqueous fluids (Leshin, 2000; Boctor et al., 2003). Moreover, as these meteorites are typically highly shocked and fractured, the traditional vacuum impregnation with epoxy while preparing thin sections can further cause hydrogen contamination (Hallis et al., 2012a; Hallis et al., 2012b; Usui et al., 2012). Such contamination effects (whether from terrestrial residence or processing in a laboratory) on the measured δD values in martian meteorites have been reported previously (Boctor et al., 2003; Greenwood et al., 2008; Hallis et al., 2012a; Hallis et al., 2012b; Usui et al., 2012). Tissint provides a unique martian sample with minimal terrestrial contamination from interaction with terrestrial fluids, because of its short residence time on Earth. We attempt to evaluate the effects of sample preparation

techniques on Tissint, and its implications for the hydrogen isotopic signature of the martian interior.

The Tissint strewn field lies in an arid region south-southwest of Tissint in Morocco near the Algerian border. The fall occurred on 18th July 2011 and many whole stones and fragments were recovered within weeks of this event (Aoudjehane et al., 2012; Irving et al., 2012). Petrographic and geochemical investigations suggest that Tissint is one of the freshest available martian meteorites, with virtually no observable effects of terrestrial weathering (Aoudjehane et al., 2012; Balta et al., 2015). As such, this meteorite represents a unique opportunity to study a martian basaltic rock with minimal, if any, terrestrial contamination. In this study, we report the hydrogen isotopic compositions of phases analyzed in two samples of Tissint that were prepared specifically to evaluate the effects of different sample preparation techniques. Based on the analyses of these samples, we present the implications for the hydrogen isotopic composition of the martian mantle.

2.2 Sample Description

On the July 18th 2011, a large fireball across northwest Africa heralded the arrival of the fifth martian meteorite fall (Aoudjehane et al., 2012). Glossy, fusion-crusted stones were picked up several weeks later in southern Morocco, near the town of Tissint from which the meteorite's name is derived. Tissint is a depleted basaltic shergottite containing abundant magnesian olivine phenocrysts in a groundmass of fine-grained pyroxenes and maskelynites (Balta et al., 2015). It is one of the oldest known shergottites, with a crystallization age of 574 ± 20 Ma (Brennecka et al., 2014b), and has a cosmic-ray exposure age of 0.7 ± 0.3 Ma (Aoudjehane et al., 2012). Tissint shows evidence of surface weathering on Mars, as recorded in the chemistry of the impact melt glass produced during the shock event

that ejected the sample from Mars and incorporated martian surface alteration products. Specifically, this glass is enriched in volatiles such as H_2O, CO_2, F, and Cl (Chen et al., 2015), as well as in light rare earth elements (Aoudjehane et al., 2012). Most phases in Tissint are highly fractured as a result of shock, with the exception of maskelynite, which is a diaplectic glass, produced during this shock (Figure 2.1).

2.3 Methods

2.3.1 Sample Preparation. We obtained a sample of Tissint from the meteorite collection in the Center for Meteorite Studies at Arizona State University (ASU); this was derived from a fragment that was one of the earliest recovered pieces. To assess the effects of different preparation techniques on hydrogen isotope analyses, we prepared two polished sections from this sample: one was a standard epoxy impregnated polished thin section (referred to hereon as "PTS"; this section was designated as "Tissint, 6" and was studied by Balta et al., 2015) and the other was a polished thick section prepared without the use of water, hydrocarbon-based fluids or epoxy (referred to hereon as the anhydrously prepared thick section or "ATS"). To prepare the Tissint ATS, a fusion-crusted piece (the interior of which was not exposed until it was cut in the laboratory) was cut with a saw without the use of any lubricant. The cutting was performed very slowly to avoid heating the sample. A thick section of approximately 5 mm thickness was cut from this piece. The section was dry-polished on various grit sized polishing papers. The final polish was done with a dry velvet cloth coated with ~1 μm diamond powder. This polishing cloth was prepared by first coating the velvet with the diamond powder that was suspended in a water-based solution, followed by drying overnight in a 60°C oven. Both the PTS and the ATS were coated with carbon before the EPMA and SIMS analyses.

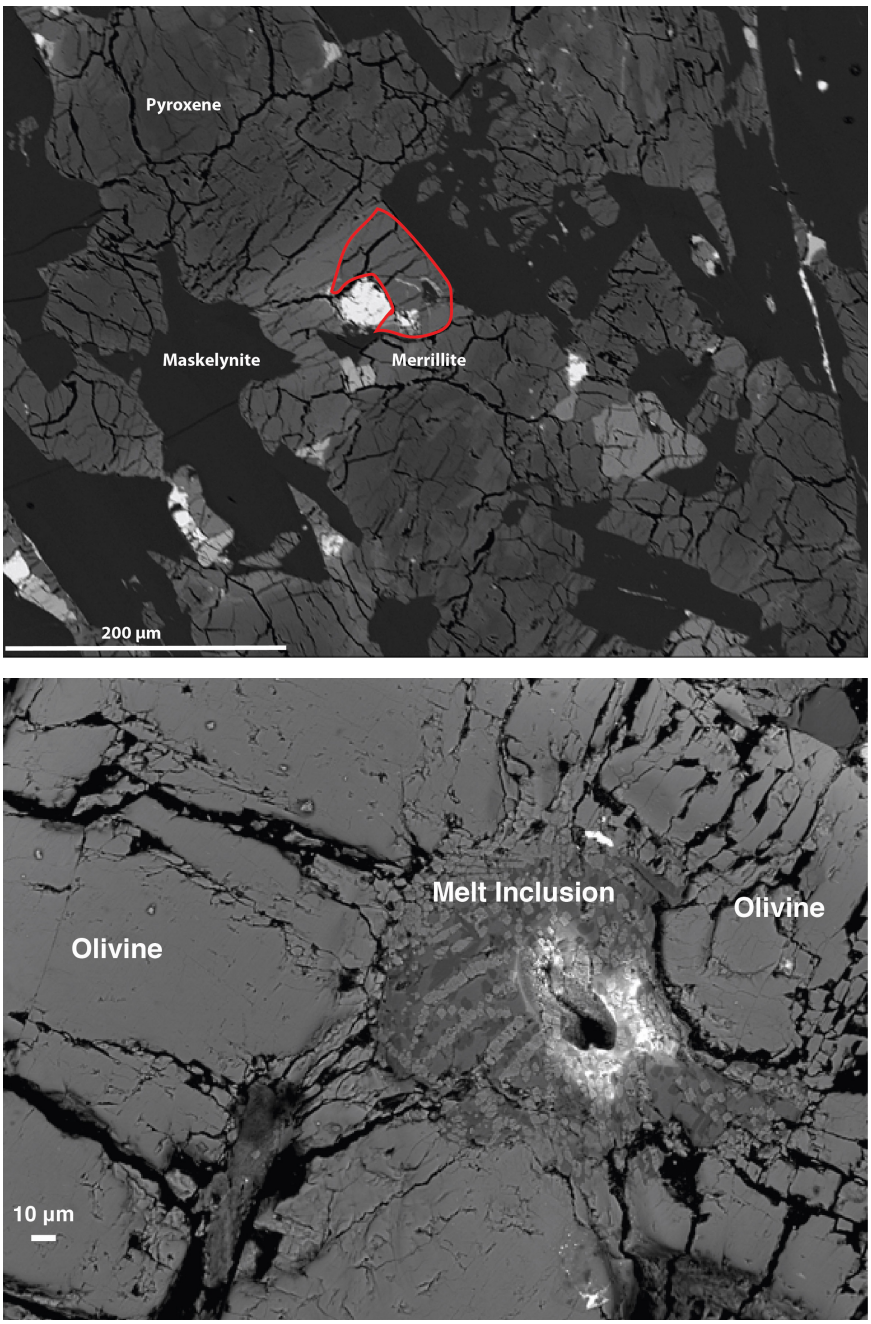

Figure 2.1. a) Backscattered electron (BSE) image showing various phases in the Tissint PTS prior to SIMS analyses. It can be somewhat difficult to distinguish merrillites (shown in the image with a red outline) from surrounding pyroxenes in a BSE map, but they were easily identified in the elemental maps that were also obtained by us. b) BSE image of an olivine-hosted melt inclusion showing an area where SIMS analyses (3 repeat runs) were conducted.

2.3.2 Electron microprobe analyses. The PTS was documented and its mineral compositions were determined using the Cameca SX-100 electron microprobe at the University of Tennessee; the analytical details for these analyses are given by (Balta et al., 2015)). The Tissint ATS was documented using a JEOL JXA-8530F Hyperprobe at ASU. Backscattered electron (BSE) imaging and elemental EDS mapping were conducted to identify mineral phases in the ATS. After the isotopic analysis, SIMS craters in the PTS and ATS were examined again with BSE imaging using the JEOL Hyperprobe at ASU.

2.3.3 Secondary ion mass spectrometry analyses. Hydrogen isotopic compositions and H_2O contents were measured using the Cameca IMS-6f secondary ion mass spectrometer (SIMS) at ASU. A Cs^+ primary beam (10 kV accelerating voltage) with a beam current ranging from 7 to 10 nA was used. Negative secondary ions were accelerated to 5 kV from the sample into the mass spectrometer. The Cs^+ primary beam has an advantage over O^- beam, since it results in lower instrumental mass fractionation and matrix effects (Deloule et al., 1991). Also, it is preferable to use negative secondary ions, since H_2^- interference on D is negligible (McKeegan et al., 1985), allowing the use of low mass resolving power (~500), which results in higher secondary ion intensities; this is especially important for analyzing the hydrogen isotopic compositions of nominally anhydrous phases that are targeted here. Each SIMS analysis run consisted of 60 cycles, with each cycle consisting of measurements of H (for 1 second) and D (for 10 seconds). The typical analysis spot size was ~20 μm, but the circular area from which secondary ions were accepted into the mass spectrometer was set at 8 μm, at the center of the crater, using the smallest (100 μm) field aperture. The total analysis time for each spot was ~15 minutes. A dead time correction of 42 ns was applied to all the analyses. At the end

of each analysis, $^{16}O^-$ was measured, providing $H^-/^{16}O^-$ ratios that were used to determine the H_2O content. A normal-incidence electron gun was used to neutralize the positive charge build-up in the sputtered crater. We used a GaN sample to align the electron gun using cathodoluminescence (Chen et al., 2013). The measured hydrogen isotopic compositions are reported relative to Standard Mean Ocean Water (SMOW; D/H=0.0001559), as follows:

$\delta D = ([(D/H)_{Sample}/(D/H)_{SMOW}] - 1) \times 1000$

Durango apatite, with a reported δD value of -120‰ (Greenwood et al., 2011), was used as the standard for hydrogen isotope analyses of merrillite. For silicates, a rhyolitic glass ("Macusanite rhyolitic glass" with δD = -150‰; Pichavant et al., 1987) was used as the standard for hydrogen isotope measurements. For determining the H_2O contents of various phases in Tissint, a set of three rhyolitic glasses (with known H_2O contents of 0.5, 1.3, and 2.4 wt.%) along with Durango apatite (0.09 wt.% H_2O) were used to determine the slope of a calibration line in a plot of $H^-/^{16}O^-$ versus H_2O abundances. Based on repeat analyses of these standards during the different analysis sessions, we estimate the external reproducibility (2SD) of our measurements of H_2O contents to be ±20%.

Analyses of the nominally anhydrous Lake County plagioclase, co-mounted in an epoxy mount with the apatite and rhyolite glasses, were performed to assess the hydrogen blank during SIMS measurements. The hydrogen ion signal on this standard epoxy mount varied depending on the analysis session and the amount of time the mount resided in the vacuum chamber. The resulting $H^-/^{16}O^-$ ratios suggested that the best blank value on the standard epoxy mount (still likely to be higher than the blank during actual sample analyses; see below) was ~30 ppm. We anticipate the blank is lower for the actual analyses of the Tissint PTS and ATS measured here because epoxy is minimized (in the PTS) or absent (in the ATS), and

these samples were stored under vacuum prior to analyses (see below). Nevertheless, since the blanks were measured in a separate mount than the samples, we cannot know their precise value for the actual sample analyses. As a result, while we can place an upper limit on the blanks for our analyses, no blank correction has been applied to the data reported in Table 1. For phases with measured H_2O contents higher than a few hundred ppm the blank is smaller than the analytical uncertainty and is not significant. However, we may be overestimating the H_2O contents given in Table 1 of phases with the lowest concentrations by at most a factor of ~2.

The data on the Tissint PTS and ATS were acquired over three analysis sessions lasting for 3 to 4 days each. The instrumental mass fractionation varied from -40 to -150 ‰ between sessions. The D/H ratio of nominally anhydrous minerals can be significantly affected by residual H atoms present in the sample chamber vacuum (Hallis et al., 2012a). As such, the Tissint samples were left inside the SIMS sample chamber under vacuum for a duration ranging from several hours (for the PTS) to overnight (for the ATS) before each analytical session. For all analyses reported here, the measured δD values showed no correlation with the pressure reading in the sample chamber, and so this effect was insignificant. The samples were pre-sputtered for a minimum of 3 minutes before each analysis to remove any surface contamination.

As we used rhyolitic glass standards to determine the calibration curve for calculating the H_2O content of Tissint merrillites, maskelynites and olivines, we must also consider potential matrix effects. The influence of matrix effects between the maskelynite and rhyolite glass have not been investigated. However, (Aubaud et al., 2007) described nearly identical calibrations for Ca-rich basalts and Ca-poor rhyolites, and hence we have assumed that any matrix effect between the Ca-rich

glassy maskelynite and our rhyolite glass standards is also insignificant. The influence of such matrix effects on merrillites is unknown, and therefore no correction was applied. We did, however, apply a matrix effect correction for H_2O contents measured in olivines. Using a similar analytical procedure to that utilized here (i.e., detecting hydrogen as the H^- species), (Aubaud et al., 2007) showed that the slope of the calibration line for olivine in a plot of $H^-/^{30}Si^-$ versus H_2O abundances was approximately 2.9 times that for rhyolite. Mosenfelder et al. (2011) has shown that changing the matrix ion from Si to O changes the absolute calibration, but not the linearity of the calibration. We applied this correction factor to our olivine analyses, and so the H_2O contents reported for this mineral (shown in italics in Table 1) have been corrected for this matrix effect. We note that while the accuracy of the absolute H_2O contents reported here may be affected to some (greater or lesser) degree by matrix effects, the relative H_2O contents for a set of analyses of any one mineral phase are robust. Other laboratories have detected hydrogen as $^{16}OH^-$ species when determining the H_2O contents of nominally anhydrous phases and these studies observe smaller matrix effects between olivine and rhyolite glass (e.g., Tenner et al., 2009). However, if we were to detect hydrogen as the $^{16}OH^-$ species instead of as H^- species, we would need to operate at much higher mass resolving power (translating to lower transmission) to isolate the $^{17}OH^-$ and $^{16}OH_2^-$ ions from the $^{16}OD^-$ ion for determining isotopic ratios, and so we opted to run at nearly maximum transmission by detecting hydrogen as H^- species (e.g., Hauri et al., 2002).

It was recently shown that for SIMS measurements, averaging isotopic ratios collected over the course of a measurement results in a bias compared to the true ratio if the ion intensity for one of the isotopes is low (Ogliore et al., 2011). To address this data analysis artifact, we calculated the D/H ratio by using the sum of

all counts for D and H measured during each measurement, instead of averaging the individual D/H ratios obtained for every cycle in that measurement. The errors on the δD values reported in Table 1 are two times the standard errors of the mean; those analyses where the standard error was more than two times larger than the best possible (Poisson) errors from counting statistics were discarded. For SIMS analyses, the best possible (Poisson) errors from counting statistics are comparable to the standard errors of the mean. The discarded analyses (where the standard error is significantly higher than the Poisson errors) showed significant variations in the isotopic ratios during a single run which were attributed to the beam sputtering through different phases or encountering grain boundaries or cracks during the analysis. This was verified following the SIMS analyses via examination of the analysis spots using the electron microprobe at ASU.

2.4 Results

We report here the hydrogen isotopic compositions and H_2O contents in merrillite, maskelynite, and olivine in each of the two sections (PTS and ATS) of Tissint. We additionally analyzed multiple spots within a single melt inclusion hosted within an olivine in the ATS. These data are reported in Table 2.1.

In the PTS, merrillites show a range in δD of -105 ± 20‰ to +524 ± 16‰, and their H_2O contents vary from 0.29 to 0.96 wt.% (2900 to 9600 ppm) (Figure 2.2a, Table 2.1). Maskelynites in the PTS (Figure 2.2b, Table 2.1) show δD of +119 ± 24‰ to +1340 ± 22‰ with H_2O content varying from 0.014 to 0.061 wt.% (140 to 610 ppm) (except one analysis on a fracture with a significantly higher H_2O content of 0.62 wt.% and δD of -51 ± 24‰). Two olivine grains analyzed in this section show low δD values of -43 ± 9 ‰ and -121 ± 5 ‰ and H_2O contents of 0.037 and 0.035 wt.% (370 and 350 ppm) (Table 2.1).

In the ATS, merrillites (Figure 2.2a, Table 2.1) show δD of +272 ± 28‰ to +2418 ± 15‰ and H_2O content of 0.04 – 0.38 wt.% (400 to 3800 ppm), whereas maskelynites (Figure 2.2b, Table 2.1) have an even larger spread in δD of -116 ± 94‰ to +3682 ± 40‰ and H_2O content of 0.003 – 0.054 wt.% (30 to 540 ppm). Olivines show considerably lower δD values and a smaller spread (δD ranging from +12 ± 53‰ to +470 ± 37‰) compared to the merrillites and maskelynites (Table 2.1). Their H_2O content ranges from 0.005 to 0.035 wt.% (50 to 350 ppm). Several analyses of a single olivine-hosted melt inclusion show δD values ranging from +904 ± 16‰ to +1397 ± 22‰ and H_2O contents from 0.15 to 0.20 wt.% (1500 to 2000 ppm) (Table 2.1).

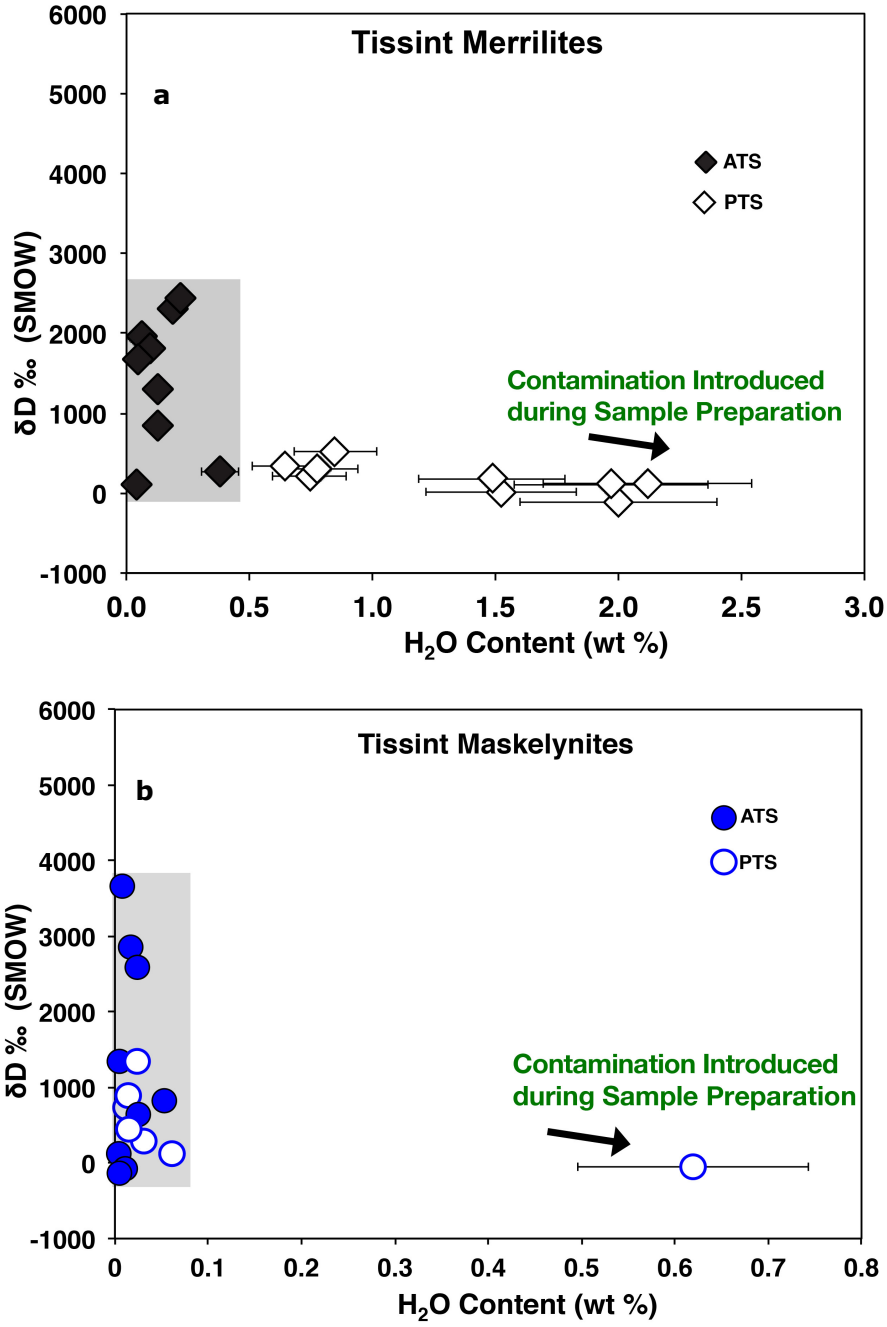

Figure 2.2. a) Hydrogen isotopic composition plotted against H_2O content in Tissint merrillites. The solid black diamonds are analyses on the anhydrously prepared thick section (ATS); the open black diamonds are on a polished thin section (PTS) prepared using epoxy. b) Hydrogen isotopic composition plotted against H_2O content in Tissint maskelynites. The solid blue circles are analyses on the ATS; open blue circles are on the PTS. The gray boxes in these figures highlight the compositions that appear to be largely unaffected by contamination during sample preparation.

2.5 Discussion

2.5.1 Evaluating effects of sample preparation techniques. Comparison of PTS with ATS data demonstrates the effects of sample preparation on the degree to which different phases can be contaminated. In particular, δD values in the PTS merrillites show a negative correlation with their H_2O contents, whereas there is no such correlation in merrillites in the ATS (Figure 2.2a). Furthermore, the PTS merrillites have higher H_2O contents and a restricted range in δD compared to the ATS merrillites (Figure 2.2a, Table 2.1). Merrillite is a nominally anhydrous mineral, but it can form a solid solution with the mineral whitlockite, the end-member composition of which can have up to ~8500 ppm H_2O (McCubbin et al., 2014; Hughes et al., 2006). Some of the merrillites analyzed in the Tissint PTS have up to 9600 ppm H_2O, which is more than the merrillite-whitlockite system can accommodate. Therefore, we believe that these analyses of the PTS merrillites have some contribution from epoxy filling the microcracks commonly found in this mineral in the martian meteorites. Although only two olivines were measured in the PTS, these analyses too show significantly higher H_2O contents and low δD compared to olivines analyzed in the ATS (Table 2.1). As such, it seems plausible that H_2O contents and hydrogen isotope systematics in merrillites and olivines in the Tissint PTS have been affected to a greater extent than the Tissint ATS by the addition of a terrestrial water component characterized by a low δD. In contrast, maskelynites in both the PTS and ATS show a similar range of H_2O contents (with the exception of one analysis in the PTS that was obtained on an epoxy-filled crack and has a significantly higher H_2O abundance). The PTS maskelynites do show a somewhat more restricted range in δD values compared to ATS maskelynites and there may be a hint of an anti-correlation between δD and H_2O content (Figure 2.2b), but this may be a sampling artifact given the fewer analyses of this phase conducted on the PTS.

Given these data, it appears that highly fractured grains such as merrillite and olivine can be significantly contaminated with terrestrial hydrogen during PTS preparation involving epoxy impregnation and cutting and polishing in water. In this context, it may be worth noting an apparently weak anti-correlation between δD and H_2O content in ATS olivines (Figure 2.3) possibly suggesting a small degree of terrestrial contamination recorded in this mineral even in the ATS. However, since there are only few analyses of ATS olivines, and they all have systematically higher δD and lower water content than PTS olivines, any terrestrial contamination of this mineral in the ATS is still inferred to be minimal. In contrast, a glassy, unfractured phase such as maskelynite appears to be significantly less affected by laboratory contamination. Furthermore, the lack of correlation between δD values and H_2O contents in phases measured in the ATS (with the possible exception of olivine; see above) strongly suggests that hydrogen isotope systematics in Tissint are minimally, if at all, affected by terrestrial contamination in the field prior to recovery. These results have implications for interpretations based on previously reported SIMS hydrogen isotope data obtained on shocked and fractured mineral phases in polished thin sections of the martian meteorites prepared with epoxy and water.

In light of the above, in the following discussion sections, any interpretations regarding the hydrogen isotopic compositions of martian reservoirs or processes on Mars affecting the δD of martian crustal rocks are based only on the hydrogen isotope data obtained on the Tissint ATS (Figure 2.3).

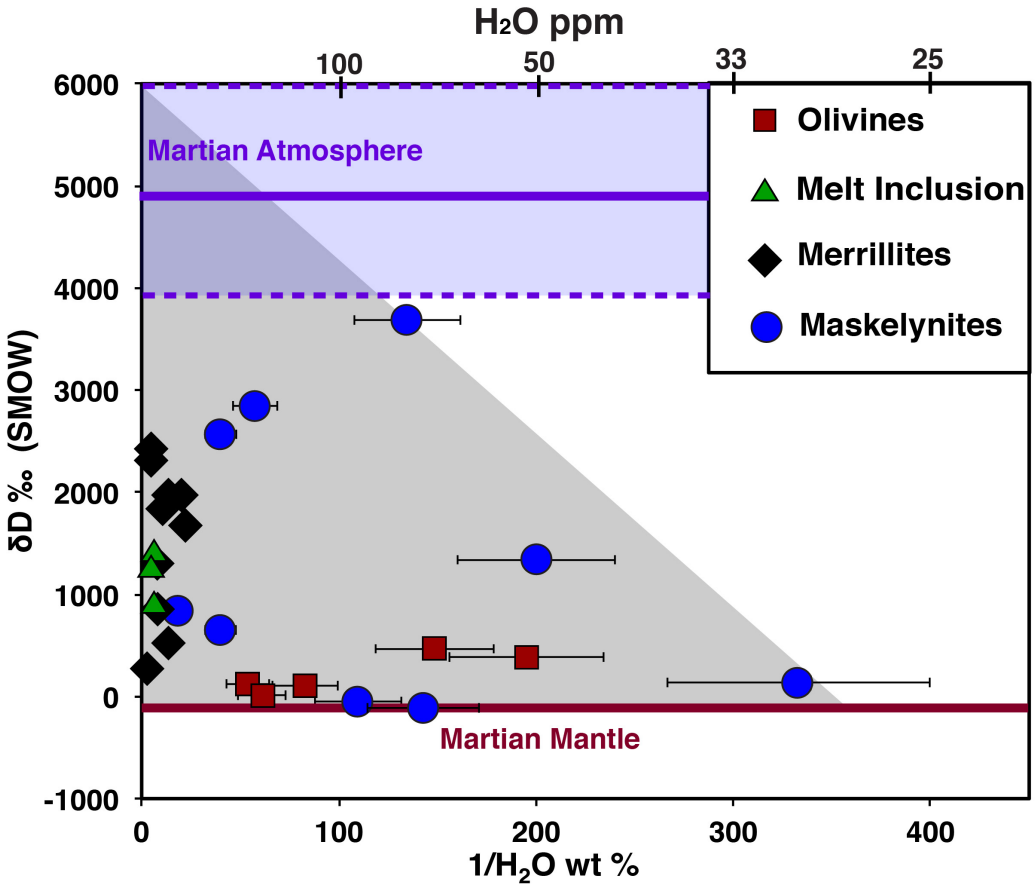

Figure 2.3. δD versus $1/H_2O$ for phases analyzed in the Tissint ATS; linear trends in such a plot may be explained by mixing between distinct components in this composition space. Maskelynites (solid blue circles) and merrillites (solid black diamonds) show considerable scatter in their δD, with the lowest δD values close to zero. Red squares show olivine analyses while green triangles show multiple analyses on a single devitrified olivine-hosted melt inclusion. The range of compositions shown here can be explained by mixing between three components, the end-members of which are defined by the apices of the gray triangle: (1) A wet, high δD component (upper left) most likely representing martian crustal fluids (i.e., aqueous fluids that have exchanged hydrogen with the martian atmosphere); the δD of this component is taken to be the highest possible value based on the measurement of the martian atmosphere by the SAM instrument on the Mars Science Laboratory (shown as the horizontal purple box bounded by the purple dashed lines showing δD = +4950 ±1080 ‰; Webster et al., 2013). (2) A drier, low δD component (lower right) representing a martian magmatic signature (specifically, primary magmatic compositions of different minerals would be expected to fall along the horizontal brown line representing the martian mantle, with H_2O contents consistent with their respective mineral/melt partition coefficient; the lower right corner of the gray triangle shown here is constrained by the measured ATS maskelynite compositions). (3) A wet, low δD component that could represent either a terrestrial-like martian component (such as evolved, volatile-rich magmatic fluid) or terrestrial contamination.

2.5.2 Comparison with previous hydrogen isotope studies on Tissint.

Preliminary data reported by Hallis et al. (2014) for the primary igneous minerals olivine and pyroxene in Tissint showed higher H_2O contents (0.07 – 0.36 wt.%) and more restricted δD values (-150 to +100‰) compared to the ATS olivines analyzed here. In that study, olivine-hosted melt inclusions also showed significantly higher H_2O contents of 0.49 – 0.56 wt.% and a more limited range in δD of -98 to +372‰, compared to the olivine-hosted melt inclusion analyzed here (Table 1). Hallis et al. (2014) additionally reported that shock melts in Tissint have H_2O contents of 0.02-0.23 wt.% and δD ranging from -66 to +4224‰.

A more recent study by Chen et al. (2015) has reported H_2O contents and the hydrogen isotopic compositions of impact melts and maskelynites in Tissint. These authors demonstrated that Tissint impact melts (δD values varying from +45 to +4867 ‰ and H_2O contents ranging from 0.02 to 0.24 wt.%) showed a negative linear correlation between $1/H_2O$ and δD, indicative of mixing between two end-member water reservoirs on Mars. The CO_2, S, F and Cl concentrations and C isotope compositions in these impact melts suggest that this mixing trend is due to the incorporation of volatile-rich alteration products formed by groundwater on Mars (and characterized by a high δD similar to the martian atmosphere) into a volatile-poor, low-δD magmatic component (i.e., a mixture of primary igneous minerals olivine, pyroxene and plagioclase) during impact-induced melting on Mars (Chen et al., 2015). These authors additionally reported that Tissint maskelynites had H_2O contents <0.01 wt.% and a restricted δD of -222 to +296‰; three of their maskelynite data points showed higher δD values of +1171 to +2970‰, but they attributed these to contributions from phosphates during their SIMS analyses. While the majority of our ATS maskelynites (5 of 9) do indeed have H_2O contents <0.01 wt.%, some have higher H_2O abundances (up to ~0.054 wt.%). Moreover, our ATS

maskelynites have a wide range in δD (-116 to +3682‰) that is not correlated with their H_2O content. Post-analysis BSE imaging of these maskelynites did not show beam overlap with any other phases and, as such, we believe that the range in H_2O abundances and δD is characteristic of this phase in Tissint. This does not preclude the possibility that the original plagioclase was characterized by low H_2O and δD as suggested by Chen et al. (2015) based on the negative linear correlation between $1/H_2O$ and δD in impact melt glasses. This merely implies that the same shock event that produced these impact glasses (from melting of different proportions of magmatic minerals including plagioclase) also produced the maskelynite, which acquired its variable H_2O contents and δD values during this event (see section below on "Shock-related fractionation and implantation of martian atmosphere" for a more detailed discussion of this possibility).

2.5.3 Cause(s) of δD variation within and between phases in Tissint.

There are various processes that may have affected the hydrogen isotope systematics of Tissint. In the following, we discuss these possibilities and examine the rationale for which ones may be the most likely to result in the inter- and intra-phase variations in δD reported here.

2.5.3.1 Crustal assimilation. Geochemically, shergottites are classified as enriched, intermediate and depleted, based on their trace element compositions (McCoy et al., 2011). These shergottite groupings also correlate with their radiogenic isotope systematics and magmatic redox conditions (Wadhwa, 2001; Herd et al., 2002; Borg and Draper, 2003; Treiman, 2003; Debaille et al., 2008; Symes et al., 2008; Basu Sarbadhikari et al., 2009; Usui et al., 2010; Brandon et al., 2012). It has been suggested previously that these shergottite groupings imply the presence of at

least two distinct geochemical reservoirs on Mars: one that is an incompatible element-depleted, reduced reservoir and another that is an incompatible element-enriched, oxidized reservoir. These two geochemically distinct reservoirs could either both reside in the martian mantle (Borg and Draper, 2003; Debaille et al., 2008; Symes et al., 2008; Brandon et al., 2012) or the depleted reservoir may reside in the mantle while the enriched reservoir could be in the martian crust (Wadhwa, 2001; Herd et al., 2002; Basu Sarbadhikari et al., 2009). Previous studies have suggested that crustal assimilation by the shergottite parent magmas may have affected their light isotope systems such as hydrogen (Usui et al., 2012) and sulfur (Franz et al., 2014). Martian crustal material that has been altered by crustal fluids, which equilibrated with the Mars atmosphere, is expected to have high δD. If shergottite parent magmas originated from a mantle with relatively low δD, then assimilation of altered crust with high δD into such magmas could result in δD variations among the different martian meteorites. However, variations in δD on the micron-scale (i.e., between and within individual phases) as seen in Tissint cannot be readily explained by this type of mixing process. Furthermore, trace element and radiogenic isotope systematics in Tissint suggest that it is one of the most depleted shergottites, implying minimal (if any) crustal assimilation (Brennecka et al., 2014b; Balta et al., 2015). Therefore, the hydrogen isotopic compositions of the phases in Tissint are not likely to have been affected by crustal assimilation.

2.5.3.2 Magmatic degassing. Hydrogen isotope systematics have been investigated in a variety of terrestrial igneous rock types in order to understand the evolution of volatiles in their parent magmas. Magmatic degassing is an important process that can fractionate hydrogen isotopes (Taylor, 1986). Specifically, depending on the magmatic redox conditions, hydrogen release from silicate

magmas occurs either through dehydrogenation (H_2 loss) or dehydration (H_2O loss) (e.g., Newman et al., 1988). While dehydrogenation results in an increase in δD and negative correlation between δD and H_2O content, dehydration typically results in a decrease in δD and a positive correlation between δD and H_2O (e.g., Demény et al., 2006).

One of the earliest attempts to understand the effects of degassing of water on the hydrogen isotopic composition of magmas was a study of rhyolitic glasses which showed a correlation of δD with the H_2O content (Taylor et al., 1983). A more detailed study performed recently on Indonesian arc basalts reveals that the extent of hydrogen isotopic fractionation during dehydration of magma depends on the species being degassed from the magma (i.e., water dissolved as hydroxyl or as molecular water) and, to a lesser extent, temperature of the magma (De Hoog et al., 2009). Since these parameters are not constant during the degassing process, the extent of hydrogen isotope fractionation during degassing of water depends on the evolution of the magma system. Nevertheless, dehydration of magmas typically results in hydrogen isotope fractionation on the order of ≤~150‰.

Under more reducing conditions, such as in lunar magmas, hydrogen release occurs primarily through dehydrogenation (degassing of H_2). This process can increase δD significantly in the residual magma. Degassing of up to 95-98% of H_2 can increase δD by up to 800-1000‰ and produces a negative correlation between δD and H_2O content (Saal et al., 2013; Sharp et al., 2013; Tartèse et al., 2013). Given the reduced nature of Tissint (log fO_2 ~ QFM -4 to -2.4; (Balta et al., 2015), it is possible that H_2 degassing during crystallization could have contributed, at least in part, to the variation in δD. Nevertheless, the total δD range reported here in the ATS maskelynites (from as low as ~-100 up to as high as ~+3700‰) is not readily explained by H_2 degassing alone. Combined C-O-H species have also been argued to

be possibly present in martian magmas and could influence degassing species (and the extent of associated hydrogen isotope fractionation). However, given the low molar abundances of carbon present compared with hydrogen, these species would likely have little to no impact on the δD recorded in these rocks (Stanley et al., 2014).

2.5.3.3 Secondary alteration by crustal fluids. The ubiquitous presence of valley networks (e.g., Bakers, 1982) and lake deposits (e.g., Squyres, 1989) on ancient martian terrains indicates the presence of surface water and of a denser atmosphere in the early history of Mars. Among martian meteorites, shergottites lack extensive evidence of secondary alteration and weathering compared to other martian meteorite groups such as the nakhlites (McSween, 1994). Tissint in particular lacks significant mineralogical evidence for secondary weathering and alteration. However, hematite occurs in impact melt glass, and has been interpreted to reflect incorporation of a surface component during impact (Kuchka et al., 2014). Tissint also contains magnetite, which is argued to be a deuteric alteration product of ulvöspinel (Gattacceca et al., 2013). It has additionally been argued that some of the geochemical and isotopic characteristics of the abundant impact melt glasses in Tissint are the result of incorporation of a near-surface weathered component during the impact event on Mars (Aoudjehane et al., 2012).

Crustal fluids on Mars that equilibrated with the D-enriched martian atmosphere are expected to have a similarly high δD value. Assuming that the primary igneous minerals in the shergottites have a low δD reflecting that of the shergottite mantle source, interaction with a relatively D-enriched crustal fluid (under conditions with relatively low fluid to rock ratios) could result in variable increases in δD in these minerals through incomplete exchange of hydrogen with the

fluid. As proposed earlier for phases in other martian meteorites (Watson et al., 1994; Boctor et al., 2003; Greenwood et al., 2008; Usui et al., 2012, 2015), such near-surface fluid interactions on Mars could also be responsible for the large variations seen in δD in Tissint phases. Given that the crystallization age of Tissint is ~575 Ma (Brennecka et al., 2014), this fluid-rock interaction may have taken place anytime since then but prior to ~0.7 Ma, the time of ejection of this sample from the surface of Mars (Aoudjehane et al., 2012). Moreover, this process could have been continuous or episodic based on the availability of water in the near-surface environment on Mars during this time period.

2.5.3.4 Shock-related fractionation and implantation of martian atmosphere.

Shergottites have experienced one or more shock events, with the final impact resulting in their ejection from the surface of Mars (~0.7 Ma ago in the case of Tissint; (Aoudjehane et al., 2012). Shock effects in these meteorites are evidenced by the presence of phases such as maskelynite, ringwoodite, and impact melt pockets. Tissint in particular shows a variety of shocked phases such as ringwoodite, akimotoite, lingunite, majorite, tuite, stishovite, silicate perovskite and impact-produced glass (Baziotis et al., 2013; Walton et al., 2014) and two new high-pressure minerals, ahrensite and tissintite (Ma et al., 2014). It is estimated to have experienced peak shock pressure in the range of ~25 to 40 GPa (Baziotis et al., 2013). Analysis of natural remnant magnetization (NRM) shows that this meteorite was re-magnetized during multiple impact events (Gattacceca et al., 2013). Therefore, there is extensive evidence of shock effects in Tissint.

There have been several experimental studies that demonstrated that impact-related shock causes an increase in δD of the residual solid (Tyburczy et al., 2001; Minitti et al., 2008a; Minitti et al., 2008b). However, these experimental studies on

serpentinite (Tyburczy et al., 2001) and kaersutite (Minitti et al., 2008a) show that impact-induced fractionation only increases δD by ~100‰. Furthermore, some shock experiments on bulk amphibolites and kaersutitic amphiboles show that the H_2O content of the shocked material increases (Minitti et al., 2008a; Minitti et al., 2008b). This increase is primarily attributed to two processes. First, the reduction reaction of Fe^{3+} to Fe^{2+} in kaersutites during impact is expected to increase the H_2O content. Specifically, the crystal chemistry of amphibole couples the water content and oxidation state of Fe via the following reaction, which would move towards the left during impact (Minitti et al., 2008a; Minitti et al., 2008b):

$$Fe^{2+}_{Kaersutite} + OH^{-}_{Kaersutite} \Leftrightarrow Fe^{3+}_{Kaersutite} + O^{2-}_{Kaersutite} + \tfrac{1}{2}H_{2External}$$

The second process that likely affects the H_2O content is shock implantation of atmospheric gases, which would also greatly affect the δD under martian conditions (Minitti et al., 2008a). Indeed, there is evidence of shock-implanted martian atmosphere in several shergottites (Bogard and Johnson, 1983; Marti et al., 1995; Beck et al., 2007). Thus, shock implantation of a D-enriched martian atmosphere could have increased the δD in the phases in Tissint. Given the micron-scale heterogeneity of the effects of shock metamorphism in the martian meteorites, it is possible that the δD (and H_2O content) were variably affected on the micron-scale as well.

2.5.4 Implications for the δD signature of the martian mantle. The δD of the terrestrial upper mantle is determined through the analysis of terrestrial basalts originating from it. One of the first estimates was from Mid Ocean Ridge Basalts (MORB) that have δD of ~-80 ‰ (Kyser and O'Neil, 1984). Subsequent studies show that MORBs have a range of δD from -100 to -20 ‰ (Poreda et al., 1986; Chaussidon et al., 1991; Honma et al., 1991; Kingsley et al., 2002; Pineau et

al., 2004; Clog et al., 2013). Most recently, Clog et al. (2013) re-investigated a suite of MORB samples and estimated that the δD of the terrestrial depleted upper mantle is -60 ± 5‰.

Previous estimates of the δD value of the martian mantle range from ~-100 to ~+1000 ‰ (Watson et al., 1994; Leshin, 2000; Boctor et al., 2003; Hallis et al., 2012a; Usui et al., 2012) (Figure 2.4). In particular, some previous studies suggest that the martian mantle has a relatively high δD (possibly as high as ~+1000 ‰; (Leshin, 2000). If this is true, the distinct δD values for the mantles of Mars and Earth would imply that sources of water for the terrestrial planets were different. Other analyses suggest that the δD value of the martian mantle may be similar to that of the Earth's upper mantle (Gillet et al., 2002; Boctor et al., 2003; Hallis et al., 2012a). The reasons for such a range in the estimated δD values of the martian mantle (based on analyses of different phases in different types of martian meteorites, with distinct magmatic/post-magmatic histories on Mars and varying terrestrial exposure histories) are likely to be complicated. In particular, it can be difficult to rule out the effects of terrestrial contamination, and deconvolve them from other effects associated with degassing and shock. For example, minerals in some martian meteorites show a negative correlation of δD with water contents (e.g., Leshin, 2000; Boctor et al., 2003), which could imply mixing between either two distinct martian reservoirs, or a martian reservoir with high δD and low H_2O content and a terrestrial component with low δD and high H_2O content. The data reported here for merrillites in the Tissint PTS (Figure 2.2a) suggest that such a trend could potentially result from contamination during sample preparation. More recently, Usui et al. (2012) have made the case that the martian mantle has an Earth-like δD (≤+275 ‰) based on analyses of the olivine-hosted melt inclusions in a geochemically depleted basaltic shergottite; however, allowing for some terrestrial

contamination of these melt inclusions yields an upper limit on the martian mantle δD of ~+1000 ‰.

Tissint is unique among martian meteorites since it sampled one of the most depleted mantle source reservoirs on Mars (Aoudjehane et al., 2012; Brennecka et al., 2014b; Balta et al., 2015). As discussed earlier, as the freshest martian meteorite fall and most rapidly delivered to modern laboratories, it is also the least affected by residence in the terrestrial environment. As such, it is currently the best representative among the known martian meteorites of a sample derived from the depleted mantle on Mars. Nevertheless, we see a large range (greater than an order of magnitude) in the δD of merrillites and maskelynites of the Tissint ATS, which we argue is likely the result of processes occurring on Mars.

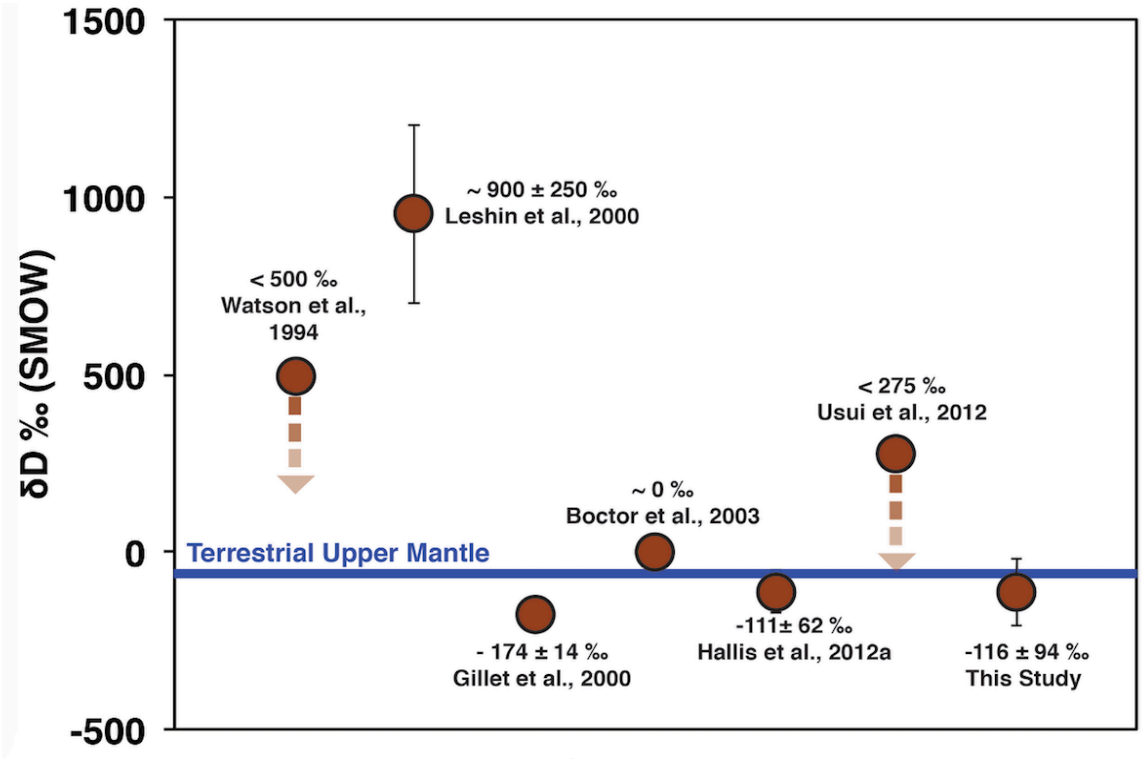

Figure 2.4. Estimates of δD of primitive (mantle) water on Mars based on analyses of minerals in the martian meteorites. The current best estimate of the δD value for the terrestrial upper mantle (-60‰; Clog et al., 2013) is shown as the horizontal blue line.

Each of the processes described in the previous section may have contributed to the hydrogen isotope systematics in Tissint, though it is difficult to deconvolve these effects. Nevertheless, the only processes among those discussed above that could produce the large δD variation seen in Tissint ATS merrillites and maskelynites (Figure 2.3) are either secondary alteration by martian crustal fluids or shock implantation of the martian atmosphere (or both). Given that both of these processes are expected to increase the resulting δD for martian rocks, we may reasonably conclude that the elevated δD in some of the analyses reported here results from these processes and that the lower end of the δD in our measurements represents the δD value of the Tissint depleted mantle source on Mars. To estimate the δD of this depleted mantle source end-member we must therefore assess the possible variation due to the other processes we discussed in the previous section. All processes described earlier result in an increase in the δD, with one exception: dehydration (H_2O loss) could decrease the δD of an originally hydrous Tissint parent magma. Based on studies of terrestrial igneous rocks, however, it is evident that such degassing of H_2O can fractionate the δD value of the parent magma only by ≤150‰ (De Hoog et al., 2009). Furthermore, since reducing conditions are thought to have prevailed for the Tissint parent magma ((Balta et al., 2015), dehydrogenation rather than dehydration is more likely during degassing and would have resulted in an increase in the magmatic δD. As we have argued that the data obtained here on the Tissint ATS are only minimally, if at all, affected by terrestrial contamination, it is reasonable to hypothesize that the lowest δD values reported here for Tissint ATS phases (i.e., -116 ± 94‰; Table 2.1), corresponds to that of its parent magma. This lowest δD value is (within error) similar to the current best estimate of the δD of the terrestrial depleted upper mantle (-60 ± 5‰; Clog et al., 2013). As such, we suggest that the D/H composition of Tissint's depleted martian

mantle source is similar to the Earth's depleted upper mantle. Figure 2.4 summarizes all previous estimates of the δD value for primordial water in the martian mantle, and includes the estimate presented in this study.

Mars has been characterized as a failed planetary embryo, having accreted mostly within the first ~2 Ma of Solar System formation (Dauphas and Pourmand, 2011), whereas Earth continued its accretion through runaway growth. Since their accretionary mechanisms are hypothesized to be different, the similarity of the D/H compositions of the source mantles of these two terrestrial planets could imply either that the accreting material for both had similar δD values or that water was added later (via a "late veneer") to both from a similar source. The CI chondrites have been suggested to be the major source of water on the Earth (Alexander et al., 2012) and Vesta (Sarafian et al., 2014); as such, the similarity of D/H ratio in the terrestrial and martian mantles would suggest that the CI chondrites could be the major source of water on Mars too. Finally, as discussed previously by Leshin (2000), if Mars started with a D/H ratio similar to that of the Earth, the exchangeable water reservoir on Mars would have had to experience ~80-90% loss to reach the present day D-enrichment in the martian atmosphere, i.e., the present-day inventory of exchangeable water on Mars is only 10-20% of its initial abundance.

2.5.5 Proposed scenario for the evolution of δD in Tissint. Assuming that the δD of the upper mantle of Mars is similar to that of the terrestrial upper mantle (as discussed in the previous section), Figure 2.5 provides a schematic illustration of the likely processes that have affected the δD values in the phases in Tissint. The parent magma of Tissint inherited the δD composition of its source in the martian mantle since partial melting and crystal fractionation do not fractionate hydrogen isotopes significantly (Bindeman et al., 2012). The trace element and radiogenic isotope systematics of Tissint indicate that it originated from a depleted

mantle source (Brennecka et al., 2014). As such, crustal contamination is unlikely to have affected the hydrogen isotope systematics of the Tissint parent magma to any significant degree.

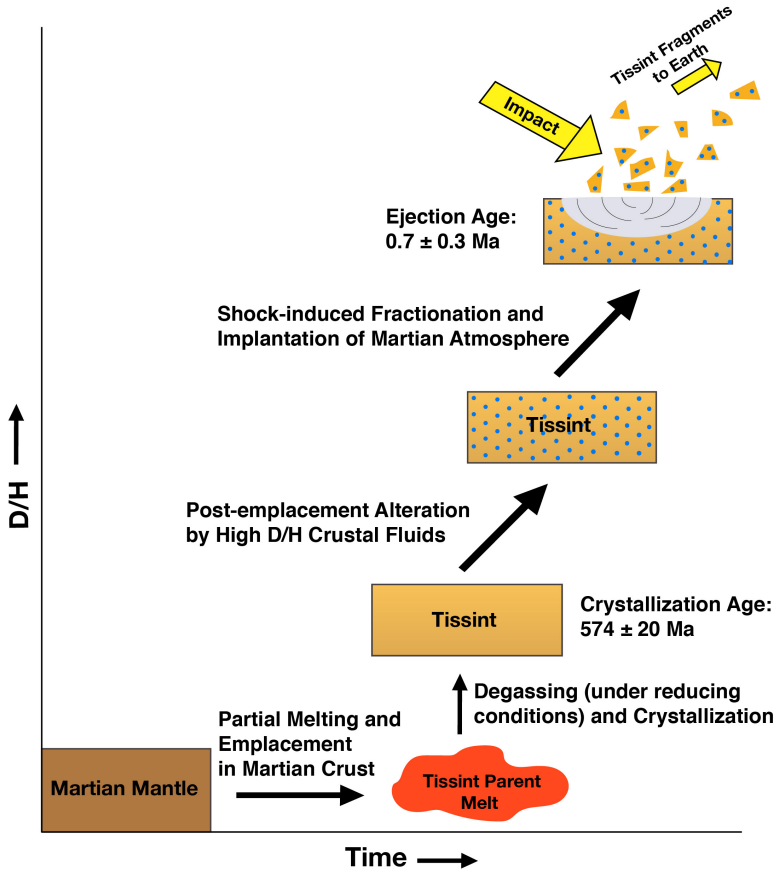

Figure 2.5. A schematic depiction of processes that likely affected the D/H ratios in Tissint at different stages in its magmatic and post-magmatic history. Partial melting in the mantle does not fractionate hydrogen isotopes to any significant degree; since water is expected to behave incompatibly during mantle melting, the water content of the Tissint parent melt will be higher than that in its source mantle. Subsequent magmatic degassing can fractionate the D/H ratio and lower the H_2O content of the parent melt; in the case of Tissint (thought to form under relatively reducing magmatic conditions; Balta et al., 2015), any degassing is likely to be in the form of dehydrogenation which would raise the D/H ratio in the parent melt. Crustal aqueous fluids on Mars are characterized by high δD owing to equilibration with the martian atmosphere. Therefore, interaction and sub-solidus exchange of hydrogen with such crustal fluids is likely to increase the δD (and water content) in Tissint phases. This process can take place anytime during the span of hundreds of millions of years, from the time of magmatic emplacement and crystallization (at 574 ± 20 Ma; (Brennecka et al., 2014b) till ejection from the martian surface due to impact (at 0.7

± 0.3 Ma; (Aoudjehane et al., 2012). At the next stage, during impact, hydrogen isotopes are additionally likely to fractionate in the rock; experiments suggest that this process may result in an increase in δD up to ~100 ‰ and may also increase the water content of the shocked phases. Furthermore, during the impact, martian atmospheric hydrogen could be implanted into the phases in the rock, causing an increase in their δD. All these processes probably contributed to varying degrees to the δD range reported here within and among Tissint phases, but the lowest δD values recorded in these phases are likely to be close to the initial magmatic value. See text for details.

If the Tissint parent magma was hydrous, then the extent and direction of δD evolution would depend on whether this magma experienced dehydration (up to ~150‰ decrease in δD; De Hoog et al., 2009) or dehydrogenation (up to ~800 to 1000‰ increase in δD(Saal et al., 2013; Sharp et al., 2013; Tartèse et al., 2013). Following crystallization in a near-surface environment, Tissint likely interacted with crustal fluids with high δD values (~+5000 ‰; (Leshin et al., 2013; Webster et al., 2013; Mahaffy et al., 2015) and under conditions of relatively low fluid:rock ratios. This process would have resulted in variable increases in the δD of the primary igneous minerals in Tissint through incomplete exchange of hydrogen with these fluids. Such fluid-rock interactions would have occurred anytime between the time of its crystallization (~575 Ma; Brennecka et al., 2014) until the time when it was ejected from Mars as a result of an impact event (at ~0.7 Ma; Aoudjehane et al., 2012). During this time period it may also have experienced multiple impact events that could have variably increased the δD of mineral phases depending on the degree of shock experienced during such events. The final (and most significant) impact event that ejected the rock from the martian surface ~0.7 Ma ago is also likely to have caused variable increases in the δD in Tissint phases. Therefore, the inter- and intra-grain variations in δD in various Tissint phases reported here are considered to be a combined record of the superposed effects of each the above processes at different times in the history of this meteorite.

2.5.6 Water contents of Tissint phases and its parent magma. The H_2O contents reported here in the various phases in Tissint have the potential for furthering our understanding of the volatile inventory of martian reservoirs. Nevertheless, it must be emphasized that there is a significant caveat to the following discussion. As discussed in a previous section, a variety of post-magmatic processes could have altered the water contents of primary igneous minerals in Tissint. Therefore, inferences about the water content of the Tissint parent magma that are based on the assumption that the water contents measured in Tissint phases have not been significantly altered by secondary processes may not be correct. Given this caveat, such inferences must be considered tentative until such time as there is further confirmation of the magmatic water content of phases in Tissint.

A recent study of the water content of magmatic apatites in the enriched shergottite Shergotty and the depleted shergottite QUE 94201 suggested that the water contents of both the geochemically enriched and depleted shergottite parent magmas were similar (730-2870 ppm) and their mantle sources were estimated to contain 73-290 ppm water (McCubbin et al., 2012). In contrast, (Usui et al., 2012) measured water contents in melt inclusions from an enriched shergottite (LAR 06319) and a depleted shergottite (Y980459) and argued that the source mantle of the depleted shergottites was comparatively water-poor (≤116 ppm water), and the enriched shergottite parent magmas derived additional water from crustal assimilation. A more recent study of water contents in shergottites using apatite-based melt hygrometry suggests that parent melts of the enriched and depleted shergottites have distinctly different water contents and the mantle source reservoir of the depleted shergottites may be drier than that of the enriched ones (McCubbin et al., *in press*). As Tissint is a highly REE-depleted shergottite (Balta et al., 2015),

the model proposed by these authors predicts low water content (up to ~200 ppm) in the Tissint parent magma. However, this predicted water content is substantially below that measured here in the Tissint melt inclusion.

A single olivine-hosted melt inclusion was measured in this study and shows δD ranging from +904 to +1397‰ and H_2O contents of 0.15 to 0.20 wt.%. These H_2O abundances are elevated relative to those reported for melt inclusions in the depleted shergottite Y980549, but similar to that for a melt inclusion in the enriched shergottite LAR 06319 ((Usui et al., 2012). Although, as discussed previously, our calibration for determining H_2O contents leaves the potential for significant uncertainties, these abundances are a factor of 5-10 times those reported for melt inclusions in the depleted shergottite Y980459; even the most significant corrections estimated by us (see "Methods" section) would suggest that the Tissint melt inclusions are far more water-rich than those reported for Y980459. The δD in this melt inclusion is also elevated relative to that proposed for the depleted martian mantle by several previous studies (e.g., Boctor et al., 2003; Hallis et al., 2012a; (Usui et al., 2012); it is, however, similar to that proposed by Leshin (2000) for the martian mantle. Usui et al. (2012) interpreted the relatively high water content and elevated δD in the melt inclusion in the enriched shergottite LAR 06319 as evidence for interaction with a high-δD martian crustal reservoir. However, Tissint is a depleted shergottite and there is no evidence of any contamination of the Tissint parent magma prior to or during crystallization (Balta et al., 2015). Therefore, the elevated δD and water content in the Tissint melt inclusion cannot be from assimilation of martian crust into the parent magma. In fact, this melt inclusion is unlikely to record magmatic conditions given that it is crystalline, has cracks and the host olivine is highly fractured (Figure 1b). Moreover, the variation in the δD (+904 to +1397‰) and the H_2O content (0.15 to 0.20 wt.%.) within the melt inclusion

further suggests that post-crystallization processes may be responsible for both. Subsolidus processes such as interaction (and partial equilibration) with martian crustal fluids or diffusive loss of hydrogen from the inclusion could produce the elevated δD in this melt inclusion. Such processes could additionally account for the difference in the δD values measured in this melt inclusion and those of olivines that host such inclusions (which are significantly lower) (Figure 3). Moreover, these processes would also have altered the H_2O content of this inclusion. As such, the H_2O concentrations reported here in the olivine-hosted melt inclusion (Table 1) are unlikely to be reliable indicators of magmatic water content for Tissint.

Additional, potentially more reliable, information on the H_2O content in the Tissint parent magma may be obtained from H_2O abundances measured in various phases in this shergottite. Water is able to substitute into the merrillite structure as a whitlockite component (Hughes et al., 2006) and our measured water contents of 0.04-0.38 wt.% in the Tissint ATS phosphates would suggest a substantial whitlockite component. Taken at face value, such a component would suggest equilibration with hydrothermal or aqueous fluids at subsolidus temperatures below ~1050 °C (McCubbin et al., 2014; Hughes et al., 2008). However, we have not established the structural position of the water within this phosphate mineral and whitlockite components have not previously been verified in martian meteorites using structural data (McCubbin et al., 2014); without a full characterization of the mineral structure we hesitate to suggest that these high water contents reflect a substantial whitlockite component and thus have adopted the term "merrillite" as the appropriate description for this phosphate mineral. Even accepting a possible large uncertainty on merrillite water contents as for the other phases, our measured water contents are significantly higher than those reported recently for merrillites from Shergotty (McCubbin et al., 2014). As discussed in an earlier section, the lack of

correlation between water content and δD in Tissint ATS merrillites implies minimal, if any, contribution from terrestrial contamination (Figure 2a). Moreover, since the measured δD values are far below those estimated for martian crustal fluids in equilibrium with the Mars atmosphere (Usui et al., 2012, 2015), the high water contents in this mineral are unlikely to reflect solely addition during shock processes or interaction with such crustal fluids. Alternatively, however, it is possible that the δD values (which are in the range of +272 to +2418 ‰) and the relatively high water contents in the Tissint ATS merrillites are the result of partial equilibration with aqueous fluids derived from a distinct martian reservoir comprised of hydrated crust or ground ice (Usui et al., 2015). In any case, in addition to the above potential complications, we cannot specifically quantify the parent magma H_2O content based on these merrillites due to the lack of constraints on mineral/melt partitioning.

Partition coefficients for water have been measured experimentally for both olivine and plagioclase, potentially allowing these phases to be used as our best constraints on the Tissint parent magma water contents. Olivines may be particularly useful in this analysis as they are among the earliest crystallizing minerals in Tissint and their cores likely spent substantial time at magmatic temperatures prior to crystallization of other phases, which should eliminate possible kinetic effects on water incorporation (Balta et al., 2015). However as discussed in the "Methods" section, water contents in anhydrous phases such as olivine may be overestimated by a factor of 2 even after the correction for matrix effects. Nevertheless, if we take the H_2O contents reported in Table 1 at face value, the magmatic water content of Tissint olivines may be assumed to be in the range of 0.005-0.035 wt.%. Partition coefficients for the incorporation of water in olivine have been measured on natural and experimental olivines and are typically very low (e.g.,(Hauri et al., 2006; Johnson, 2006); use of these partition coefficients produces parental magma H_2O

contents >1 wt.%. However, all our analyses of olivines (regardless of water contents) show elevated δD values, a possible indication of either selective loss of H relative to D from the olivines through diffusive loss after water was able to degas from the Tissint magma following olivine crystallization, or subsolidus alteration by D-rich martian crustal fluids. In either scenario, the measured water contents in the ATS olivines are unlikely to reflect primary magmatic compositions.

Previous estimates for the water partition coefficient for plagioclase have large ranges (Johnson, 2006). A partition coefficient of 0.007 was recently used to estimate the water content of lunar parental magmas (Hui et al., 2013), while a value of 0.004 was used for higher-Na feldspars from Mt. St. Helens (Johnson, 2005). Moreover, the H_2O contents reported here in ATS maskelynites have a wide range (0.003-0.054 wt.%; Table 1). As illustrated in Figure 2.3, the range in ATS maskelynite compositions is likely to be the result of mixing between three end-member components (represented by the apices of the gray triangle in Figure 3): 1) a high δD, high water component representing martian crustal fluids, 2) a low δD, low water component representing the primary magmatic mineral composition, and 3) a low δD, high water component that may represent either a terrestrial-like martian component (such as a late-stage magmatic fluid enriched in water and volatiles) or terrestrial contamination. Given this, the lowest H_2O content reported here in ATS maskelynites (~30 ppm; Table 2.1 and Figure 2.3) is likely to be closest to the magmatic composition of the original plagioclase. We note again that more appropriate blank and calibration corrections may be necessary and could result in lowering the H_2O contents reported here in the ATS maskelynites. As such, the value of 30 ppm for the H_2O content for the primary magmatic plagioclase (based on the lowest value measured here for the ATS maskelynites) is still likely to be an upper limit. If this value is used, partition coefficients in the range of 0.004 to 0.007 yield

H_2O contents in the range of 0.4 to 0.8 wt.% for the melt in equilibrium with the Tissint plagioclase. Unlike olivine, plagioclase was formed later in the crystallization sequence of Tissint (Balta et al., 2015), and therefore a correction additionally needs to be made for a substantial degree of crystal fractionation (possibly ~80-90%) to obtain the true water content of the Tissint parent magma. Assuming ~80% crystal fractionation prior to the onset of plagioclase, and 30 ppm as an upper limit on the abundance of H_2O in the original magmatic plagioclase, the H_2O content in the Tissint parent magma is estimated to be ≤0.2 wt.%.

In summary, based on the water contents of the nominally anhydrous phases analyzed here and our estimated corrections, the Tissint parent magma H_2O content is likely to be ≤0.2 wt. %. This upper limit is about an order of magnitude higher than the water content suggested for the parent magmas of the depleted martian shergottites by (Usui et al., 2012) and McCubbin et al. (*this issue*), but it is nevertheless consistent with these studies.

2.6 Conclusions

We analyzed the hydrogen isotopic compositions of various phases in Tissint, one of the freshest martian falls. This meteorite provides a unique opportunity to analyze a martian crustal sample with minimal terrestrial contamination. In order to assess the effects of laboratory contamination on the hydrogen isotope compositions of phases in the martian meteorites during sample preparation, a comparison was made between traditional sample preparation techniques involving mounting in epoxy and epoxy-free anhydrous sample preparation methods. We see a strong effect of laboratory-based sample contamination on igneous minerals in Tissint that are highly fractured by shock. An anhydrously prepared section shows minimal, if any, evidence of such contamination, and δD values in phases analyzed in this

section range from values that are terrestrial upper mantle-like to highly elevated values approaching that of the martian atmosphere. Various processes such as magmatic degassing, secondary aqueous alteration by crustal fluids, or shock processes may have contributed to the large δD range in the Tissint phases. Taking into account the effects of processes that are likely to have affected the δD values of Tissint phases, we argue that the lowest δD value of -116 ± 94‰ measured in the Tissint ATS is likely representative of the martian mantle. As such, we conclude that martian mantle has a similar hydrogen isotopic signature to the terrestrial upper mantle, and suggest that irrespective of distinct accretion mechanisms, the primordial water on Mars and Earth had similar sources.

Table 2.1

The H_2O content and hydrogen isotope compositions of phases analyzed in the Tissint polished thin section (PTS) and anhydrously prepared thick section (ATS). For each analysis on a particular phase, the number indicates a distinct grain and the alphabet indicates a different spot on the same grain.

	H_2O Content (wt. %)[3]	δD (‰)[2]
PTS:		
Phosphates		
Merrillite-1a	0.96	119 ± 9
Merrillite-1b	0.69	21 ± 26
Merrillite-2	0.38	524 ± 16
Merrillite-3	0.35	303 ± 30
Merrillite-4	0.34	212 ± 25
Merrillite-5	0.89	111 ± 12
Merrillite-6	0.91	-105 ± 20
Merrillite-7	0.29	339 ± 25
Merrillite-8	0.67	183 ± 26
Maskelynites		
Maskelynite-1	0.015	461 ± 31
Maskelynite-2	0.031	290 ± 29
Maskelynite-3	0.013	744 ± 30
Maskelynite-4	0.620	-51 ± 24
Maskelynite-5	0.014	887 ± 27
Maskelynite-6	0.023	1340 ± 22
Maskelynite-7	0.061	119 ± 24
Olivines[3]		
Olivine-1	*0.037*	-43 ± 9
Olivine-2	*0.035*	-121 ± 5
ATS:		
Phosphates		
Merrillite-1	0.09	1834 ± 33
Merrillite-2	0.13	1308 ± 39
Merrillite-3	0.05	1960 ± 42
Merrillite-4	0.38	272 ± 28
Merrillite-5	0.05	1679 ± 35
Merrillite-6	0.19	2308 ± 19
Merrillite-7	0.07	1967 ± 25

Merrillite-8	0.22	2418 ± 15
Merrillite-9	0.13	848 ± 15
Merrillite-10	0.04	522 ± 27
Maskelynites		
Maskelynite-1	0.007	-116 ± 94
Maskelynite-2	0.005	1342 ±74
Maskelynite-3	0.054	839 ± 41
Maskelynite-4	0.003	135 ± 121
Maskelynite-5	0.025	2570 ± 39
Maskelynite-6	0.017	2839 ± 27
Maskelynite-7	0.007	3682 ± 40
Maskelynite-8	0.025	651 ± 36
Maskelynite-9	0.009	-45 ± 113
Olivines[3]		
Olivine-1a	*0.007*	470 ± 37
Olivine-1b	*0.005*	380 ± 34
Olivine-1c	*0.016*	12 ± 53
Olivine-2	*0.019*	127 ± 38
Olivine-3	*0.012*	106 ± 46
Melt Inclusion		
MI-1a	0.197	1283 ± 27
MI-1b	0.150	1397 ± 22
MI-1c	0.168	904 ± 16

[1]The external reproducibility (2SD) of the measured H_2O contents is estimated to be ±20% based on repeat analyses of the standards used in this study (see text for details).

[2]The uncertainty (2σ) in the δD is from counting statistics only.

[3]The H_2O content of olivines has been corrected for matrix effect as described in the Methods section.

CHAPTER 3

ISOTOPIC INVESTIGATIONS OF CALCIUM-ALUMINUM RICH INCLUSIONS

3.1 Introduction to Calcium-Aluminum-rich Inclusions and its components.

Primitive meteorites preserve petrographic and geochemical records of early events that shaped our Solar System. They contain refractory inclusions, known as Calcium-Aluminum-rich Inclusions (CAIs), which are the first solids to have formed within the proto-solar nebula (Amelin et al., 2002; Amelin et al., 2010; Bouvier and Wadhwa, 2010; Connelly et al., 2012). Elemental and isotopic abundances of these inclusions record early events in the Solar System. The refractory minerals and textures of the CAIs suggest they formed as high temperature condensates in a reducing environment (Grossman, 1972). Thermodynamic models indicate that the mineralogy of CAIs is similar to the first mineral phases expected to condense out of a gas of solar composition (Grossman, 1972; Ebel and Grossman, 2000).

Absolute high-resolution dating of CAIs has been undertaken using the Pb-Pb radiogenic chronometer, which shows them to be the oldest solids in the Solar System, forming at 4568-4567 Ma. (Amelin et al., 2002; Amelin et al., 2010; Bouvier and Wadhwa, 2010; Bouvier et al., 2011; Connelly et al., 2012). Another useful high-resolution dating technique is the ^{26}Al-^{26}Mg short-lived chronometer, which has been used extensively for relative dating of CAIs (e.g., (MacPherson et al., 1995; Bizzarro et al., 2004; Jacobsen et al., 2008). Most CAIs have a constant canonical initial $^{26}Al/^{27}Al$ ratio of $\sim 5 \times 10^{-5}$ (MacPherson et al., 1995). These CAIs occur in all chondrites, and are particularly abundant in carbonaceous chondrites. Many CAIs have a uniform Solar O isotopic composition and they also show evidence for in situ decay of live ^{10}Be, which is a produced during irradiation near the protosun, suggesting that they formed in a restricted region near the protosun (MacPherson, 2005). Some CAIs show evidence for later thermal processing,

followed by cooling with slow cooling rates (2-50C°/hr), for up to 0.7 Ma (MacPherson et al., 2012).

3.1.1 Types of refractory inclusions. Based on their composition and texture, normal CAIs are classified as type A, type B, or type C (MacPherson, 2014). Type A inclusions are further classified, as fluffy type A, or compact type A. Fluffy type A CAIs are unmelted aggregates of hibonite, spinel, perovskite and melilite, which condensed from a gas of solar composition (Grossman, 1972; Ebel and Grossman, 2000). They are typically ^{16}O-rich and have irregular shapes. The compact type A CAIs contain spinel, perovskite, Al-Ti rich pyroxene, rhönite and coarse-grained melilite. They are ^{16}O-rich and have rounded shapes. They formed through crystallization from a melt following evaporation of nebular dust and gas. Type B inclusions formed by crystallization from molten droplets. They are unique to CV carbonaceous chondrites, and show evidence for multiple thermal events (Grossman, 1975). They are further classified as type B1, type B2 and type B3 that grade into each other. Minerals in type B CAIs show variable degrees of ^{16}O enrichment. Type B1 CAIs are zoned, containing melilite, spinel, Al-Ti rich pyroxene, and sometimes glass that formed rapidly from crystallization from a homogenous melt. Type B2 CAIs have higher anorthite/melilite ratio and are more silica-rich than Type B1. Their mineralogy and texture suggests that they have crystallized slowly from isolated melt pockets of their precursor material (Grossman, 1975). Type B3 are rare forsterite-bearing inclusions that are only found in CV and CB chondrites. The type B3 CAIs contain a core of ^{16}O-rich spinel, pyroxene and forsteritic olivines and a mantle of ^{16}O-depleted anorthite and melilite mantles. Type C CAIs are coarse grained with diverse textures and mineralogies. They contain ^{16}O-poor melilite, anorthite, pyroxene and spinel. Their relatively high volatile content suggests that

they melted under either high pressures or high gas/dust ratios. They are thought to be the precursors for Al-rich chondrules (MacPherson, 2016).

Amoeboid Olivine Aggregates (AOAs) are another set of unusual refractory inclusions found in primitive meteorites (Grossman and Steele, 1976). These are olivine-rich fine-grained inclusions that are less refractory than other CAIs. Other AOA minerals include spinel, Al-rich pyroxene, anorthite, and rarely melilite. It has been suggested that they likely formed in the same region as the normal CAIs but experienced cooler condensation temperatures (Fagan et al., 2004).

Some CAIs are classified as FUN (Fractionated and Unknown Nuclear effects) inclusions, based on their unusual isotopic compositions (Wasserburg et al., 1977; MacPherson, 2014). Their mineralogies and textures are similar to normal CAIs, however their isotopic compositions differ significantly. For example, they show large mass-dependent fractionation in O, Mg, and Si isotopes (Wasserburg et al., 1977) as well as non-linear isotopic anomalies in Ca, Ti, Cr, Sr, Ba, and Nd systems (Birck, 2004). Large mass-fractionation effects resulting in heavy isotopic composition of O, Si, and Mg suggest a high temperature origin, possibly indicating evaporative environments. FUN inclusions lack evidence for ^{26}Al, suggesting that they formed before normal CAIs, prior to the injection of ^{26}Al into the early Solar System (Sahijpal and Goswami, 1998), or they formed in a spatially distinct region that lacked ^{26}Al (Holst et al., 2013).

The CM carbonaceous chondrites also contain hibonite-bearing inclusions, namely PLACs (PLAty hibonite Crystals) and SHIBs (Spinel-HIBonite spherules). These inclusions are smaller than normal CAIs (~ 50-100 μm). PLACs lack evidence for in situ decay of ^{26}Al (Liu et al., 2012), however they exhibit large nucleosynthetic non-linear anomalies in Ti and Ca isotopes, whereas SHIBs show subcanonical initial

$^{26}Al/^{27}Al$ ratios and large non-linear anomalies in Ca, Ti, and Si isotopes (Ireland et al., 1988).

3.1.2 Wark-Lovering rims. CAIs are surrounded by multi-mineralic layers, which are termed as 'Wark-Lovering rims' (Wark and Lovering, 1977). This rim sequence represents unique yet universal events in the early Solar System. They are composed of refractory minerals such as hibonites, spinels, perovskites, melilites, and Al-rich pyroxenes. The WL rims were first described by (Wark and Lovering, 1977), where type A CAIs exhibit rim sequence of Fe-rich spinel + perovskite/anorthite (altered to nepheline, sodalite etc)/Ti-Al rich pyroxenes/Al-rich diopside. Type B CAIs show hibonite/Fe-rich spinel/nepheline +sodalite. Classically defined WL rims contain at least spinel, melilite (and/or its alteration products) and pyroxene (Wark and Lovering, 1977; Wark and Boynton, 2001). Various mechanisms have been proposed to account for WL rim mineralogy and their isotopic signatures;

1. Condensation: Textural studies and high-spatial-resolution focused-ion-beam transmission electron microscopy (FIB TEM) of WL rims show a complex mixture of polycrystalline grains, with the presence of subhedral grains suggesting a condensation origin. (Toppani et al., 2006; Stroud et al., 2007; Zega et al., 2007; Ito et al., 2010; Bolser et al., 2016). Oxygen isotopic variations in WL rims suggest that rims are a product of condensation processes as CAIs cycled between ^{16}O-rich and ^{16}O-poor nebular reservoirs, incorporating different isotopic signatures in their rims (Ito et al., 2010; Simon et al., 2016b).
2. Crystallization from a melt: Textural studies and FIB TEM studies of WL rims show a complex mixture of polycrystalline material, and the presence of triple junctions and subhedral grains suggest formation from melt, which has been considered as evidence for flash heating, caused by mechanisms such as

shock waves (Stroud et al., 2007; Zega et al., 2007; Ito et al., 2010). Oxygen isotopic variations measured in WL rims have been explained by flash heating and subsequent re-equilibration with nebular gas (Hirai et al., 2002; Ito and Messenger, 2008).

3. Evaporation residue: Based on their refractory element compositions, WL rims were considered to be a consequence of flash heating (at >2500 K for <2 s) and were thought to represent the evaporation residues from such events (Wark and Boynton, 2001).
4. Nebular alteration: Growth of layers as a result of chemical gradients present during alteration of the interiors of inclusions in the nebula (MacPherson et al., 1982). This hypothesis suggests that the rims formed as a product of condensation in a ^{16}O-rich environment and the ^{16}O-poor component was introduced later as a product of alteration and disturbance (Cosarinsky et al., 2005; Yoshitake et al., 2005).

Multiple mechanisms: Contradicting textural, elemental and isotopic evidence suggest multiple mechanisms, as these analyses were conducted on different mineral layers (MacPherson et al., 1982; Wark and Boynton, 2001; Simon et al., 2011; Simon et al., 2016a). Therefore, the WL rim sequence likely formed as a consequence of multiple processes (Davis et al., 1986; Murrell and Burnett, 1986). WL rims in many CAIs show alteration phases, however there are CAIs with WL rims consisting of only high temperature mineral phases, therefore alteration events most likely post date the WL rims formation.

This diversity of refractory inclusions found in primitive chondrites records various processes that were active in the early Solar System. This and the following three chapters focus on isotopic investigations of normal CAIs. By determining their chronology and mass dependent as well as non-mass dependent isotopic anomalies,

I attempt to determine the nature of these processes and the timescales over which these processes were active. CAIs record isotopic variations in many elemental systems. Broadly, these anomalies can be attributed to following processes:

1. Radioactive decay of short-lived and long-lived radionuclides (e.g., ^{26}Al, ^{41}Ca, ^{238}U)
2. Nucleosynthetic anomalies (due to incomplete mixing of presolar components). (e.g., ^{48}Ti, ^{54}Cr, ^{96}Zr)
3. Mass dependent fractionation (due to primary (evaporation and condensation) as well as secondary (thermal and aqueous alteration) processes). (e.g., Mg and Si isotopes).

3.2 ^{26}Al-^{26}Mg relative age dating of Wark-Lovering rims

The WL rims have been described as the *'early Solar System stratigraphy*' by G. J. Wasserburg (Wark and Lovering, 1977). The rims consist of one or more mineral layers, which are consistent in thickness around the CAIs, including over sharp and irregular corners. WL rims are absent around the broken regions of the CAIs. They are present around CAIs from different chondritic groups (e.g., Allende (CV3), Murchison (CM2) and Lance (CO3.5)) (Frost and Symes, 1970; Grossman, 1975; Grossman et al., 1977); however other chondritic components like chondrules do not exhibit WL rims around them.

Oxygen isotopic studies of some WL rims show heterogeneous oxygen isotopic compositions, which suggest that the rim sequences tapped different oxygen reservoirs (Ito and Messenger, 2008; Simon et al., 2011; Simon et al., 2016a). This discovery is significant because it predicts a protoplanetary disk that was heterogeneous and dynamic where CAIs may have journeyed a significant distance over the duration of rim formation. It is fundamental to put time constraints over

such a large-scale transport event in order to understand the origin and formation conditions of the WL rims.

One of the most commonly used chronometer for chondritic components is the ^{26}Al-^{26}Mg system. 26-Aluminum is a short-lived radionuclide (half-life of ~0.73 My) that undergoes β decay to form ^{26}Mg. This isotope system has been used to obtain the relative chronology of early Solar System events with sub-million-year precision (e.g., (Young and Galy, 2004)). Analysis of many CAIs shows that the initial Solar System abundance of ^{26}Al in terms of the ^{26}Al/^{27}Al ratio was ~5 x 10^{-5}, and that these refractory inclusions were formed within a very narrow time interval on the order of less than a few hundreds of thousands of years (MacPherson et al., 1995; Bizzarro et al., 2004; Jacobsen et al., 2008; Villeneuve et al., 2009). The ^{26}Al-^{26}Mg chronometer has the potential to provide high-resolution time constraints on WL rim formation. However, one of the limiting factors in establishing the chronometry of these rims is their small size. Their total thickness varies from 50-200 microns, with individual layers being 10s of microns thick. The application of the high-spatial-resolution in situ secondary-ion mass spectrometry (NanoSIMS) provides an opportunity to use the Al-Mg chronometer on WL rims to date the relative formation time of these rim sequences. NanoSIMS has revolutionized the field of isotope cosmochemistry because it allows spatial resolution of 10s to 100s of nanometers (see review by (Zinner, 2003). Recent studies of the Al-Mg system using NanoSIMS 50L show that it can provide precision on Mg isotopes corresponding to time resolution of 0.4-0.6 million years (Ito and Messenger, 2010). Such spatial resolution coupled with high temporal resolution is critical to date individual layers in WL rims, making NanoSIMS the only technique available currently for this purpose.

In chapter 4, I discuss ^{26}Al-^{26}Mg relative chronology of two CAIs from NWA 8323 (CV3 oxidized carbonaceous chondrite) and their WL rims. The results of this

study suggest that these WL rims formed ~2-3 Ma after CAI formation. These results suggest that CAIs remained free floating in the solar nebula for at least 2-3 Ma, before being accreted onto their parent bodies. Moreover, some mineral layers from the rims may have formed contemporaneously with chondrules, possibly by the similar transient heating mechanisms.

3.3 Zirconium Nucleosynthetic Anomalies in CAIs

Nucleosynthetic anomalies have been identified in various meteoritic components in many elemental systems including Ca, Ti, Cr, Sr, Ba, Zr, Mo, Hf, Gd, Dy, and Ru etc (Birck, 2004). These non-linear isotopic variations suggest that there were multiple inputs of extra-stellar material in the early Solar System. Determination of these nucleosynthetic variations answers questions about the following;

a. The origin of these anomalies,
b. The carrier phases that brought these anomalies into our Solar System,
c. The mixing mechanisms and timescales of mixing of these carrier phases with the Solar System material and
d. The degree of preservation of these carriers phases in the meteoritic materials.

Chapter 5 presents results of high-precision Zr isotopic composition 11 CAIs from the Allende CV3-oxidized carbonaceous chondrite and four CAIs from CV3 (NWA 6991, and NWA 6619), and CK3 (NWA 4964 and NWA 6254) meteorites, using multicollector inductively coupled plasma mass spectrometer (MC-ICP-MS). This same set of CAIs has also been analyzed for other isotopic systems including Ti, Cr, Sr, Mo, Ba, Nd, Sm, Gd, and Dy (Brennecka et al., 2010; Brennecka et al., 2013; Mane et al., 2014; Mercer et al., 2015; Shollenberger et al., 2015; Mane et al.,

2016; Shollenberger et al., 2016), therefore this is the first attempt to study an extensive suit of nucleosynthetic anomalies and their possible stellar sources in the same sample set. Zirconium has five stable isotopes, ^{90}Zr, ^{91}Zr, ^{92}Zr, ^{94}Zr, and ^{96}Zr, of which four form primarily via the s-process (slow neutron capture process), whereas ^{96}Zr has a significant contribution of r- process nucleosynthesis. The Zr isotopic composition of 14 out of 15 CAIs shows identical excess (within analytical uncertainty) in ^{96}Zr, suggesting that the CAI-forming region was homogenous, however, distinct than the terrestrial and bulk chondritic composition. Additionally, one CAI from NWA 6254 (CK3 chondrite) reported here shows a lesser enrichment in ^{96}Zr, and excess in ^{92}Zr, which is a decay product of a short-lived radionuclide ^{92}Nb (half-life ~37 Ma). The Nb-Zr isotopic systematics of CAIs reported here defines a Solar System initial ^{92}Nb/^{93}Nb of $(1.31 \pm 0.72) \times 10^{-5}$. These results suggest injection of supernova material into the early Solar System.

3.4 Mass dependent Mg isotopic variations in CAIs

CAIs are the oldest solids that have been dated using long-lived Pb-Pb absolute chronometry, with a high precision (within ± 0.16 Ma) (Amelin et al., 2002; Amelin et al., 2010; Bouvier and Wadhwa, 2010; Connelly et al., 2012). This dating method assumes a constant U isotopic ratio (^{238}U/^{235}U = 137.88) for early Solar System material. However, it was recently shown that ^{238}U/^{235}U varies significantly in CAIs, affecting the calculated age by up to 6 Ma (Brennecka et al., 2010). This variation was attributed to the presence of short-lived ^{247}Cm in the early Solar System that decays to ^{235}U ($t_{1/2}$ ~15.6 Ma) (Brennecka et al., 2010; Tissot et al., 2016). However, other processes such as mass-dependent isotopic fractionation caused by thermal and/or secondary alteration processes, and incomplete mixing of nucleosynthetic carriers with U isotopic anomalies could also produce the observed

heterogeneity in U isotopes (Amelin et al., 2009; Connelly et al., 2012). As U has only two primordial isotopes, it is difficult to distinguish between the mass-dependent isotopic fractionation and non-mass-dependent isotopic anomalies. In order to evaluate whether thermal processes (during evaporation/condensation) and/or secondary alteration processes are responsible for U isotopic variations, I analyzed mass dependent Mg isotopic composition of 11 CAIs from Allende meteorite. These CAIs were previous analyzed for their U isotopic composition (Brennecka et al., 2010). The thermal processes that could cause U isotopic fractionation are expected to fractionate Mg isotopes as well, resulting in correlation between the $^{238}U/^{235}U$ and $^{25}Mg/^{24}Mg$. The Mg isotopic composition of the Allende CAIs suggest that isotopic fractionation during thermal processes may have contributed to relatively small U isotopic variation in a subset of these samples, however, CAIs showing larger U isotopic variations do not correlate with $^{25}Mg/^{24}Mg$ ratios, suggesting that the U isotope variation in these samples may be dominated either by ^{247}Cm decay or by the presence of nucleosynthetic anomalies.

3.5 Future Work

Isotopic analysis is a powerful tool used in cosmochemistry to determine the nature of early Solar System events. In chapter 4, I report relative age dating of WL rims around two type B inclusions from NWA 8323 CV3 carbonaceous chondrite. As discussed in this chapter, mineral layers in WL rims likely formed by different mechanisms and therefore determining the chronology of WL rims sequences around different types of CAIs and CAIs from different primitive meteorites would improve our understanding of timescales of WL rim formation. Combining this age dating analysis with other techniques such as high-resolution microscopy, which enables determining the mechanisms of formation for the different mineral layers in the WL

rims, would provide a wholesome insight into the processes associated with the WL rim formation and the timescales over which they were active.

In chapter 5, I discuss Zr isotopic composition of 15 CAIs from 5 different carbonaceous chondrites. All of these inclusions show a homogenous yet distinctly anomalous isotopic composition in ε^{96}Zr and homogenously terrestrial isotopic composition for ε^{91}Zr and ε^{92}Zr, indicating isotopic homogeneity in the CAI forming region. However, one CAI, Homer from NWA 6254 (CK3) suggests some amount of heterogeneity in the Zr isotopic composition. This data set needs to be extended to include CAIs from other carbonaceous chondrites, to asses the isotopic homogeneity in Zr and other isotopic systems in the CAI-forming region. Isotopic analysis of CAIs to determine nucleosynthetic anomalies in multiple isotopic systems, coupled with age dating would provide a comprehensive picture of mixing processes and its timescales in the early Solar System.

CHAPTER 4

FORMATION TIMESCALES OF RIM SEQUENCES AROUND CALCIUM-ALUMINUM-RICH INCLUSIONS FROM A CV3 CHONDRITE

4.1 Introduction

Relative and absolute dating techniques suggest that CAIs are the first formed solids in the Solar System (Amelin et al., 2002; Bouvier and Wadhwa, 2010) that condense at high temperatures (most refractory phases starting at ~1750 K) (Grossman, 1972). CAIs are surrounded by a sequence of mono- or bi- mineralic layers, termed as WL rims (Wark and Lovering, 1977). These rims have been described as the early Solar System stratigraphy (Wark and Lovering, 1977). The width of these individual layers is less than a few microns, which make their isotopic analysis a major analytical challenge. Recent advances in analytical techniques, allowed analyses of Oxygen isotopes in the WL rims. In some CAIs, these rims show variation in the non-mass dependent oxygen isotopic composition, suggesting that during the rim formation event(s), the CAI was transported to different regions of the Solar nebula, with distinct oxygen isotopic signatures (Simon et al., 2011; Simon et al., 2016a). It is crucial to put time constraints over such a large-scale transport event in order to understand the origin and formation conditions of the WL rims..

The WL rims show a general mineralogical sequence spinel-perovskite-hibonite-melilite-anorthite-Al rich clinopyroxene- forsterite (Wark and Lovering, 1977). Alteration phases such as nepheline, anorthite, sodalite, grossular and wollastonite have also been reported in the rim sequences (MacPherson et al., 1982). Incomplete WL rims around broken CAIs and absence of rims around other chondritic components such as chondrules, suggest restricted spatial or temporal conditions of rim formation (Wark and Lovering, 1977). Various mechanisms have been proposed to explain the formation of WL rims, they include: 1) condensation

and subsequent accretion on the CAI surface (Ito and Messenger, 2008; Simon et al., 2011; Bolser et al., 2016; Simon et al., 2016a), 2) crystallization from a melt, by the flash-heating mechanisms (Keller et al., 2013), 3) formation as evaporation residues (Wark and Boynton, 2001), 4) growth of layers as a result of chemical gradients set up during alteration of the interior of inclusion, in nebular settings (MacPherson et al., 1982). Putting time constraints on the WL rim formation is crucial for understanding the transport of material in the early Solar System.

One of the main limiting factors in establishing the chronometry of these rim sequences is their size. Their total thickness varies from 50-200 μm, with individual layers being 10s of μm. The application of the high spatial resolution in situ Secondary Ion Mass spectrometry technique (NanoSIMS) provides a unique opportunity to use the Al-Mg chronometer on Wark-Lovering rims to date the relative formation time of these rim sequences. ^{26}Al is a short-lived radionuclide (half-life of ~0.705 My (Norris et al., 1983) that undergoes β decay to form ^{26}Mg. Therefore, this system can be used to obtain the relative chronology of early Solar System events with sub-million year precision (Young and Galy, 2004). I report high spatial resolution Al-Mg chronology of CAIs and their rims using a Cameca Amtek NanoSIMS 50L at ASU. Specifically, I analyzed two CAIs and their WL rims from the Northwest Africa (NWA) 8323, in order to determine the time difference between the formation of host CAIs and their WL rims. NWA 8323 is an oxidized CV3 carbonaceous chondrite, with a low shock grade as well as low weathering grade (Meteoritic Bulletin, 2014).

4.2 Methods

4.2.1 Scanning Electron Microscopy. Back scattered electron images and elemental abundances of mineral phases in CAIs and their WL rims were obtained

using JEOL JXA-8530F electron microprobe at Arizona State University (ASU) and FEI NOVA NanoSEM, 600 field emission gun Scanning Electron Microscope at the Smithsonian Institute. For both CAIs, BSE images, X-ray elemental MAPs and WDS spot analyses for major elemental abundances of different mineral phases were obtained.

4.2.2 Trace element analysis (Ba, Sr and Eu). Ba, Sr, and Eu abundances of WL rims and CAI interior were analyzed using Cameca 6f Secondary Ion Mass Spectrometer at ASU using protocols described in (Zinner and Crozaz, 1986; Hinton, 1990). A O^- primary beam with a primary current of ~15 nA was used to sputter an area of ~20 × 20 μm^2. A combination of contrast aperture of 400 μm and a field aperture with a diameter of 150 μm, was used to target the analysis area of ~4 μm. Si^+, $^{88}Sr^+$, $^{138}Ba^+$, and $^{151}Eu^+$ secondary species were detected on an electron multiplier in a pulse counting mode, with a mass resolving power of ~9000 (m/ Δm). Five cycles of mass calibration were performed before every analysis in order to minimize the possible hysteresis effects of the magnetic field control. Energy filtering was used to minimize the molecular interference, with an energy offset of -75V and energy slit width of 40 V. A pre-sputtering time of 300 seconds was applied before every analysis. In order to calculate elemental abundances in ppm, calibration was done using standard glasses, NIST 610, NIST 612 and NIST 614 and secondary standards ML3BG and KL2G (basalts glasses). Each analysis lasted for ~1.5 hours with 30 cycles containing 2 measurements each. The uncertainties reported here are1σ poisson error. $^{151}Eu^+$ has a molecular interference from $^{135}Ba^{16}O^+$ species that was corrected empirically with BaO^+/Ba^+ = 0.049 ratio (Hinton, 1990) reported for silicates, using methods described in (Zinner and Crozaz, 1986).

4.2.3 Oxygen Isotopic Analysis. The oxygen three-isotopic analysis was performed using the Cameca IMS-1280 ion microprobe at WiscSIMS lab, University

of Wisconsin, Madison, using analytical protocols similar to that of (Kita et al., 2010; Tenner et al., 2013). A Cs^+ beam with ~20 pA primary current was used to sputter ~ 3 × 4 μm^2 area to target smaller phases in the WL rims and CAI interior. The normal incidence electron gun was used for charge compensation. Each spot was presputtered for 180 seconds before the analysis. Secondary ion species of $^{16}O^-$ (Faraday cup), $^{17}O^-$ and $^{18}O^-$ (Electron multipliers) were simultaneously detected with typical $^{17}O^-$ count rates of ~6 – 8 × 10^3 cps . The contribution of the tailing of $^{16}OH^-$ interference on $^{17}O^-$ was corrected empirically, and was always lower than 0.3‰. San Carlos olivine (SCO) was used as a bracketing standard ($\delta^{18}O$ = 5.32 ‰; (Kita et al., 2010)) to correct for instrumental mass bias (each series of 10-15 sample analyses bracketed with 8 SCO analyses). Terrestrial spinel, gehlenitic and åkermanitic melilites, anorthite, diopside and synthetic fassaite glasses were used to correct for potential matrix effects. The measured $^{17}O/^{16}O$ and $^{18}O/^{16}O$ ratios were reported relative to VSMOW (Vienna Standard Mean Ocean Water). The errors reported here are 2 standard deviation (2SD) of the bracketing standard; SCO (~1 ‰ for $\delta^{17}O$, $\delta^{18}O$, and $\Delta^{17}O$). After the analyses, SIMS pits were verified using EPMA at ASU, to make sure there was no overlap with cracks, inclusions or other phases. The oxygen isotopic composition of the CAIs and their WL rims is reported in Table 4.2.

4.2.4 Al-Mg analysis. Mg isotopic analysis was conducted at Secondary Ion Mass Spectrometry (SIMS) labs at ASU using Cameca NanoSIMS 50L. Gold or carbon-coated polished thick sections of samples were sputtered by a 16keV primary O^- beam with a primary current of ~20 to 50 pA. The primary beam was rastered over 5 × 5 μm areas on the sample. Positive secondary ions were collected from the central 2.5 × 2.5 μm by using electronic gating. Positive secondary ions of $^{24}Mg^+$, $^{25}Mg^+$, $^{26}Mg^+$ and $^{27}Al^+$ were collected simultaneously using electron multipliers, in

isotope ratio mode. Potential isobaric interferences such as ^{23}NaH, $^{12}C_2$, ^{24}MgH, $^{13}C_2$, and $^{12}C^{14}N$ are completely resolved using a mass resolving power of <9000. We used the NMR (Nuclear Magnetic Resonance) tool, to regulate magnetic field stability, within a session the variation in the magnetic field was >10 ppm. The variation in the magnetic field was < 10 ppm for the entire session. The raw ratios were corrected for dead time. The instrumental mass bias was corrected using terrestrial standards. Analysis time varied between 30-90 minutes per spot for different mineral phases. The long-term external reproducibility of $\delta^{26}Mg^*$ on San Carlos olivine is 3.24‰ (Figure 4.1a) and on Lake County plagioclase is 11.9 ‰ (Figure 4.1b). The Mg isotopic composition and Al/Mg ratios of different mineral phases in CAIs and their WL rims are reported in table 4.1.

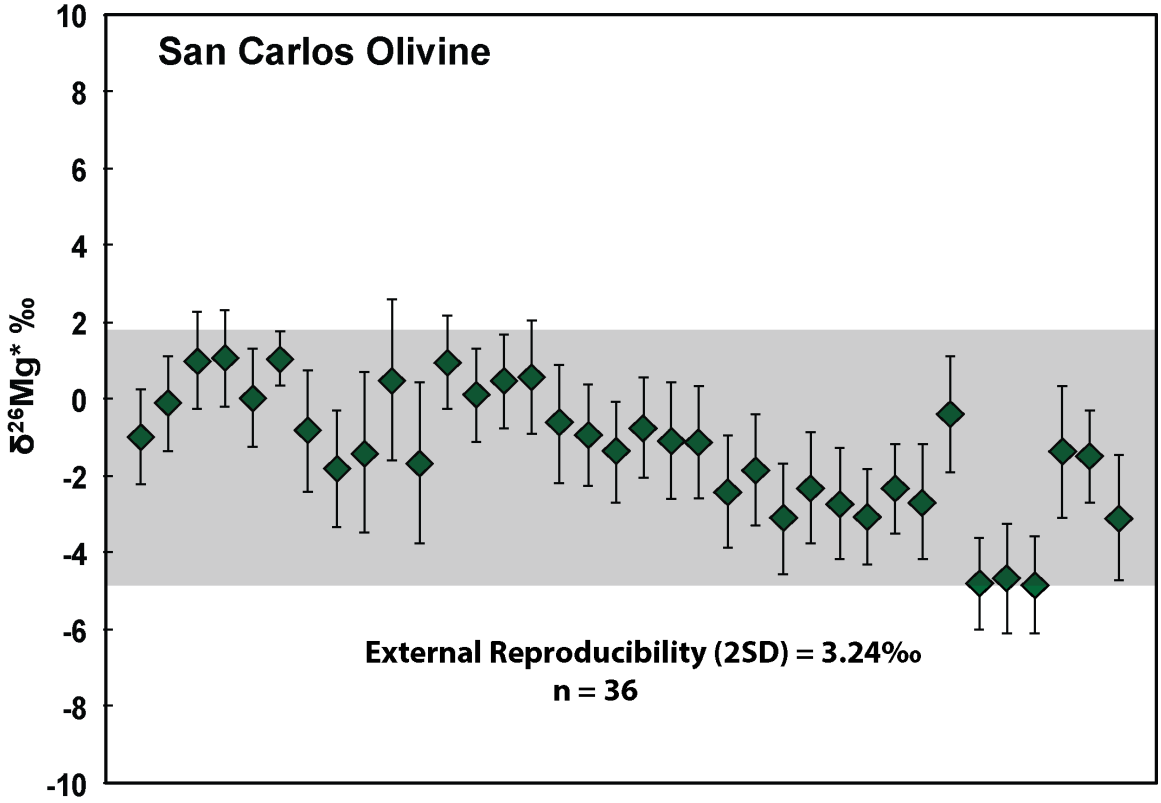

Figure 4.1a. External reproducibility of $\delta^{26}Mg^*$ on San Carlos olivine

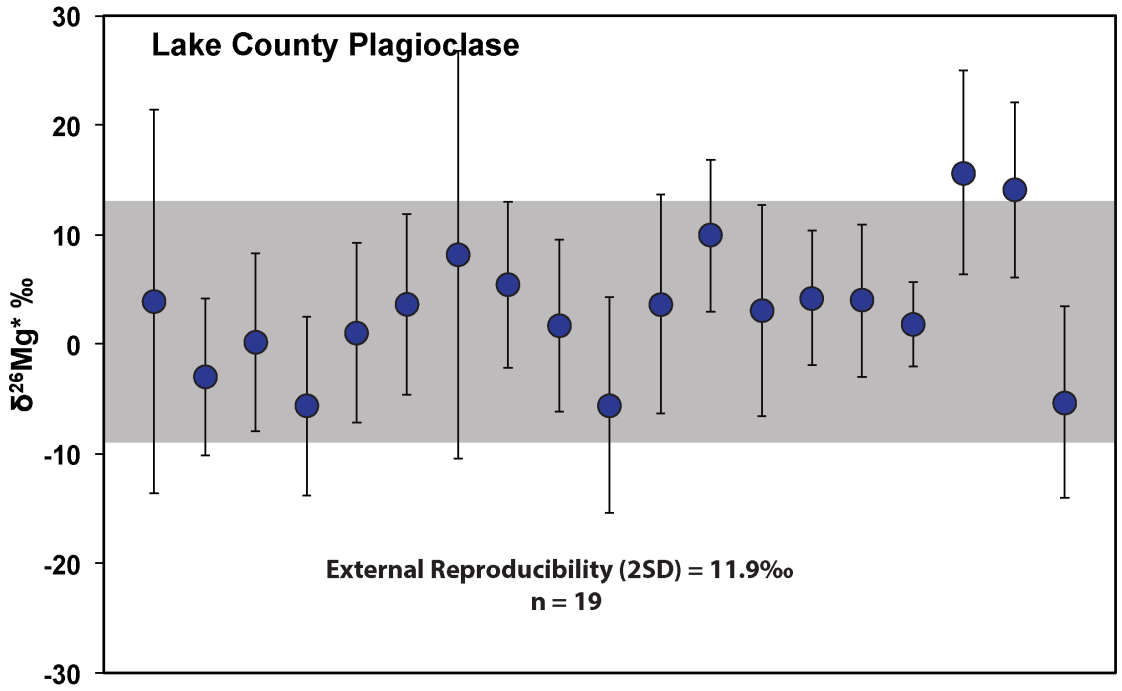

Figure 4.1b. External reproducibility of $\delta^{26}Mg^*$ on Lake Country plagioclase

4.3 Results

4.3.1 Petrography of CAIs and their WL rims. CAI-1 is a coarse-grained inclusion consisting of melilite, spinel, anorthite and pyroxene (Figure 4.2a and 4.2b). The WL rim sequence is more or less continuous and it consists of pyroxene, spinel, and anorthite. Some of the anorthites show hedenbergite needles crystallizing inside anorthites in the WL rims. Some spinels also show evidence for melting, with Fe-rich composition and relict spinel grains in the rims. The outermost pyroxene layer however, is fine-grained and does not show any evidence for melting. CAI-2 is similarly a coarse-grained inclusion that is containing spinel, anorthite, Ti-rich pyroxene, and melilite (Figure 4.3a and 4.3b). This inclusion also contains some Fe-Ni metal. The WL rim sequence consists of anorthite, spinel, pyroxene and some patchy occurrence of nepheline (Figure 4.4). The WL rim only partially surrounds the

CAI, the other part exposes interior anorthite. Some regions in the WL rim of CAI-2 show presence of glass (Figure 4.4), suggesting very quick crystallization after melting.

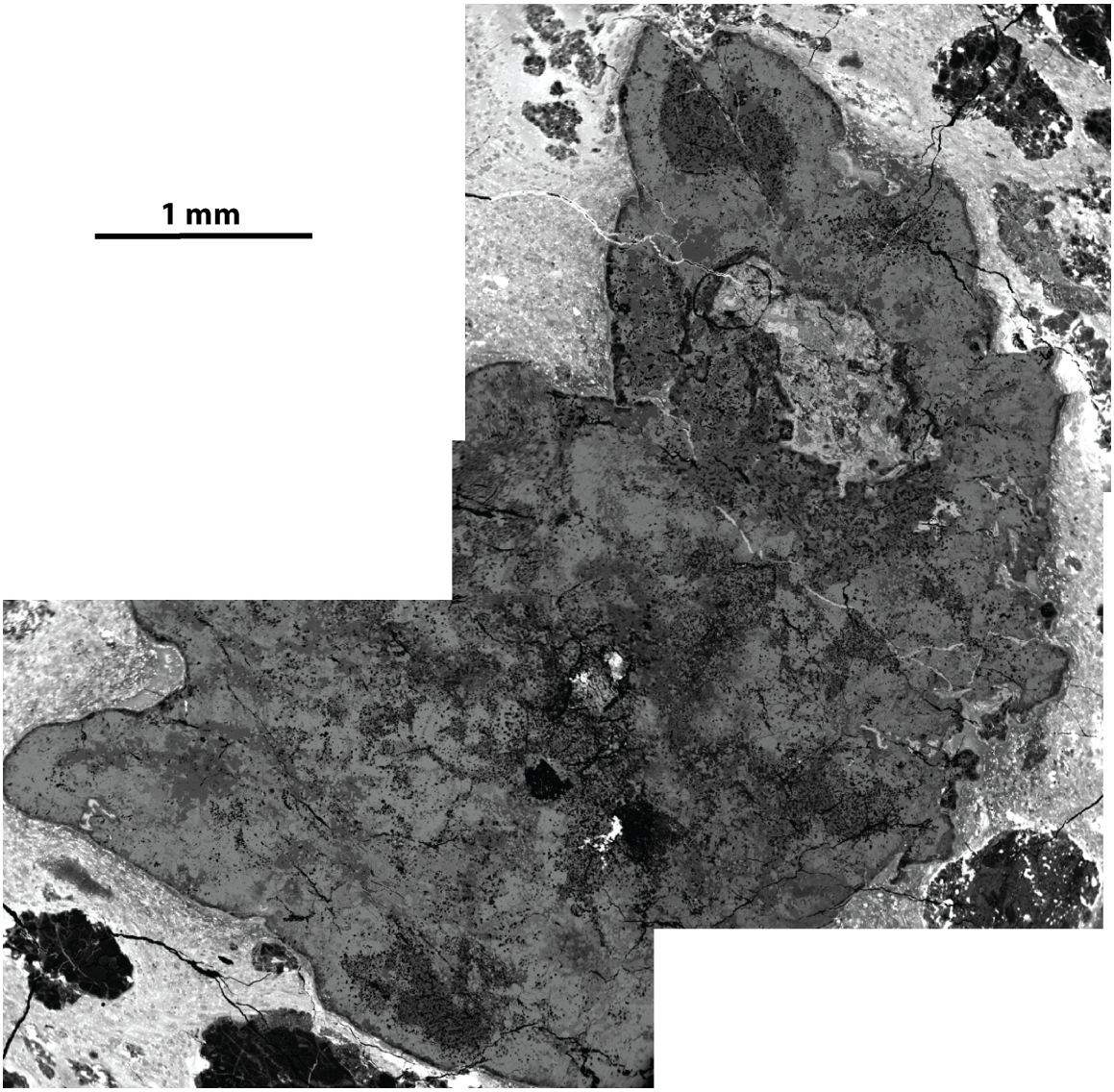

Figure 4.2a. Backscattered electron image of CAI-1

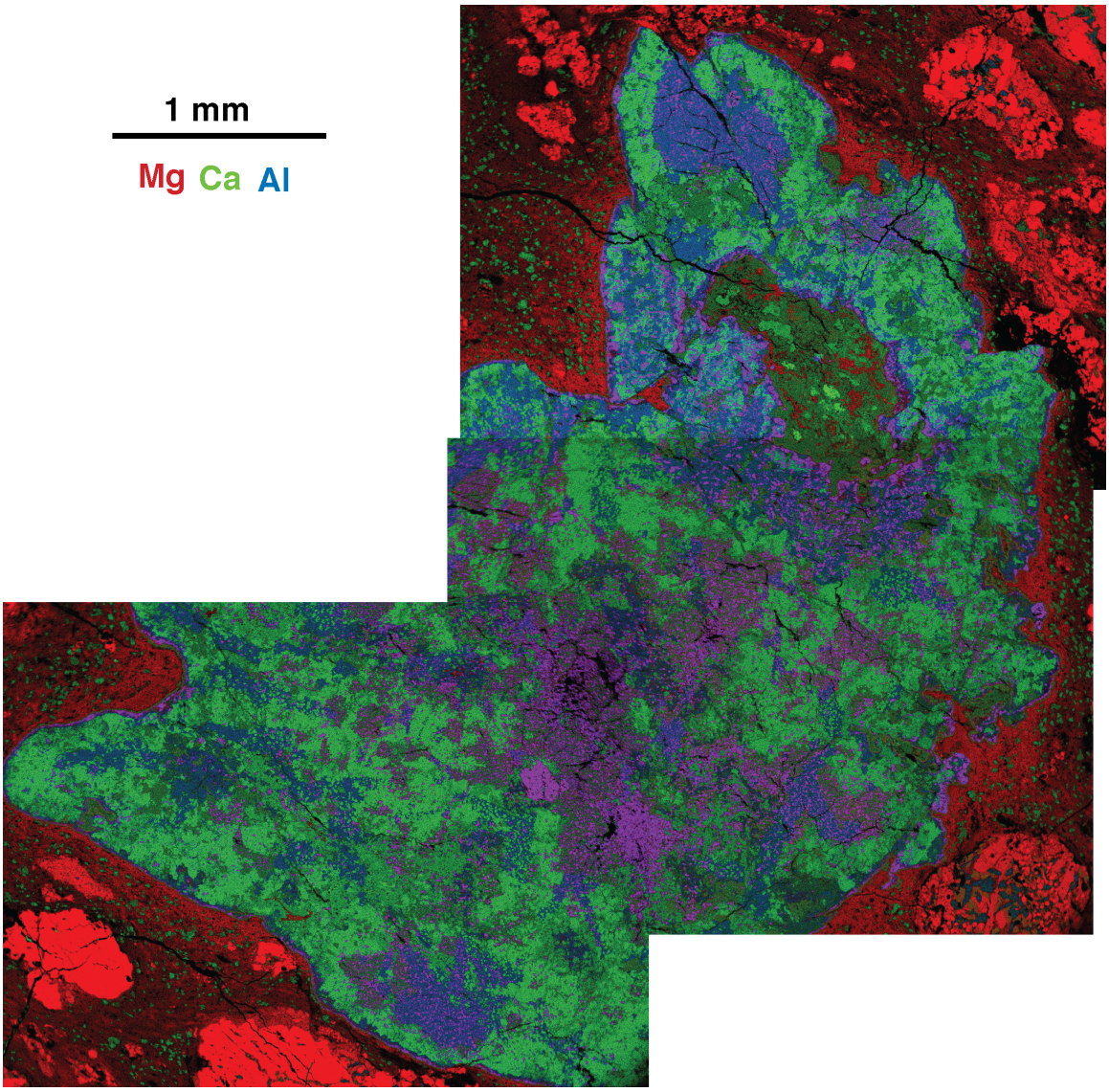

Figure 4.2b. X-ray elemental map of CAI-1

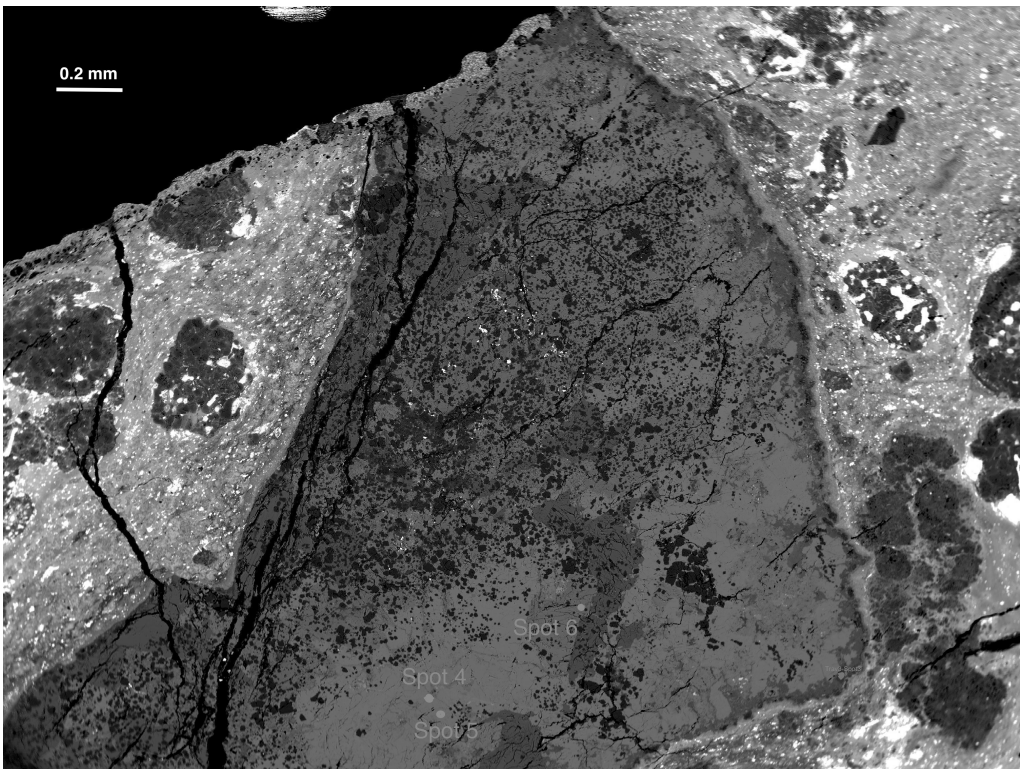

Figure 4.3a. Backscattered electron image of CAI-2

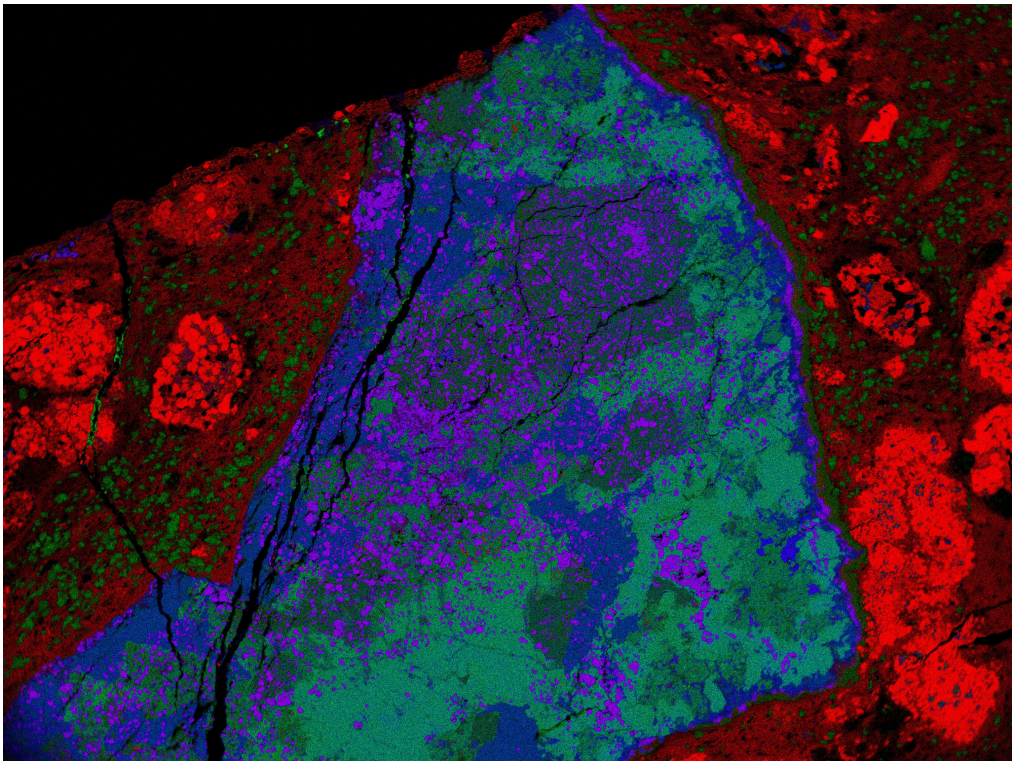

Figure 4.3b. X-ray elemental map of CAI-2

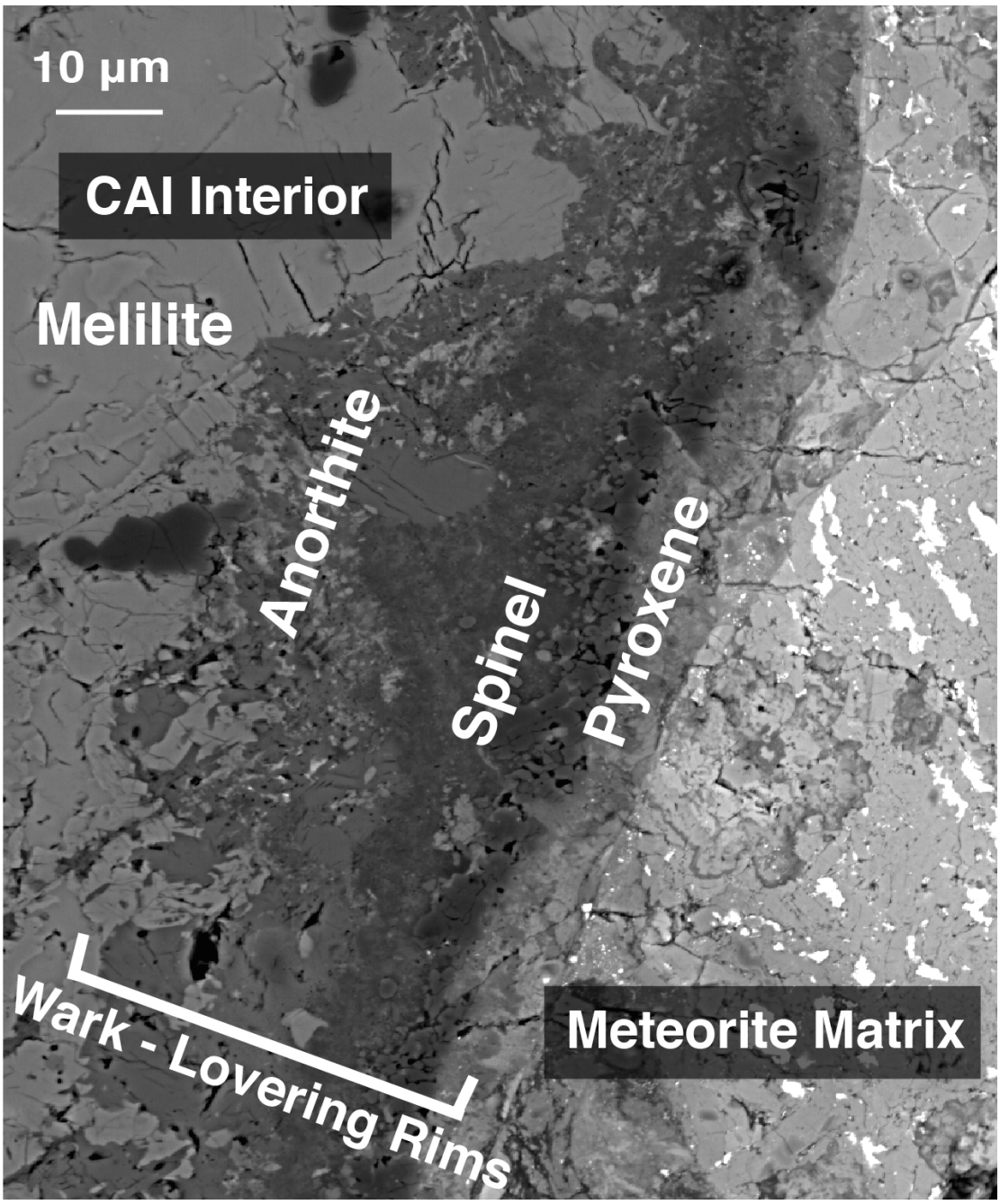

Figure 4.4. Back-Scattered Electron Image (BSE) of a WL rim sequence from CAI-1

4.3.2 Trace element abundances of CAIs and their WL rims.

a. Na abundances: Anorthite occurs as a primary well as a secondary alteration phases in CAIs. A correlated analysis of Al-Mg system and Na abundances was performed on a Type B Vigarano CAI USNM 1623-8 (Macpherson and Davis, 1993). Coarse-grained anorthite and melilite in this inclusion shows elevated Na abundances and no correlation between Al/Mg ratios and $^{26}Mg^*$ abundances. Given the coarse grained nature of anorthite in this inclusion, it was suggested that anorthite was initially formed as a nebular alteration product, which was later melted during a brief melting event, which did not allow all the Na to evaporate (Macpherson and Davis, 1993). We compared the Na abundances from this inclusion with the anorthite analyzed for this work (Figure S3) and they are significantly lower than Na abundances reported for USNM 1623-6 anorthites. Unlike USNM 1623-6, the Al-Mg systematics in CAI-1 and CAI-2 define well-correlated isochrons.

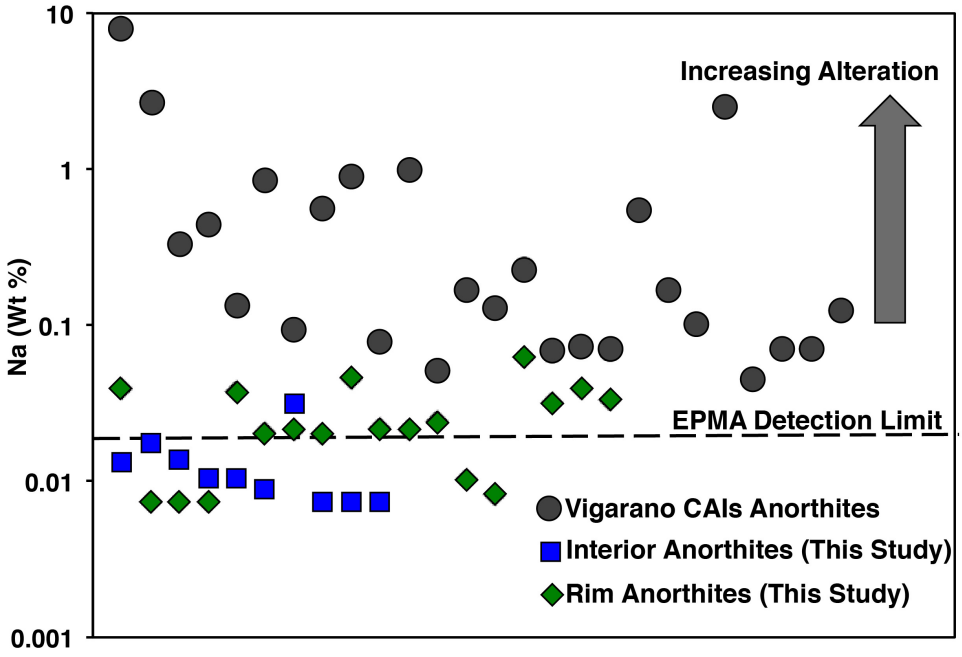

Figure 4.5. Na abundances of CAI interior and WL rim anorthites. Na abundances in anorthites from Vigarano CAIs affected by secondary alteration (with reset Al-Mg isochrons) are plotted for reference (MacPherson and Davis, 1993)

b. Trace elemental abundances: In many CAIs, fine-grained anorthite occurs as an alteration product of melilite. However, alteration products derived from melilite show loss of Sr. Trace elemental abundances of Eu, Ba and Sr were analyzed in two Type B CAI from Allende, TS23 and TS 24 (Davis et al., 1994). Primary anorthites that show canonical initial $^{26}Al/^{27}Al$ ratio do not show constant Eu/Sr ratio but a variable Ba/Sr ratio. However, alteration products derived from melilite show a positive trend that suggests Sr loss in these phases. When compared to interior as well as rim anorthites from CAI-1 and CAI-2, they also show variable Ba/Sr ratio but constant Eu/Sr ratio, suggesting that these interior and rim anorthites are primary and not an alteration product derived from melilite.

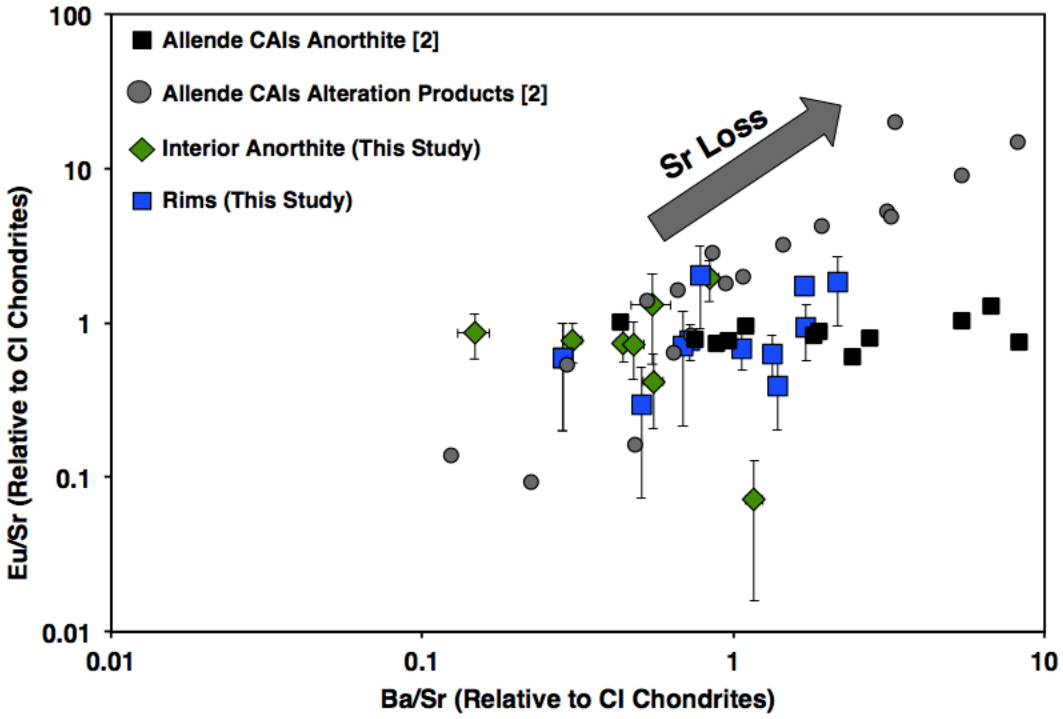

Figure 4.6. Ba/Sr and Eu/Sr ratios of anorthites from WL rims and CAI interiors. For Comparison anorthites from Allende CAIs that are relatively unaltered (showing canonical Al-Mg isochrons) and alteration products that show evidence for Sr loss (Davis et al., 1994)

4.3.3 Oxygen Isotopic Composition of CAIs and their WL rims. Oxygen isotopic analyses of the two inclusions analyzed for this study shows variation in the interior as well as rims (Figure 4.6a and 4.6b). In terms of $\Delta^{17}O$, phases in the two CAIs range from the CAI end-member ($\Delta^{17}O$ = -25‰) up to the terrestrial value ($\Delta^{17}O$ = 0‰). The interior spinels show $\Delta^{17}O$ values of -24 ± 2 ‰ (2SD). The interior pyroxenes also show a restricted range in $\Delta^{17}O$ of -24.2 ± 1.6 ‰ to -20 ± 1 ‰. The interior melilites show $\Delta^{17}O$ values that are close to terrestrial (ranging from -9 ± 2 ‰ to -1 ± 2 ‰). The interior anorthites show a range in $\Delta^{17}O$ of -11 ± 2 ‰ to -1 ± 2 ‰. The WL rim spinel show a restricted range in $\Delta^{17}O$ of -19 ± 2 ‰ to -22 ± 2 ‰. The rim pyroxenes show $\Delta^{17}O$ values ranging from -24 ± 2 ‰ to -8 ± 2 ‰. The rim anorthites show $\Delta^{17}O$ values in the range of -4 ± 2 ‰ to 0 ± 2 ‰.

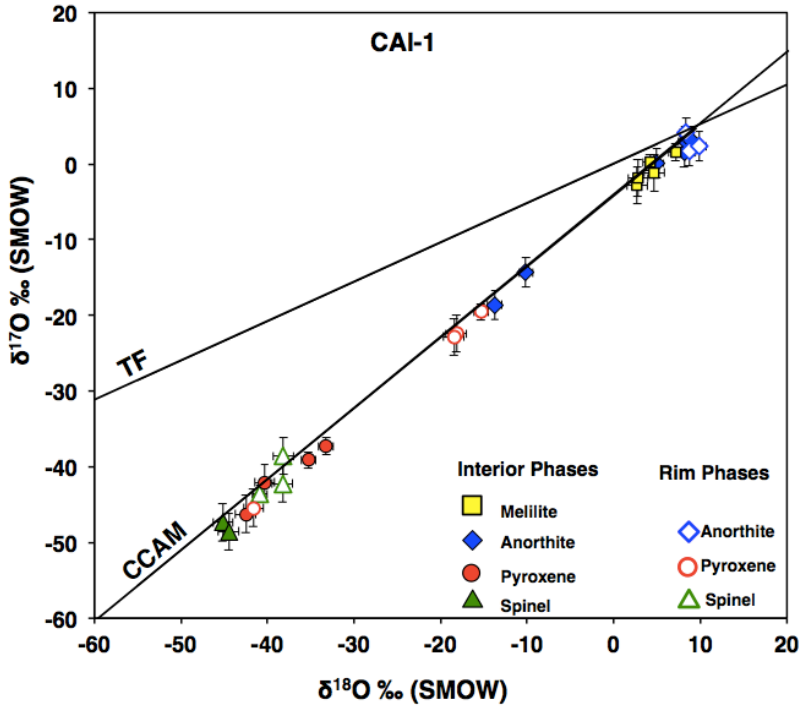

Figure 4.7a. Oxygen isotopic composition of mineral phases in CAI-1 and its WL rim

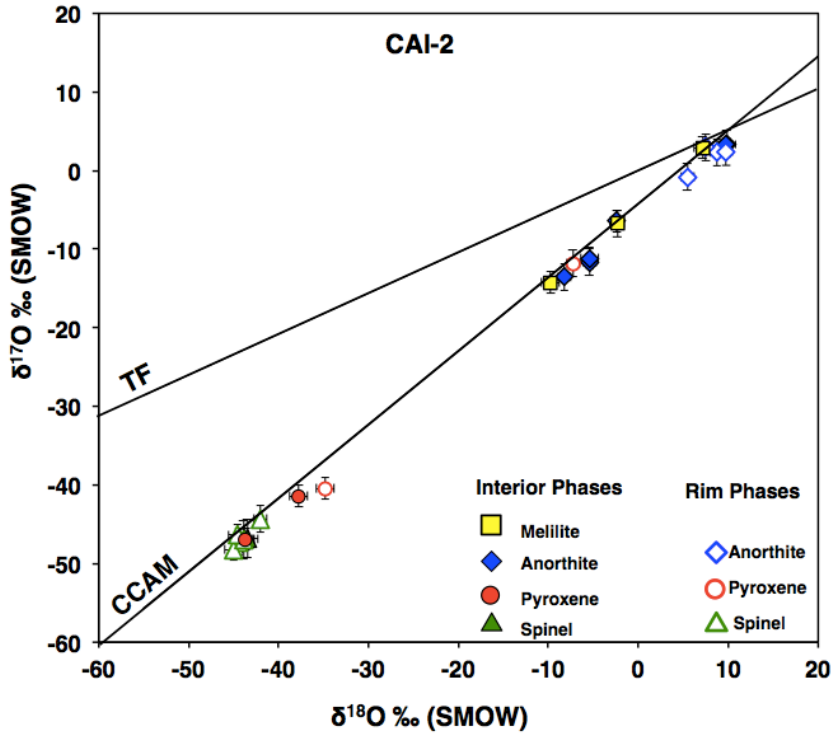

Figure 4.7b. Oxygen isotopic composition of mineral phases in CAI-2 and its WL rims.

4.3.4 Al-Mg Systematics of CAIs and their WL Rims. The interior of the CAI-1 shows evidence for a $^{26}Al/^{27}Al$ ratio of (5.2 ± 0.6) × 10^{-5}, with initial $(\delta^{26}Mg^*)_0$ of 1.7 ± 4.7‰ (MSWD = 2.9). In the WL rim for CAI-1, the $^{26}Al/^{27}Al$ ratio was inferred to be (6.2 ± 3.2) × 10^{-6}, with initial $(\delta^{26}Mg^*)_0$ of 3.4 ± 2.7‰ (MSWD = 0.5). The relative time between formation of CAI-1 interior and its WL rim is $2.2^{+0.7}_{-0.4}$ Ma. The interior of the CAI-2 shows evidence for a $^{26}Al/^{27}Al$ ratio of (5.2 ± 0.4) × 10^{-5}, with $(\delta^{26}Mg^*)_0$ of 5.8 ± 3.9‰ (MSWD = 2.1). In the WL rim for CAI-2, the $^{26}Al/^{27}Al$ ratio was inferred to be (4.5 ± 3.4) × 10^{-6}, with $(\delta^{26}Mg^*)_0$ of 4.4 ± 3.1‰ (MSWD = 1.0). The relative time between formation of CAI-2 interior and its WL rim is $2.5^{+1.5}_{-0.6}$ Ma. The Al-Mg isochrons for both the CAIs and their rims are shown in Figure 5a and 5b.

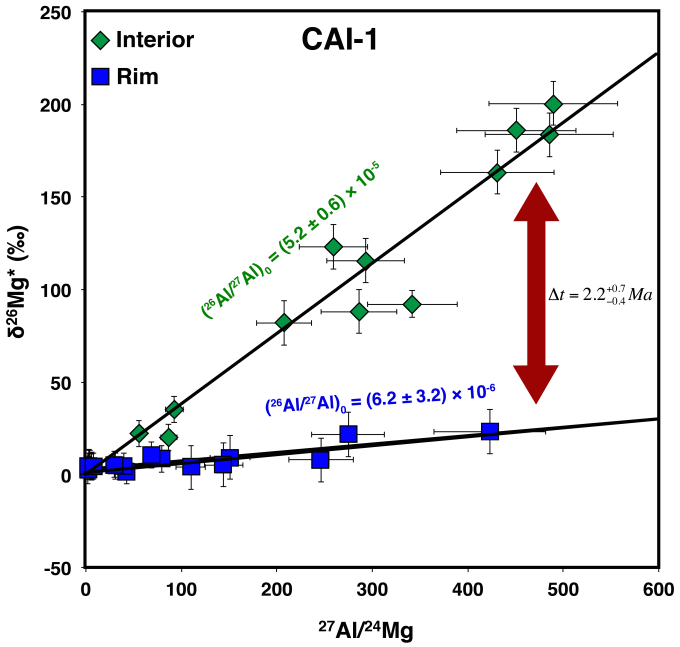

Figure 4.8a. Al-Mg relative isochrons CAI-1 interior and WL rims.

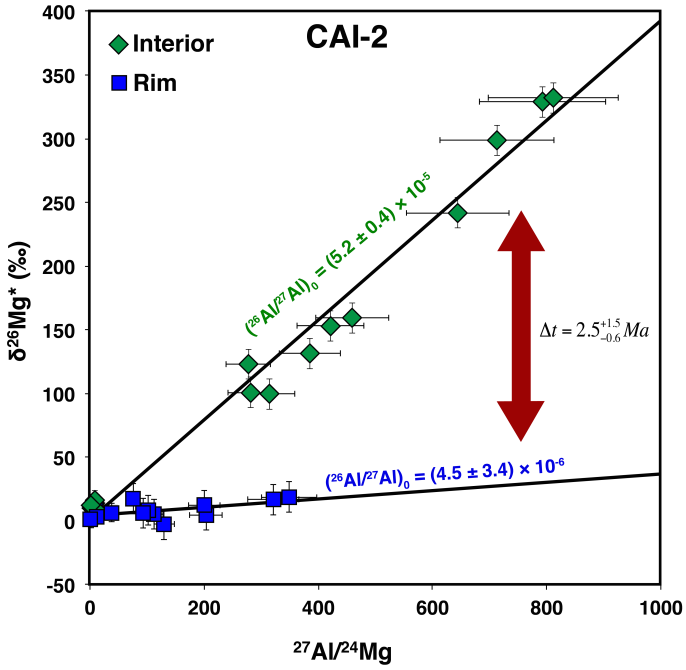

Figure 4.8b. Al-Mg relative isochrons CAI-2 interior and WL rims.

4.4 Discussion

4.4.1 Formation history of WL rim sequence. The WL rim sequences observed in these two inclusions, coarse-grained anorthite and euhedral spinel suggesting formation of these layers crystallized from a melt, whereas the outermost pyroxene layer is finer-grained suggesting a likely condensation origin. Classically defined WL rims have at least spinel, melilite (and/or its alteration products) and pyroxene. Other rim sequences observed around CAIs include spinel/diopside, spinel/anorthite or melilite/diopside layers (Wark and Boynton, 2001). Wark and Boynton, 2001 (Wark and Boynton, 2001) argued that unless their formation mechanisms are the same, these rims should not be considered as WL rims. The rims studied here show a strong textural evidence of crystallization from a melt, hence indicating a transient heating mechanism responsible for their formation. Although the sequence of minerals in these rims is not classical, they still show concentric mono- to bi- mineralic layers of refractory mineral assemblages that are primary. Therefore we consider these rims as a WL rim sequence.

Oxygen isotopic composition of various chondritic components provides information about different nebular environments where objects like CAIs and chondrules formed and underwent secondary processing, like thermal metamorphism and aqueous alteration (Clayton, 1993). Particularly in CAIs, O isotopes record evidence for varying nebular environments. The Solar O isotopic composition inferred from the Solar wind samples by the genesis mission suggests Solar $\delta^{17}O$ and $\delta^{18}O$ ~ -60‰ (McKeegan et al., 2011). Compared to the rest of the Solar System material, CAIs, AOAs (Amoeboid Olivine Aggregates) and their accretionary rims show ^{16}O-rich composition, with $\delta^{17}O$ and $\delta^{18}O$ values as negative as ~-40‰ (E.g. (Clayton et al., 1973; McKeegan et al., 1998; Krot et al., 2002). Mineral phases in some igneous CAIs show variation in their $\delta^{17}O$ and $\delta^{18}O$ values varying from Solar to terrestrial

composition e.g., (Aléon, 2016), defining a mass independent mixing line with slope ~1 (CCAM: Carbonaceous Chondrites Anhydrous minerals). Most CAIs show ^{16}O-rich solar like isotopic composition, whereas chondrules show intermediate δ^{17}O and δ^{18}O values ranging from -10‰ to 5‰ (Clayton, 1993; Kita et al., 2010; Tenner et al., 2013). O isotopic composition of chondrules shows variation in different chondrite groups, however their O isotope values are intermediate between CAIs and secondary alteration products.

Most oxygen isotopic analyses of WL rims show ^{16}O enrichment (similar to the CAI parent reservoir) as well as the presence of a ^{16}O poor component. Both these components are present within the same rim sequence (Hirai et al., 2002; Cosarinsky et al., 2005; Yoshitake et al., 2005; Ito and Messenger, 2008; Simon et al., 2011; Simon et al., 2016b). These variations in oxygen isotopes have been explained by flash heating and subsequent re-equilibration with nebular gas (Hirai et al., 2002; Ito and Messenger, 2008). Alternatively, it has been suggested that rim sequences are a product of condensation processes and CAIs cycled between ^{16}O rich and ^{16}O poor nebular reservoirs, trapping different isotopic signatures in their rims (Ito and Messenger, 2008; Simon et al., 2011; Simon et al., 2016a). Yet another hypothesis suggests that the rims formed as a product of condensation in a ^{16}O-rich environment and the ^{16}O-poor component was introduced later as a product of alteration and disturbance (Cosarinsky et al., 2005; Yoshitake et al., 2005).

The O isotopes in anorthites in the rims and the interiors are partially exchanged whereas both interior and rim spinels and pyroxenes are ^{16}O-rich, suggesting that both interior and rim anorthites may have started with a ^{16}O-rich composition and later exchanged. Although the spatial resolution for O isotopic analyses presented here is not sufficient to determine the O isotope heterogeneity across a single mineral layer, as seen elsewhere, these rims show heterogeneity from one spot to

the other. Interaction of CAI minerals with multiple O isotopic reservoirs in the nebular environment as they crystallize, can explain this heterogeneity. Starting with ^{16}O-rich reservoir where spinel formed followed by crystallization of melilite and anorthite ad partial exchange with ^{16}O-poor reservoir. This was followed by the rim anorthite formation in ^{16}O-poor reservoir. Rim spinel layer formed in ^{16}O-rich reservoir, followed by rim pyroxene that shows varying degree of partial exchange with ^{16}O-poor reservoir. Alternatively, secondary alteration on the parent body could also explain the O-isotope variation seen in the CAI and WL rims minerals. Melilite and anorthite have a high O diffusivity, whereas spinels and pyroxenes are more resistant to O diffusion (Ryerson and McKeegan, 1994). However, there is no other evidence of secondary resetting in the anorthite and melilite. Therefore, it is more likely that the remelting of anorthites occurred in ^{16}O-poor gas, where the spinels remained unaltered but anorthites exchanged. The pyroxene layer formed later, which also shows heterogeneity and ^{16}O-rich composition.

There is abundant evidence of secondary alteration in CAIs, especially from CV3 oxidized meteorites like Allende. The two CAIs analyzed here also show evidence for secondary alteration in certain patches. However, relatively pristine areas in the interior of both the CAIs define a canonical Al-Mg isochron. Therefore we conclude that interior and rim anorthites in CAI-1 and CAI-2 are primary igneous in nature. We cannot rule out the possibility of the rim anorthite forming as secondary alteration product, which later underwent a melting event that evaporated all the Na and other volatiles and homogenized Sr abundances. As anorthite is the innermost layer of the WL rim sequence, other layers formed later.

Considering both the oxygen isotopic systematics and elemental abundances in these two CAIs, the WL rims studied here were likely produced by melting in the solar nebula and were not significantly altered on the parent body. More textural

evidence for this melting event is from glass and Fe-rich euhedral spinels that are also seen in the rims.

4.4.2. Al-Mg relative ages of WL rims. Anorthites provide an opportunity to resolve radiogenic ^{26}Mg excesses because of their high Al/Mg ratios (80-400), which helps constraining the slope of the isochron with higher precision. Although coarse-grained anorthite is a primary mineral in CAIs, anorthite also occurs as an alteration product of melilite in many CAIs. However anorthite in the interior and rims of these two CAIs is primary for following reasons, 1) they show a coarse grained texture, (Figure 4.3), which is typical of crystallization from a melt, whereas alteration products are typically fine-grained 2) The interior and rim anorthites form two distinct well-correlated linear arrays defined by multiple individual analyses in Al-Mg system, for each CAI (Figure 4.5a and 4.5b), whereas, altered anorthites typically show a scatter on Al-Mg space. 3) Alteration products in CAIs show elevated abundances of volatile elements such as Na. A correlated study of Al-Mg system and Na abundances of anorthites from a Vigarano CAI, suggests that reset anorthites also show elevated Na abundances (Macpherson and Davis, 1993). Comparing their results with the anorthites from CAIs reported here, there is no evidence for secondary processing of these anorthites (Figure 4.7) 4) Trace elements such as Sr, Ba and Eu behave like tracers of aqueous alteration (Davis et al., 1994). As seen in some anorthites and other alteration products derived from melilite in CAIs, aqueous alteration results in loss of Sr (Davis et al., 1994). Unaltered anorthites from Allende CAIs do not show such evidence for Sr loss, and maintain relatively undisturbed Al-Mg isochrons; neither do the anorthites (from the rims as well as the interiors) reported here (Figure 4.8).

The relative time difference reported here dates two different melting events, one that melted the entire CAI and the second one that formed the WL rims. As anorthites represent the innermost layer of the WL rim sequence (Figure 4.3), the principle of superposition suggests that the intermediate spinel and outermost pyroxene layers must have formed after the anorthite layer. There is a likelihood that the rim anorthite represents an alteration product of the interior melilite that was later melted and crystallized. During such heating event, evidence of any nebular fluids carrying Na or Sr diffusion could have been erased and homogenized. However after melting and crystallization, these anorthites did not experience any significant alteration.

Al-Mg systematics suggests that CV CAIs precursors formed in a short time interval of ≤ 20 ka in the early Solar System (Thrane et al., 2006; Jacobsen et al., 2008), and their melting continued for at least 0.2 Ma (Hsu et al., 2000; MacPherson et al., 2010; MacPherson et al., 2012) and up to 0.7 Ma for some CAIs (MacPherson et al., 2012). However, some of the rim minerals show a near-canonical $^{26}Al/^{27}Al$ ratio (Simon et al., 2005; Kawasaki et al., 2016), suggesting the onset of WL rims formation contemporaneous with CAIs formation. Our results suggest that the rim formation continued for ~2 Ma either in a spatially isolated nebular region continuously or as multiple episodic events (Figure 4.9).

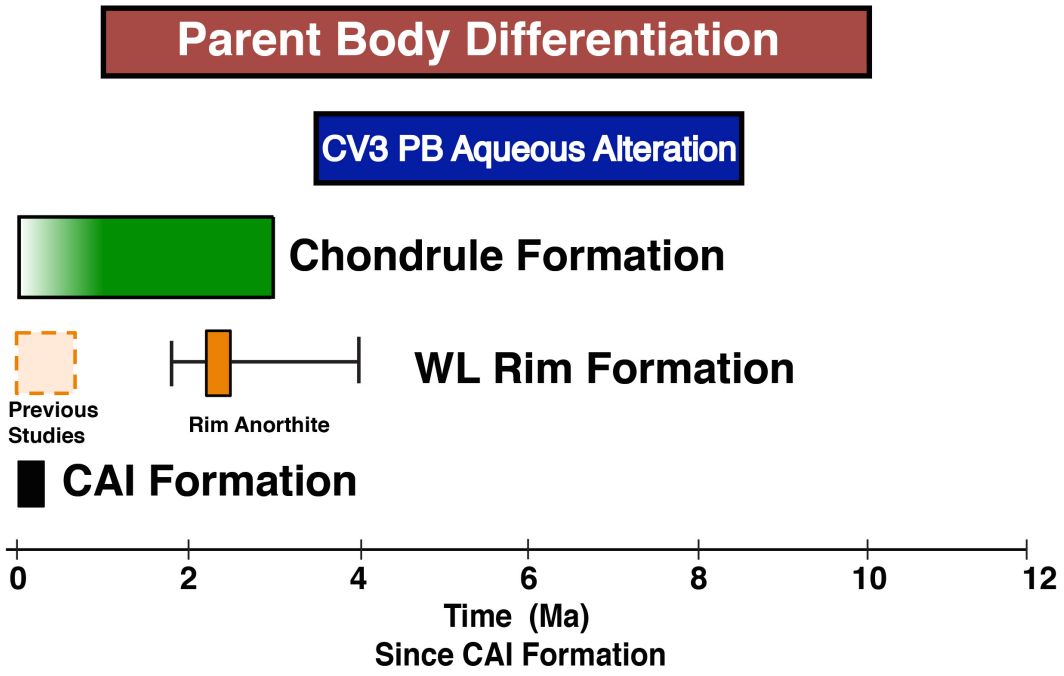

Figure 4.9. Early Solar System chronology

The ~2-3 Ma time difference also coincides with chondrule formation. Chondrule precursors formed as early as ~0.9 Ma after the first solids (Villeneuve et al., 2009), but their meting continued for ~4 Ma, with peak intensities at ~1.5 and ~ 3 Ma (Villeneuve et al., 2009). This suggests that chondrule formation probably occurred as episodic events, where melting of chondrules occurred due to transient heating events such as gravitational instabilities-driven shock or planetismal bow shock events (Desch et al., 2012). Similar heating mechanisms may have caused formation of at least some layers in the WL rim sequence. Chondrules from different chondritic groups show distinct size distribution, O isotopic composition and ^{26}Al-^{26}Mg relative ages, suggesting that chondrules from each chondritic group formed in isolated environments (Kita et al., 2005), however their melting mechanism was

similar. O isotope systematics in at least some CAIs records an evidence for large-scale transport. Therefore, in spite of forming in distinct settings, CAIs and chondrules record similar processes.

If the Al-Mg system is recording the WL rim formation, our results imply that these CAIs may have remained as free-floating objects for ~2-3 Ma before being accreted on their meteoritic parent bodies, suggesting that the CAI-forming region was turbulent and dynamic. Additionally many differentiated meteorites show evidence of early accretion of differentiated parent bodies within first two million years after CAIs (Dauphas and Pourmand, 2011; Kruijer et al., 2014a), carbonaceous and ordinary chondrites were probably the residues of planetary formation, instead of being the primary building blocks of planets.

4.5 Conclusions

Formation of Wark-Lovering (WL) rims around Calcium-Aluminum rich Inclusions (CAIs) in primitive meteorites marks a brief but unique event in the early Solar System history. Each mineral layer in these rims represents an absolute time marker. In some CAIs, these rims show variation in the non-mass dependent oxygen isotopic composition, suggesting that during the rim formation event(s), the CAI was transported to different regions of the solar nebula, with distinct oxygen isotopic signatures. Here we present relative ages of WL rims, using ^{26}Al-^{26}Mg chronometer, suggesting that at least some layers in these rims formed ~2-3 Ma after the host CAI formation. The time difference of ~2-3 Ma coincides with the majority of chondrule formation ages, suggesting that these rims may have formed in flash-heating events similar to those that produced the majority of chondrules in the early Solar System.

Table 4.1

Al-Mg Systematics of CAI-1 and CAI-2 and their WL rims

	$^{27}Al/^{24}Mg$	2 s.d	$\delta^{26}Mg^*$	2 s.d
CAI1-Int1	286	37	88.2	11.9
CAI1-Int2	6	2	4.3	7.4
CAI1-Int3	485	37	183.6	11.9
CAI1-Int4	208	37	81.9	11.9
CAI1-Int5	293	37	115.7	11.9
CAI1-Int6	451	37	185.9	11.9
CAI1-Int7	431	37	163.3	11.9
CAI1-Int8	489	37	200.5	11.9
CAI1-Int9	4	2	6.1	7.4
CAI1-Int10	6	2	4.9	7.4
CAI1-Int11	6	2	5.1	7.4
CAI1-Int12	55	37	22.3	11.9
CAI1-Int13	342	37	92.1	11.9
CAI1-Int14	93	37	35.2	11.9
CAI1-Int15	3	2	6.6	7.4
CAI1-Int16	4	2	6.4	7.4
CAI1-Int17	260	37	123.0	11.9
CAI1-Int18	87	37	20.1	11.9
CAI1-Rim1	43	2	2.3	11.9
CAI1-Rim2	151	37	9.5	11.9
CAI1-Rim3	31	2	4.8	7.4
CAI1-Rim4	144	37	5.5	11.9
CAI1-Rim5	2	0	2.3	2.7
CAI1-Rim6	30	2	5.8	7.4
CAI1-Rim7	79	37	8.6	11.9
CAI1-Rim8	110	37	4.0	11.9
CAI1-Rim9	423	37	23.3	11.9
CAI1-Rim10	3	0	4.5	2.7
CAI1-Rim11	8	2	4.6	2.7
CAI1-Rim12	69	37	10.8	11.9
CAI1-Rim13	40	2	4.5	11.9
CAI1-Rim14	247	37	8.0	11.9
CAI1-Rim15	275	37	21.7	11.9

CAI2-Int1	385	37	131.4	11.9
CAI2-Int2	282	37	100.9	11.9
CAI2-Int3	315	37	99.5	11.9
CAI2-Int4	713	37	298.7	13.6
CAI2-Int5	793	37	328.7	14.1
CAI2-Int6	644	37	241.9	12.1
CAI2-Int7	277	37	123.1	11.9
CAI2-Int8	17	2	7.2	7.4
CAI2-Int9	8	2	6.4	7.4
CAI2-Int10	11	2	4.3	7.4
CAI2-Int11	2	0	2.6	7.4
CAI2-Int12	459	37	159.3	11.9
CAI2-Int13	421	37	153.1	11.9
CAI2-Int14	2	0	12.1	7.4
CAI2-Int15	11	2	13.6	7.4
CAI2-Int16	8	2	16.7	7.4
CAI2-Int17	2	0	10.1	7.4
CAI2-Int18	812	37	332.0	11.6
CAI2-Rim1	112	37	5.3	11.9
CAI2-Rim2	38	2	6.5	7.4
CAI2-Rim3	200	37	12.2	11.9
CAI2-Rim4	130	37	-2.7	11.9
CAI2-Rim5	93	37	6.2	11.9
CAI2-Rim6	2	0	1.8	2.7
CAI2-Rim7	12	2	10.7	7.4
CAI2-Rim8	75	37	17.5	11.9
CAI2-Rim9	348	37	18.8	11.9
CAI2-Rim10	4	0	3.4	7.4
CAI2-Rim11	8	2	3.0	7.4
CAI2-Rim12	102	37	8.5	11.9
CAI2-Rim13	321	37	16.7	11.9
CAI2-Rim14	203	37	4.7	11.9

Table 4.2

Trace element abundance of interior and rim minerals of CAI-1 and CAI-2.

	Ba/Sr	**2 s.d**	**Eu/Sr**	**2 s.d**
CAI1-Int1	0.44	0.02	0.74	0.19
CAI1-Int2	0.84	0.06	1.96	0.58
CAI1-Int3	0.48	0.04	0.72	0.29
CAI1-Rim1	0.73	0.03	0.71	0.20
CAI1-Rim2	0.69	0.05	1.73	0.49
CAI1-Rim3	1.69	0.08	0.64	0.23
CAI1-Rim4	1.33	0.05	0.68	0.20
CAI1-Rim5	1.07	0.04	0.59	0.18
CAI2-Int1	0.30	0.02	0.77	0.22
CAI2-Int2	0.15	0.02	0.86	0.28
CAI2-Rim1	0.55	0.04	0.42	0.21
CAI2-Rim2	1.17	0.07	0.07	0.06
CAI2-Rim3	0.78	0.11	2.04	1.13
CAI2-Rim4	2.16	0.17	1.83	0.87
CAI2-Rim5	1.71	0.10	0.94	0.38
CAI2-Rim6	1.38	0.07	0.39	0.19
CAI2-Rim7	0.51	0.05	0.29	0.22
CAI2-Rim8	0.28	0.04	0.59	0.39
CAI2-Rim9	0.28	0.04	0.59	0.39

Table 4.3

Oxygen isotopic composition of CAI-1 and CAI-2 interior and WL rim minerals.

	$\delta^{18}O$	**2SE**	**$\delta^{17}O$**	**2SE**	**$\Delta^{17}O$**	**2SE**
CAI-1 Area 1 An 1 (Int)	8.10	0.80	1.50	1.93	-2.72	1.96
CAI-1 Area 1 An 2 (Int)	8.30	0.80	2.96	1.93	-1.35	1.96
CAI-1 Area 1 An 3 (Int)	4.94	0.80	0.10	1.93	-2.47	1.96
CAI-1 Area 2 An 4 (Int)	-10.14	0.80	-14.36	1.93	-9.09	1.96
CAI-1 Area 2 An 5 (Int)	-13.74	0.80	-18.60	1.93	-11.46	1.96
CAI-1 Area 2 An 9 (Int)	8.96	0.80	2.96	1.93	-1.70	1.96
CAI-1 Area 2 An 6 (rim)	8.67	0.80	1.67	1.93	-2.84	1.96
CAI-1 Area 3 An 7 (rim)	8.38	0.80	4.11	1.93	-0.25	1.96
CAI-1 Area 5 An 8 (rim)	9.87	0.80	2.34	1.93	-2.79	1.96
CAI-1 Area 2 Spi 1 (rim)	-38.15	1.16	-38.58	2.44	-18.74	2.27
CAI-1 Area 2 spi 2 (rim)	-38.27	1.16	-42.21	2.44	-22.30	2.27
CAI-1 Area 2 spi 5 (rim)	-40.85	0.85	-43.60	1.09	-22.36	1.24

CAI-1 Area 4 spi 3 (int)	-45.17	1.16	-47.36	2.44	-23.87	2.27
CAI-1 Area 4 spi 4 (int)	-44.48	1.16	-48.55	2.44	-25.42	2.27
CAI-1 Area 2 pyr 1 (rim)	-18.19	1.16	-22.40	2.44	-12.94	2.27
CAI-1 Area 2 pyr 2 (rim)	-18.47	1.16	-22.82	2.44	-13.22	2.27
CAI-1 Area 5 pyr 5 (rim)		1.16		2.44		2.27
CAI-1 Area 2 px 9 (rim)	-15.33	0.85	-19.52	1.09	-11.55	1.24
CAI-1 Area 5 pyr 6 (rim)	-41.64	1.16	-45.44	2.44	-23.79	2.27
CAI-1 Area 2 px 7 (int)	-35.30	0.85	-39.10	1.09	-20.75	1.24
CAI-1 Area 2 px 8 (int)	-33.21	0.85	-37.29	1.09	-20.02	1.24
CAI-1 Area 4 pyr 3 (int)	-40.32	1.16	-42.05	2.44	-21.09	2.27
CAI-1 Area 3 pyr 4 (int)	-42.52	1.16	-46.24	2.44	-24.13	2.27
CAI-1 Area 2 mel 1 (int)	4.69	1.16	-1.16	2.44	-3.59	2.27
CAI-1 Area 2 mel 2 (int)	2.71	1.16	-2.87	2.44	-4.28	2.27
CAI-1 Area 4 mel 3 (int)	2.77	1.16	-1.84	2.44	-3.28	2.27
CAI-1 Area 2 mel 4.5 (int)	4.15	0.85	0.20	1.09	-1.96	1.24
CAI-1 Area 3 mel 5 (int)	7.16	0.85	1.53	1.09	-2.19	1.24
CAI-1 Area 3 hd 1 (rim)	7.98	0.85	2.84	1.09	-1.31	1.24
CAI-1 Area5 hd 2 (rim)	7.21	0.85	3.11	1.09	-0.64	1.24
CAI-2 Area 4 An 1 (rim) res 201	8.73	0.74	2.33	1.71	-2.21	1.86
CAI-2 Area 4 An 2 (rim)	5.47	0.74	-0.83	1.71	-3.67	1.86
CAI-2 Area 1 An 3 (rim)	7.49	0.74	2.97	1.71	-0.92	1.86
CAI-2 Area 1 An 4 (rim)	9.75	0.74	2.38	1.71	-2.69	1.86
CAI-2 Area 5 An 6 (int)	-8.23	0.74	-13.53	1.71	-9.25	1.86
CAI-2 Area 5 An 7 (int)	-5.43	0.74	-11.68	1.71	-8.86	1.86
CAI-2 Area 5 An 8 (int)	-2.42	0.74	-6.43	1.71	-5.17	1.86
CAI-2 Area 5 An 9 (int) res=202	-5.41	0.97	-11.15	1.39	-8.33	1.60
CAI-2 Area 5 An 10 (int)	9.83	0.97	3.35	1.39	-1.76	1.60
CAI-2 Area 5 an 4 (int)	9.74	0.74	3.32	1.71	-1.74	1.86
CAI-2 Area 4 sp 1 (rim)	-44.43	0.74	-47.23	1.71	-24.13	1.86
CAI-2 Area 4 spi 2 (rim)	-42.04	0.74	-44.35	1.71	-22.49	1.86
CAI-2 Area 2 spi 5 (rim)	-45.00	0.97	-48.22	1.39	-24.82	1.60
CAI-2 Area 2 spi 6 (rim)	-43.86	0.97	-46.92	1.39	-24.12	1.60
CAI-2 Area 2 spi 7 (rim)	-44.58	0.97	-46.35	1.39	-23.17	1.60
CAI-2 Area 5 spi 3 (int)	-43.90	0.97	-46.97	1.39	-24.15	1.60
CAI-2 Area 2 spi 4 (int)	-43.46	0.97	-46.85	1.39	-24.25	1.60
CAI-2 Area 1 pyr 1 (rim)	-7.27	0.74	-11.83	1.71	-8.04	1.86
CAI-2 Area 2 pyr 4 (rim)	-34.81	0.97	-40.45	1.39	-22.35	1.60
CAI-2 Area 5 pyr 2 (int)	-37.76	0.97	-41.40	1.39	-21.77	1.60
CAI-2 Area 5 pyr 3 (int)	-43.66	0.97	-46.91	1.39	-24.20	1.60

CAI-2 Area 5 mel 2 (int)	7.15	0.97	2.89	1.39	-0.83	1.60
CAI-2 Area 4 mel 1 (int)	-2.34	0.74	-6.72	1.71	-5.50	1.86
CAI-2 Area 2 mel 3 (int)	-9.75	0.97	-14.25	1.39	-9.19	1.60
CAI-2 Area 4 Glass 1 (rim)	10.59	0.74	4.00	1.71	-1.51	1.86
CAI-2 Area 4 glass 2 (rim)	10.27	0.97	4.14	1.39	-1.20	1.60

CHAPTER 5

ZIRCONIUM ISOTOPE SYSTEMATICS OF CALCIUM-ALUMINUM-RICH INCLUSIONS: IMPLICATIONS FOR THE DEGREE OF ISOTOPIC HOMOGENEITY AND THE PRESENCE OF LIVE ^{92}Nb IN THE SOLAR NEBULA

5.1 Introduction

Nucleosynthetic variations record the isotopic fingerprints of various stellar sources that may have contributed material to the early Solar System. Different isotopic systems record these nucleosynthetic variations in presolar grains, Calcium-Aluminum rich Inclusion (CAIs) as well as in bulk meteorites. Presolar grains condense in extra-stellar environments, such as winds from Asymptotic Giant Branch (AGBs) stars or supernovae, and in many cases are the carriers of nucleosynthetic anomalies. However, when did they condense and how long did they survive in the interstellar medium before being incorporated in our molecular cloud, remains to be answered. Nucleosynthetic anomalies in bulk meteorites represent average isotopic composition on planetary scale, identifying different regions in the solar nebula. Bulk meteorites record homogenization of nucleosynthetic anomalies up to a few millions years from CAI formation.

CAIs in primitive meteorites preserve records of the early Solar System processes (MacPherson, 2014). Absolute Pb-Pb ages suggest that CAIs are the oldest solids in the Solar System that formed ~4567-4568 Ma (Amelin et al., 2010; Bouvier et al., 2011; Connelly et al., 2012). ^{26}Al-^{26}Mg relative ages of bulk CAIs suggest that the precursors of CAIs formed in very short time span of ~30,000 years (Jacobsen et al., 2008; Larsen et al., 2011). However, internal ^{26}Al-^{26}Mg isochrons suggest that their thermal processing continued for up to ~0.7 Myrs (MacPherson et al., 2012). Their oldest age suggests that they probably escaped homogenization, and thus they provide the best chance of preserving earliest Solar System reservoir(s). CAIs record

nucleosynthetic anomalies in a number of isotopic systems that are distinct than rest of the early Solar System material (Meyer and Zinner, 2006). Although presolar grains have not been found in CAIs, CAIs record evidence for in situ decay of many short-lived radionuclides like ^{26}Al, ^{41}Ca, ^{53}Mn, ^{182}Hf, and ^{247}Cm (Lee et al., 1976; Birck and Allègre, 1985; Srinivasan et al., 1994; Brennecka et al., 2010), providing a direct evidence for input from external stellar source(s).

Nucleosynthetic anomalies have been identified in CAIs in various isotopic systems such as Ca, Ti, Cr, Ni, and Zr etc. (Birck, 2004). Some of them exhibit homogenously distinct anomalies than the bulk earth (e.g., *r*- process isotopes of Sm and Nd) and rest of the primitive meteoritic material, whereas, some of them show heterogeneous isotopic anomalies (*p*- process isotopes of Sm and Nd) (Andreasen and Sharma, 2006). Correlated isotopic analyses of multiple systems are of particular interest, as they provide strict constraints about common external sources that may have contributed material to the early Solar System. For example, analysis of Ti isotopes in the Solar System material records a correlated heterogeneity in ε^{46}Ti and ε^{50}Ti (Trinquier et al., 2009). As ^{46}Ti and ^{50}Ti have two distinct nucleosynthetic sources, this correlated heterogeneity was attributed to different degrees of thermal processing of homogenous material of well-mixed molecular cloud (Trinquier et al., 2009). Another study encompasses isotopic composition of a variety of elements such as Ti, Cr, Sr, Mo, Ba, Nd, Sm, Gd, Dy, Er, and Yb in the same set of CAIs from Allende (Brennecka et al., 2013; Brennecka et al., 2014a; Mane et al., 2014; Mercer et al., 2015; Shollenberger et al., 2015). Zirconium isotope systematics is of particular interest because Zr is a highly refractory element, which was condensed into the CAIs early in the Solar System history. It has a high diffusion coefficient; therefore it does not alter very easily during the secondary alteration processes.

Slow and rapid neutron capture (*s*- and *r*-) processes are primarily responsible for the production of nuclides beyond Fe. Zirconium isotopic systematics is of particular interest, as Zr has five stable isotopes, four of which (^{90,91,92,94}Zr) are predominantly formed in stellar environments characterized by low neutron density (*s*- process). A small amount of ^{90}Zr is also produced by proton capture (*p*-) process (Travaglio et al., 2011). Although ^{96}Zr has some contribution from proton capture (*p*-) process and *s*-process, up to ~45 % of total ^{96}Zr requires higher neutron density environments (*r*- process), which are typically seen in supernovae (Arlandini et al., 1999). Therefore Zr isotopes provide an opportunity to determine contribution of nuclides formed in different stellar environments.

Additionally, ^{92}Zr can also be produced as a daughter product of the decay of the short-lived radionuclide ^{92}Nb ($t_{1/2}$ = 37 Ma (Holden, 1990)). ^{92}Zr has been previously demonstrated to cause isotopic variation in meteoritic material and therefore ^{92}Nb-^{92}Zr system has potential as a relative chronometer that could be used to date the processes that fractionate Nb and Zr. As both the parent and daughter elements are refractory in nature, this is system is less likely to be disturbed by secondary loss by volatilization. In addition, Zr and Nb are strongly incompatible elements that are not fractionated during melting and magma crystallization. Therefore ^{92}Nb-^{92}Zr system closure records condensation and accretion of planetary materials. The isotopic signatures of in situ decay of ^{92}Nb, as a correlated excess in ^{92}Zr was first observed in an iron meteorite Toluca, with initial $(^{92}Nb/^{93}Nb)_0$ ratio (1.6 ± 0.3) × 10^{-5} (Harper, 1996; Harper Jr, 1996). However, later studies in CAIs from Allende meteorite, rutile grains from iron meteorite Zagora and zircons from a mesosiderite Chaunskij, reported initial $(^{92}Nb/^{93}Nb)_0$ ratio of ~10^{-3} (Münker et al., 2000; Sanloup et al., 2000; Yin et al., 2000). Internal isochrons from an ordinary chondrite Estacado Camel Donga and a eucritic clast from a mesosiderite

Vaca Muerta define a lower Solar System initial ratio of $(^{92}Nb/^{93}Nb)_0 < 3 \times 10^{-5}$ (Schonbachler et al., 2002). Analysis of Allende CAIs does not show correlated excess in ^{92}Zr and therefore defines an initial $(^{92}Nb/^{93}Nb)_0$ ratio $<10^{-4}$ (Schönbächler et al., 2003). Internal isochrons of differentiated meteorites NWA 4590 (angrite), Agoult (eucrite) and Ibitira (ungrouped achondrite) define a Solar System initial $(^{92}Nb/^{93}Nb)_0$ of $(1.7 \pm 0.6) \times 10^{-5}$ (Iizuka et al., 2016). The discrepancy seen in the Solar System initial ratio of $(^{92}Nb/^{93}Nb)_0$ demands further constrains on the Zr isotopic composition of early Solar System material.

We report Zr isotopic composition of 11 CAIs from Allende (CV3 carbonaceous chondrite) and 4 CAIs from other carbonaceous chondrites (CV3 and CK3 carbonaceous chondrites), to understand degree of mixing in CAIs from different carbonaceous chondrite parent bodies. The Allende CAIs reported here have been analyzed for elements like Sr, Mo, Zr, Ba, Nd, Sm, Gd, and Dy, U, and they show evidence for the *r*-process decoupling at mass ~140 (lighter elements like Sr, Mo, Zr, and Ba showing evidence of r-process excess whereas heavier elements like Nd, Sm, Gd, and Dy show r-process deficits) (Brennecka et al., 2013; Brennecka et al., 2014a). For the four non-Allende CAIs, isotopic systematics of Cr, Ti, Mo, Ba, Sr, Sm, Nd, Er and Yb have been previously reported (Shollenberger et al., 2015; Mane et al., 2016; Shollenberger et al., 2016). This cooperative effort in analyzing multiple isotopic systems in the same set of CAIs is crucial for understanding the origin of nucleosynthetic anomalies, identifying the various carrier phases of these anomalies, and the distribution and preservation of these nucleosynthetic anomalies. This sample set includes different textural types such as fine-grained and coarse-grained CAIs, as well as CAIS with different REE patterns, suggesting that they experienced different thermal histories. This paper reports Zr isotopic composition of CAIs from carbonaceous chondrites other than CV3, for the first time. We analyzed 4 CAIs from

different groups of carbonaceous chondrites, one of them showing resolvable excess in $^{92}Zr/^{90}Zr$ ratio, in order to define the initial value for the CAI forming region.

5.2. Sample Description

Eleven CAIs from Allende (164, 165, 166, 167, 168, 170, 171, 172, 173, 174, and 175) were analyzed for their Zr isotopic composition. CAIs 166, 167, and 175 are fine grained inclusions that show Group – II Rare Earth Element (REE) pattern (Brennecka et al., 2010), suggesting formation from a fractionated reservoir (Fahey et al., 1987), where as CAIs 164, 165, 168, 170, 171, 172, 173, and 174 are coarse grained inclusions with a flat REE pattern (Brennecka et al., 2010), that can be easily explained by condensation from a Solar nebula of CI composition. Additionally four CAIs (referred to hereon as Simpson CAIs) were analyzed, each from a different carbonaceous chondrite. Isotopic systematics of Ti, Cr, Sr, Ba, Sm, Nd, Er and Yb of these four CAIs have been reported previously (Shollenberger et al., 2015; Mane et al., 2016; Shollenberger et al., 2016). Marge and Lisa are from two different CV3 carbonaceous chondrites (NWA 6619 and NWA 6991 respectively). Bart and Homer are from two CK3 carbonaceous chondrites (NWA 4964 and NWA 6254 respectively). Bart, Lisa and Marge show a flat Group III REE patter whereas Homer shows a modified Group II REE pattern.

5.3. Methods

We developed a new protocol for the separation and analysis of Zr isotopes from the CAI matrix. In contrast to methods reported earlier, this procedure has following advantages:

1. total Zr recovery >90%.

2. Isotopic analysis using MC ICPMS provides, degree of ionization (≥95%) (Rehkämper et al., 2001), which allows precise analysis of CAI samples with low Zr abundances.

3. The first part of column ion exchange chemistry gives simultaneous separation of Zr and Ti; the Ti clean up chemistry and isotopic data is reported elsewhere (Torrano et al in prep).

5.3.1 Analytical materials and reagents. The Zr separation chemistry was performed in Isotope Cosmochemistry and Geochronology Lab (ICGL) at Arizona State University (ASU). Samples were digested Teflon Savillex beakers that were exclusively used for extra-terrestrial samples, in order to avoid cross-contamination with terrestrial material. Nitric (HNO_3) and hydrochloric (HCl) acids were double distilled using Savillex acid distillation assembly.

Optima grade hydrofluoric (HF) and perchloric ($HClO_4$) acids and Optima grade H_2O_2 (Fisher Chemical) was used during the first step of chromatography to elute Ti. Milli-Q water (resistivity >18 MΩ cm^{-1}) used for acid dilutions and chromatography. The Eichrome DGA resin was cleaned with 6M HCl and Milli-Q water alternatively, three times each, before loading onto the columns. AG1-X8 200-400 mesh anion exchange resin was cleaned repeatedly in a sequence of following reagents; Milli-Q water, 4N HNO_3, Milli-Q water, 6N HCl, Milli-Q water, 1N HNO_3, Milli-Q water, 1N HCl, Milli-Q water (before loading onto the columns). For both the steps, resins were packed in acid-cleaned Bio-Rad Poly-Prep® columns (d = ~5.5 mm, h = 42 mm).

5.3.2 Elemental Abundances. Elemental abundances and Nb/Zr ratios for Allende CAIs were measured using a Thermo X-series quadrupole ICP-MS at the W. M. Keck Laboratory for Environmental Biogeochemistry at ASU. These CAIs were analyzed for their U isotopic composition and the results of this analysis have need

reported elsewhere (Brennecka et al., 2010). These elemental abundances were analyzed after the U isotopic composition; therefore the Nb/Zr ratios measured here may show some fractionation. The elemental abundances and Nb/Zr ratios for Simpson CAIs were measured at Lawrence Livermore National Laboratory.

5.3.3 Ion Exchange Chromatography for Zr Separation. Zr was separated from the rest of the matrix using, a two-step ion exchange chromatography protocol. The first step of this chemistry derived from (Zhang et al., 2011) and described in table 1. Pre-cleaned DGA resin was loaded in the Bio-Rad columns. DGA resin is a low-density resin that tends to float on high molarity acids, such as 12M HNO_3. Therefore the columns were fritted from the top, after loading the resin. These columns and the resin were further cleaned with 3M HNO_3, a mixture of 3M HNO_3 +1 wt% H_2O_2 and MQ water. The resin is then preconditioned with 12M HNO_3 and the samples are loaded. Major matrix elements, like Ca are then eluted with 12M HNO_3, followed by Ti in a mixture of 12M HNO_3 + 1 wt% H_2O_2. Zr (with Hf) was eluted in a mixture of 3M HNO_3 + 0.3 M HF. The 3M HNO_3 and H_2O_2 mixtures were made fresh, and stored for <5 hours before use, whereas all the other acid mixtures could be stored for up to a few months.

Table 5.1

Column Chromatography (Step 1): (Separation of Zr from CAI matrix)

	(ml)	(Acid strengths)
Clean Resin	10	3M HNO_3
	10	3M HNO_3 + 1 wt% H_2O_2
	4	H_2O
Preconditioning	15	12M HNO_3
Load Sample	10	12M HNO_3
Rinse Matrix (Ca)	10	12M HNO_3
Ti	10	12M HNO_3 1 wt% H_2O_2
Fe	10	3M HNO_3
Zr and Hf	20	3M HNO_3 + 0.3 M HF
REEs	20	0.2M HF

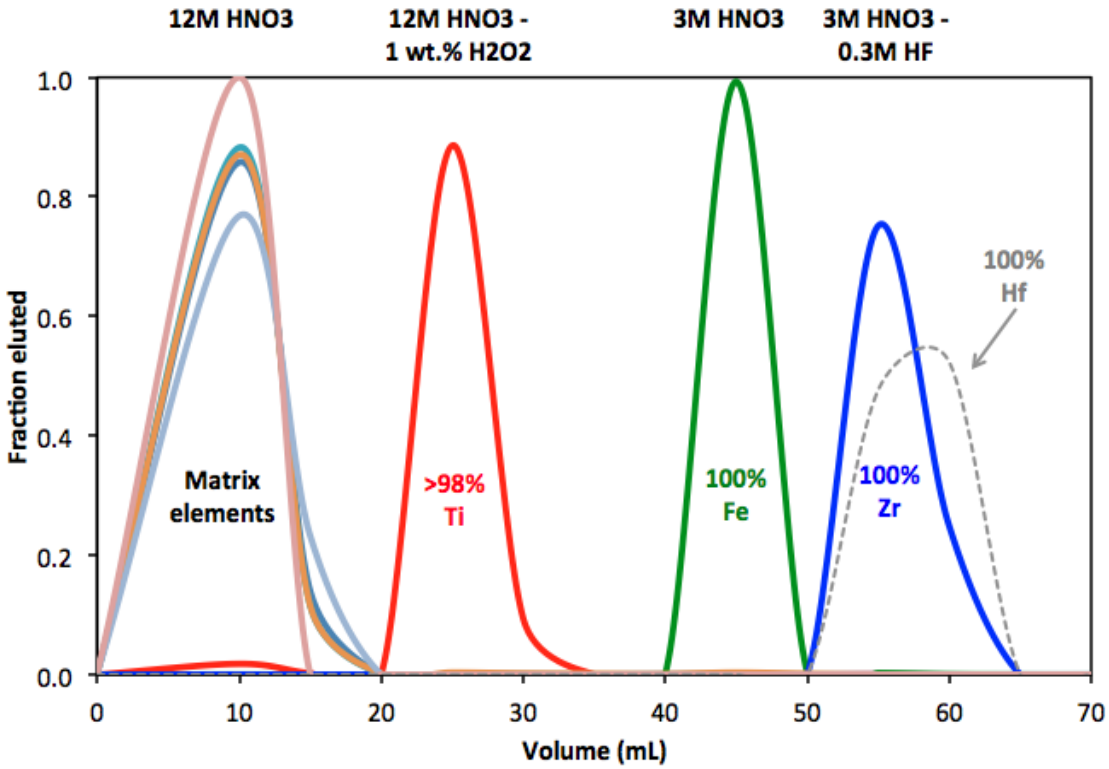

Figure 5.1. Elution curves for Zr separation chemistry using DGA resin

Whole rock samples and some CAIs (especially the ones with low Zr/matrix ratio) show some amount of Fe and other elements, therefore step 2 of this protocol removes any remaining matrix elements from the Zr cut (table 2). After the clean up columns, Zr cuts were dried and re-dissolved in 3% HNO_3 + trace HF (0.014M) for isotope measurements. The procedural blank was <0.05 ng. Multiple sets of whole rock standards were also run before and along with the standards.

Table 5.2

Column Chromatography (Step 2): (Fe clean up column)

	(ml)	
Clean Resin	10	3M HNO_3
	18	MQ H_2O
	12	6N HCl

Preconditioning	5	6N HCl
Load Sample	1	6N HCl
Elute Cr +Zr	4	6N HCl
Elute Zn	8	3N HNO_3

5.3.3 Mass Spectrometry. All Zr isotopic abundances were measured using Thermo Scientific Neptune Multi-Collector Inductively Coupled Plasma Mass Spectrometer (MC-ICPMS) at ICGL, ASU. To maximize the sensitivity of the measurements and reduce the oxide generation we used a 50-µl/minute nebulizer, an ESI Apex-Q sample introduction system with a Jet sample cone and an H skimmer cone. These measurements were conducted in low resolution (m/Δm = ~2000) and using the integration time of 8.4 seconds. All the isotopes were measured on Faraday cups.

Table 5.3

MCICPMS set up for Zr isotopic measurements

Mass Spectrometer Setup	
MC-ICP-MS	Thermo Scientific Neptune
RF Power	~950 W
Pt Guard Electrode	On, grounded
Gas Flow	
Cooling gas	~14 L/min Ar
Auxiliary gas	0
Sample gas	~ 1.2-1.4L/min Ar
Interface cone	Jet (sampler) and H (Skimmer)
Analyzer pressure	~10^9 Torr
Nebulizer (Flow rate)	50 µl/minute
Data Acquisition Parameters	
Acquisition mode	Static analogue detectors
Detection System	Faraday Cups
Resolution Mode	Low Resolution (m/Δm = ~2000)
Single analysis protocol	8.4 s integration per cycle, 25 cycles
Wash out time/Take up time	40 s /60 s

Zr detection sensitivity for ^{90}Zr varied from ~15 to 20 V for 100 ppb Zr solution. Zr isotopic abundances were measured simultaneously, while monitoring $^{179}Hf^{++}$, $^{95}Mo^{+}$ and $^{99}Ru^{+}$ interferences, (For cup configuration see table 4). Prior to isotopic

analysis, the pure Zr solutions were checked for Ti, V, Cr, Fe, and Hf concentrations to make sure that they were below the levels that would the Zr isotopic measurements (See section 5.3.4). Each isotopic analysis consisted of 8.4 seconds integrations of repeated 25 cycles. Each sample analysis was bracketed with NIST SRM 3169 analysis, to correct for instrumental mass bias. The concentration of the samples was matched to that of the bracketing standards within 10%, this is a crucial step because of the unidentified interference on ^{96}Zr (See results, section: 5.3.4). Blank solution 3% HNO_3 + trace HF (0.014M) was analyzed after every 15 analyses for blank correction. Electronic baselines were measured for NIST SRM 3169 standard after every 15 to 20 analyses. Before analyzing the samples, a set of whole rock geologic standards (Allende and BCR-2), pure NIST SRM 3169 standard that was passed through the column chemistry, were also analyzed for their Zr isotopic ratios, to check the efficiency of ion exchange chromatography as well as the accuracy of the mass spectrometric analysis. In order to determine the level at which presence of interfering elements can affect the accuracy of measured Zr isotopic analysis we performed elemental doping tests. Specifically, we measured Zr isotopic composition of NIST SRM 3169 standard, doped with different proportions of a single interfering element (X), with X/Zr ratios varying from 0.0001 to 0.5.

Table 5.4

Faraday collector configurations for Zr isotope measurement using MCICPMS

Cup	L4	L3	L2	L1	C	H1	H2	H3
Species	$^{179}Hf^{++}$	$^{90}Zr^{+}$	$^{91}Zr^{+}$	$^{92}Zr^{+}$	$^{94}Zr^{+}$	$^{95}Mo^{+}$	$^{96}Zr^{+}$	$^{99}Ru^{+}$
Mass	89.4729	89.9047	90.9056	91.9050	93.9063	94.9058	95.9082	98.9059
Amplifiers	10^{12} Ω	10^{11} Ω	10^{11} Ω	10^{11} Ω	10^{11} Ω	10^{11} Ω	10^{11} Ω	10^{12} Ω

5.3.4 Isobaric Interferences. The argide interferences of Ti, Cr, V, and Fe cause major concern for Zr isotopic measurements. Additionally isobaric interferences of Mo and Ru can cause significant variation in Zr isotopic ratios.

Doubly charged species of Hf and W isotopes additionally cause isobaric interferences on ^{90}Zr, ^{91}Zr, and ^{92}Zr. Different interfering species for Zr isotopes have been summarized in table 5.5. Zr isotopic abundances were measured using low mass resolution mode ($m/\Delta m = \sim 2000$), in order to allow maximum transmission. We ran doping tests for Ti, Cr, V, Fe, Hf, Mo and Ru (described in Section 3.3). These tests suggest following limits, below which presence of these interfering elements is permissible and it does not affect the Zr isotopic measurements. For argide interferences, Ti/Zr < 1; Cr/Zr < 1; V/Zr < 10; and Fe/Zr <5 are permissible. However, geo-standards and CAI samples, Ti, Cr, V and Fe abundances were well below these ratios. The ion exchange chromatography technique used for these samples does not allow complete separation of Zr from Hf, but low mass resolution mode still allows complete separation of Hf^{++} and Zr^{+} peaks. Lastly interferences of $^{40}Ar^{40}Ar^{12}C^{+}$, $^{40}Ar^{40}Ar^{14}N^{+}$, $^{40}Ar^{40}Ar^{16}O^{+}$, and $^{80}Kr^{16}O^{+}$ interferences cannot be avoided, and their effects on Zr isotopic composition are evident in analysis of NIST SRM 3169 standard solutions of different concentrations (10 ppb, 20ppb, 40ppb, 80ppb, and 200ppb Zr) that is bracketed with 100ppb standard solution (Figure 2). This mismatch in the concentrations of standard causes a significant shift in Zr isotopic ratios; therefore Zr concentration of each sample was matched within 15% to that of the bracketing standard.

Table 5.5

Isobaric interferences on Zr isotopes

Zr Isotope	Interfering Species	Mass	m/Δm
$^{90}Zr^{+}$	$^{50}Ti^{40}Ar^{+}$	89.90717	37791
	$^{50}Cr^{40}Ar^{+}$	89.90843	24248
	$^{50}V^{50}Ar^{+}$	89.90954	18579
	$^{180}Hf^{++}$	89.97327	1311
$^{91}Zr^{+}$	$^{51}V^{40}Ar^{+}$	90.90634	130988
	$^{182}W^{++}$	90.97410	1327
$^{92}Zr^{+}$	$^{52}Cr^{40}Ar^{+}$	91.90289	42736
	$^{92}Mo^{+}$	91.90681	51924
	$^{40}Ar^{40}Ar^{12}C^{+}$	91.92476	4659
	$^{184}W^{++}$	91.97546	1305
$^{94}Zr^{+}$	$^{54}Cr^{40}Ar^{+}$	93.90126	18587
	$^{54}Fe^{40}Ar^{+}$	93.90199	21730
	$^{94}Mo^{+}$	93.90509	76552
	$^{40}Ar^{40}Ar^{14}N^{+}$	93.92784	4362
$^{96}Zr^{+}$	$^{56}Fe^{40}Ar^{+}$	95.89732	8756
	$^{40}Ar^{40}Ar^{16}O^{+}$	95.91968	8410
	$^{80}Kr^{16}O^{+}$	95.91129	31800
	$^{96}Mo^{+}$	95.90468	26685
	$^{96}Ru^{+}$	95.90760	142044

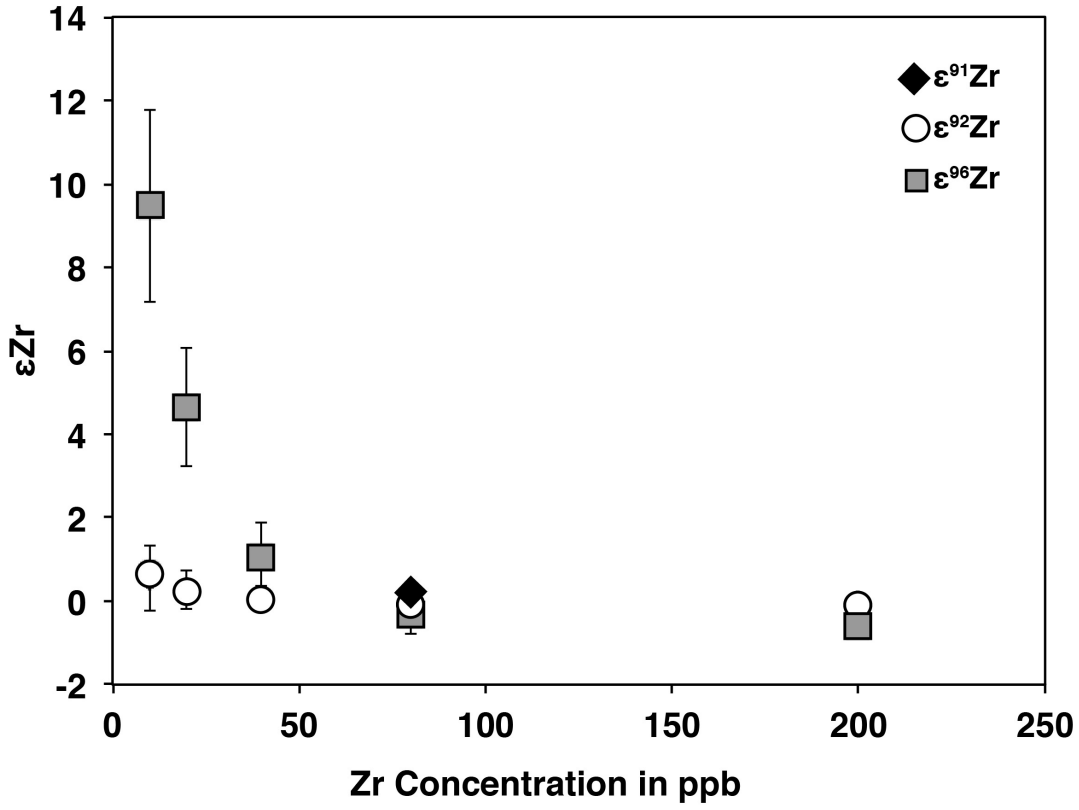

Figure 5.2. Zr isotopic measurements of NIST SRM 3169 at different concentrations show a shift in the Zr isotopic composition, where significant shifts in $\varepsilon^{96}Zr$ ratios are seen, however smaller shifts are seen in $\varepsilon^{91}Zr$ and $\varepsilon^{92}Zr$.

5.3.5 Data Reduction. Blank solution (3% HNO_3 + trace HF (0.014M)) was measured after every 15 analyses, each sample and the bracketing standard were corrected for blanks using these measurements. After blank correction of signal intensities of each isotope, the raw ratios were calculated. The mass bias coefficients (β) were calculated by internally normalizing measured $^{94}Zr/^{90}Zr$ ratios in the sample and bracketing standards to a fixed $^{94}Zr/^{90}Zr = 0.3381$ (Minister and Ricard, 1981) using the exponential mass fractionation law,

$$R_T = R_M (m_1/m_2)^{\beta}$$

where R_M is the measured isotopic ratio, R_T is the true ratio, m_1 and m_2 are the masses of the two isotopes, and β represents the intrumental mass bias.

$$\beta = \ln [(^{94}Zr/^{90}Zr)_{true}/(^{94}Zr/^{90}Zr)_{measured}]/\ln [m_{94Zr}/m_{90Zr}]$$

The interference from $^{92}Mo^+$, $^{94}Mo^+$, $^{96}Mo^+$, and $^{96}Ru^+$ can affect Zr isotopic ratios significantly, therefore $^{95}Mo^+$ and $^{99}Ru^+$ (when applicable) abundances were measured simultaneously and Zr isotopic ratios were corrected for the Mo and Ru interferences. However, the ratios measured in samples of $^{95}Mo/^{90}Zr < 0.001$ and $^{99}Ru/^{90}Zr < 5 \pm 10^{-6}$. After mass bias correction and interference correction the isotopic ratios are expressed in epsilon (ε) units,

$$\varepsilon = (R_m/R_{std} - 1) \times 10000$$

Where, R_m is the measured isotopic ratio and R_{std} is the isotopic ratio of the bracketing standard (average of measured one before and after the sample).

5.4. Results

5.4.1 Reproducibility of Standards. The long-term external reproducibility of NIST SRM 3169 for 100 ppb solution is $\varepsilon^{91}Zr$, $\varepsilon^{92}Zr$, and $\varepsilon^{96}Zr$ is ±0.14, ±0.14 and ±0.31 respectively. The whole rock standards also showed terrestrial composition; for BCR-2, $\varepsilon^{91}Zr$, $\varepsilon^{92}Zr$, and $\varepsilon^{96}Zr$ values are -0.02 ± 0.14, -0.03 ± 0.14, and -0.02 ± 0.48 respectively and for Allende, $\varepsilon^{91}Zr$, $\varepsilon^{92}Zr$, and $\varepsilon^{96}Zr$ values are -0.05 ± 0.19, -0.09 ± 0.14, and 1.36 ± 0.33 respectively. Both the geo-standards agree with previously reported literature values (Akram et al., 2013).

5.4.2 Zr Isotopic Composition of Allende and Simpson CAIs. Zr isotopic composition of Allende and Simpson CAIs has been reported in table 6. All Allende CAIs show terrestrial $\varepsilon^{91}Zr$ and $\varepsilon^{92}Zr$ values and a homogenous $\varepsilon^{96}Zr$ enrichment of ~2 (table 6, figure 3). Three of the Simpson CAIs, Bart, Lisa and Marge also show

terrestrial ε^{91}Zr and ε^{92}Zr values and an enrichment in ε^{96}Zr of ~2. Homer however shows a terrestrial ε^{91}Zr composition, but resolvable excess in ε^{92}Zr of 0.37 ± 0.14 and enrichment in ε^{96}Zr of 0.99 ± 0.40. Except Homer, all other CAIs show a homogenous enrichment in ε^{96}Zr with an average of 2.05 ± 0.38.

Table 5.6

Zr isotopic composition of Allende and Simpson CAIs

CAIs	ε^{91}Zr	2SD	ε^{92}Zr	2SD	ε^{96}Zr	2SD	# of Analyses	Concentrations
164	0.05	0.13	0.11	0.11	2.15	0.29	3	400 ppb
165	0.04	0.22	-0.03	0.14	2.16	0.32	3	400 ppb
166	0.23	0.14	0.02	0.14	1.93	0.31	2	100 ppb
167	0.08	0.25	0.01	0.25	1.56	0.77	5	100 ppb
167	0.11	0.14	0.05	0.14	2.04	0.31	5	100 ppb
168	0.08	0.19	0.09	0.16	2.17	0.47	3	400 ppb
170	0.09	0.25	0.00	0.27	1.94	0.47	5	100 ppb
170	0.11	0.20	0.05	0.14	2.12	0.31	5	100 ppb
171	0.11	0.23	-0.01	0.25	1.87	0.22	3	400 ppb
171	0.14	0.16	0.01	0.14	2.23	0.31	7	100 ppb
172	0.13	0.11	-0.02	0.13	1.96	0.25	3	400 ppb
173	0.08	0.14	0.01	0.11	1.94	0.32	3	400 ppb
174	-0.01	0.21	0.04	0.15	1.99	0.22	3	400 ppb
175	0.18	0.14	-0.05	0.14	2.10	0.38	3	100 ppb
Bart	0.20	0.22	0.09	0.15	2.37	0.36	5	100 ppb
Lisa	0.12	0.15	0.08	0.14	2.28	0.38	5	100 ppb
Marge	0.11	0.15	0.08	0.14	2.12	0.31	5	100 ppb
Homer	0.01	0.19	0.37	0.14	0.99	0.40	5	100 ppb

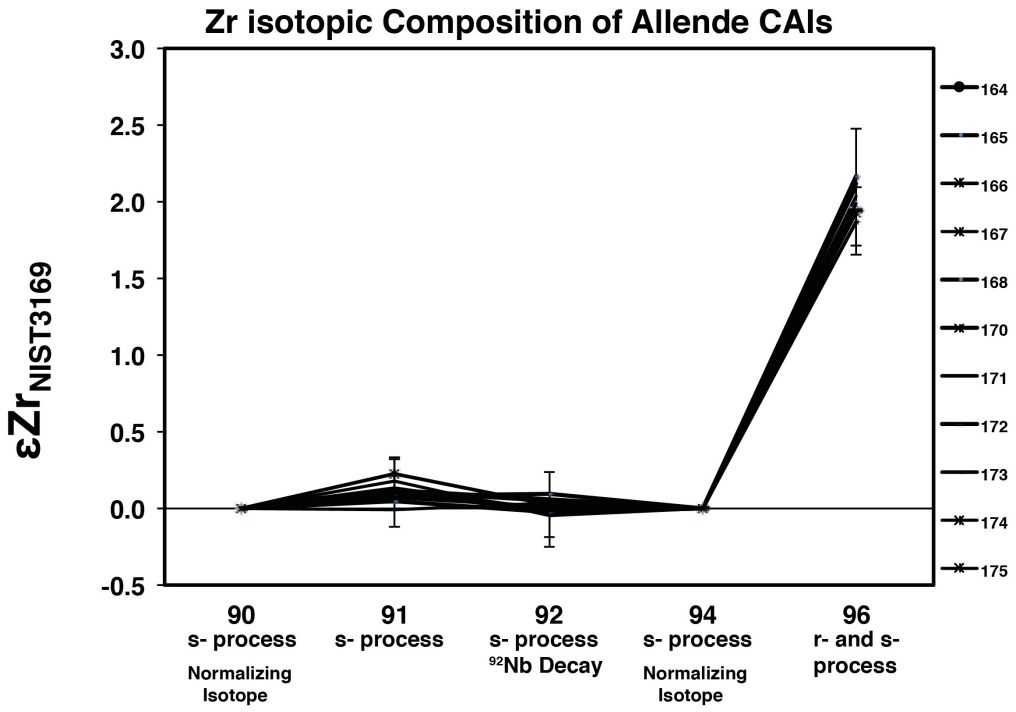

Figure 5.3a. Zr isotopic composition of Allende CAIs

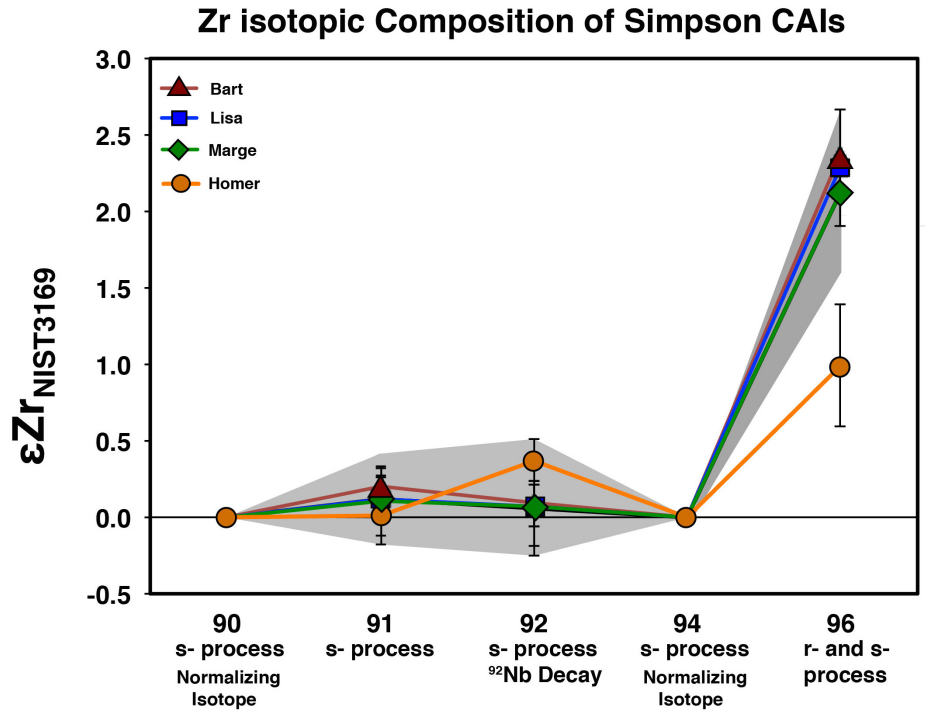

Figure 5.3b. Zr isotopic composition of Simpson CAIs

5.4.5 ^{92}Nb-^{92}Zr Decay System. For Allende CAIs, as elemental abundances were measured after U chemistry, we did not consider these for Nb-Zr systematics due to possible parent-daughter fractionation experienced with previous chemistry. Within the Simpson CAIs, Homer shows resolvable excess in ε^{92}Zr, and therefore the bulk isochron defined by these four CAIs shows an initial $(^{92}Nb/^{93}Nb)_0$ of (1.3 ± 0.7) x 10^{-6} with the MSWD of 0.026 and ^{92}Zr/^{90}Zr intercept of 0.3333776 ± 0.0000003 (figure 5.5).

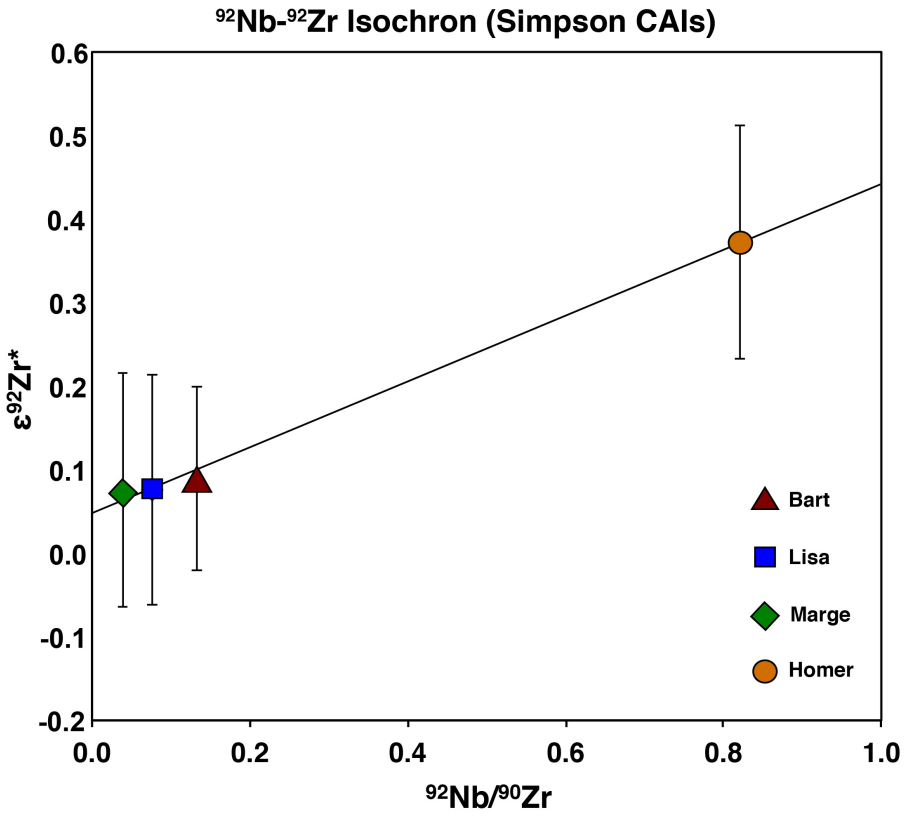

Figure 5.5. ^{92}Nb-^{92}Zr bulk isochron defined by Simpson CAIs.

5.5. Discussion

5.5.1 Origin of Zr isotopic anomalies in the Solar System. Both ^{96}Zr excess and deficits have been observed in different presolar grain components. Mainstream SiC grains from Murchison (CM2) as well as presolar graphite grains show s-process excess, i.e., deficiencies in ^{96}Zr and enrichment in all other isotopes (Nicolussi et al., 1997; Nicolussi et al., 1998; Davis et al., 1999). These grains experienced relatively low neutron density environments and therefore indicate formation in low mass AGB stars (Anders and Zinner, 1993). A small fraction of SiC (1%) as well as presolar graphite grains are characterized by enrichment in ^{96}Zr (Nicolussi et al., 1998; Pellin et al., 2006). The former suggests formation in neutron burst of a supernova (Pellin et al., 2006), whereas the latter suggests formation in either high-density s-process in AGB stars or r-process nucleosynthesis in a core collapse supernova environment (Nicolussi et al., 1998).

Zirconium isotopic measurements of bulk meteorites including carbonaceous, ordinary, and enstatite chondrites, eucrites, mesosiderites, and lunar rocks show a homogenous isotopic composition that is indistinguishable from the terrestrial Zr isotopic composition, suggesting homogeneity in Zr isotopes on planetary scale (Schönbächler et al., 2003). These results suggest that there was large-scale transport and mixing of various presolar components on the planetary scale. In contrast, stepwise leaching experiments of carbonaceous chondrites, Allende (CV), Mucrchison (CM), and Orgueil (CI) reveal large anomalies in Zr isotopic composition (ε^{96}Zr up to ~50‰), with the most distinctive ^{96}Zr enrichment in the acetic acid leachate step, suggesting an unidentified low acid resistant presolar component. These ^{96}Zr enrichments decrease with the increasing acid strengths, and the final leaching step shows a deficit in ^{96}Zr (Schönbächler et al., 2005). These results suggest that even though there was homogeneity in the average Solar System

material, different presolar components with distinct nucleosynthetic anomalies are well preserved in the carbonaceous chondrites.

The Zr isotopic composition the CAIs analyzed here has been shown in Figure 3 and 4. The data for all CAIs are within uncertainty of the measured terrestrial composition for ε^{91}Zr. However, each of the analyzed CAIs, except Homer shows excess in ε^{96}Zr that is identical within the analytical errors. Our CAIs data yield an average value for ε^{96}Zr of 2.05 ± 0.38 (2SD). Our data shows that the CAI-forming region was somewhat homogenous for its Zr isotopic composition. Comparing these studies with the bulk meteorites, we conclude that the CAI-forming region was distinctly homogenous in its Zr isotopic composition, with uniform enrichment in ^{96}Zr, compared to the average Solar System material, which also shows a homogenous Zr isotopic composition. As CAIs are the first formed solids in the solar system (Amelin et al., 2002; Bouvier and Wadhwa, 2010; Connelly et al., 2012), assuming that they represent the isotopic composition at the time of the Solar System formation, either later addition of presolar carrier phases with ε^{96}Zr deficits or some mechanism (discussed in section 5.2) that may have altered the Zr isotopic composition of the average Solar System material on the planetary scale, caused rapid homogenization of the material, before planetary accretion.

5.5.2 Comparison with Nucleosynthetic Anomalies in Other Isotopic Systems. CAIs host a variety of nucleosynthetic anomalies, including Ti and Cr (Trinquier et al., 2009), Mo (Burkhardt et al., 2011), Ru (Chen et al., 2010), and W (Kruijer et al., 2014b). An integrated isotopic analysis of Sr, Mo, Ba, Nd, and Sm suggests isotopic homogeneity in the CAI forming region (Brennecka et al., 2013). Our analysis of Zr isotopic composition of the same set of CAIs, suggests distinct Zr isotopic homogeneity in the CAIs forming region recorded in all CAIs, except one inclusion (Homer). This homogenous distinct *r*-process enrichment in CAI forming

region could either suggest that CAIs formed in an isotopically distinct reservoir that was spatially different than the bulk Solar System, or there was a later injection of freshly synthesized material into the early Solar System after CAI formation (Brennecka et al., 2013). Comparing Zr isotopic composition of these samples with isotopic composition of Sr, Mo, Ba, Sm, Nd, Gd, and Dy, there is a distinct enrichment in r-process isotopes for Sr, Zr, Mo, and Ba whereas, there is a distinct depletion in r-process isotopes of Nd, Sm, Gd, and Dy, with a decoupling at mass ~140 (Figure 5.6).

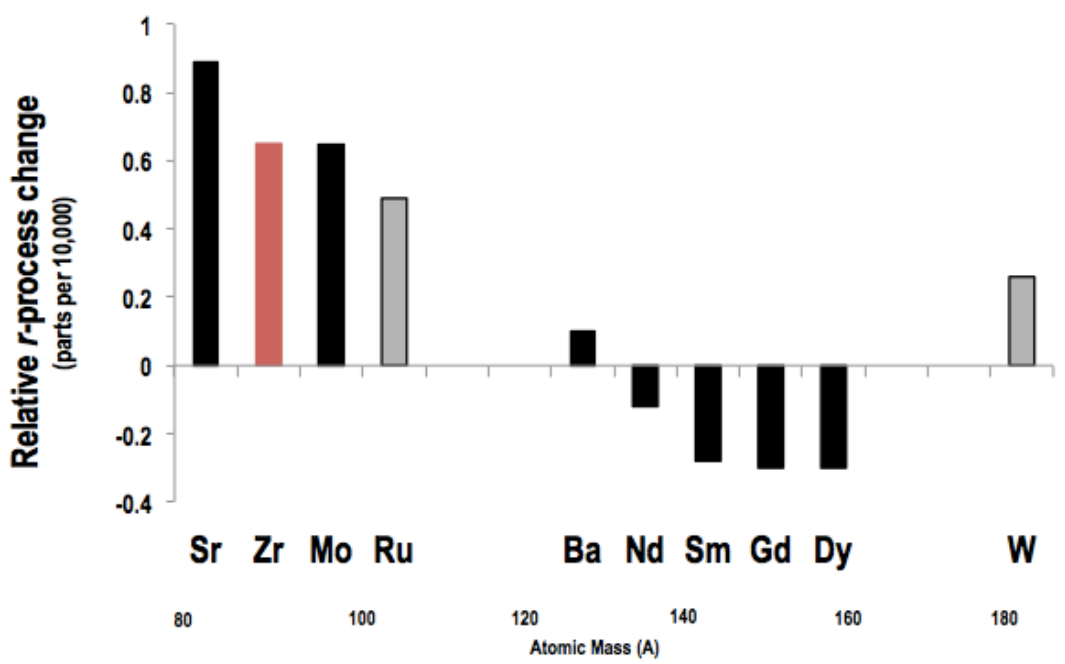

Figure 5.6. Relative *r*- process variations seen in in different elemental systems rom the same set of Allende and Simpson CAIs are shown as black bars. The grey bars show literature data from different sample sets [Chen et al. 2010; Burkhardt et al., 2012]. The red Zr bar is defined by the data presented here. Figure is adapted from [Brennecka at al., 2013].

5.5.3 Implications for the degree of isotopic heterogeneity in the early Solar System. Lesser anomalies in Homer, could suggest three possibilities;

1. Sample Contamination: Simpson CAIs show lesser nucleosynthetic anomalies in other isotopic systems such as Sr and Ba (Shollenberger et al., 2015), which was explained by the disturbance of these mobile elements by later alteration of the CAI or contamination of the CAI by the meteoritic matrix sample processing. However, as Zr is highly refractory element, it is present in the CAIs in much higher abundance than the matrix. Zr is also immobile element and therefore is less easily affected by secondary processes. Homer is the only CAI that shows excess in $\varepsilon^{92}Zr$, which would be diluted if the Zr isotopic systematics were compromised. Therefore it is less likely that the lesser enrichment in Homer is due to disturbances by secondary alteration processes.
2. Initial Zr isotopic heterogeneity in the CAI-forming region: Isotopic heterogeneities in the CAI forming region would suggest that the molecular cloud was not completely homogenized. Heterogeneity in ^{96}Zr was reported for the CAI-forming region (Schönbächler et al., 2003; Akram et al., 2013). Out of 15 CAI samples discussed here, only one shows lesser enrichment in $\varepsilon^{96}Zr$, nevertheless excess in the r-process dominated isotope. Homer also shows highly fractionated REE pattern (Schollenberger et al., in prep), suggesting it is an unusual CAI, recording complex thermal history. Therefore it is possible that Homer records unusual anomalies, not representative of the CAI-forming region.
3. Late formation of Homer relative to other CAIs: Given its fractionated REE patterns, it is likely that Homer has seen more complex thermal history and may have formed later than rest of the CAIs. As indicated by ^{26}Al-^{26}Mg short-

lived relative radio-chronometer, most CAI precursors formed within the first 20,000 to 30,000 years (Jacobsen et al., 2008; Larsen et al., 2011), their internal isochrons suggest that they did see a prolonged thermal history (Hsu et al., 2000; MacPherson et al., 2012). Homer could be such a CAI that may have formed later, recording late input of incompletely homogenized s-process material, that was later injected in the Solar System, before terrestrial planet formation (Brennecka et al., 2013). This hypothesis could be tested by relative age dating of Homer and rest of the CAIs.

5.5.4 Implications for the Initial $^{92}Nb/^{93}Nb$ ratio for the early Solar System. Homer has higher Nb/Zr ratio and shows excess in $\varepsilon^{92}Zr$. The four Simpson CAIs define a slope of initial $(^{92}Nb/^{93}Nb)_0$ ratio of $(1.31 \pm 0.72) \times 10^{-5}$. Although this slope is defined by the $\varepsilon^{92}Zr$ excess seen only in one CAI, it is consistent with the early Solar System initial $(^{92}Nb/^{93}Nb)_0$ ratio defined by an iron meteorite Toluca, with initial $(^{92}Nb/^{93}Nb)_0$ ratio $(1.6 \pm 0.3) \times 10^{-5}$ (Harper Jr, 1996), an equilibrated ordinary chondrite and a eucrite clast (Schonbachler et al., 2002), and Internal isochrons of differentiated meteorites NWA 4590 (angrite), Agoult (eucrite) and Ibitira (ungrouped achondrite) that define a Solar System initial $(^{92}Nb/^{93}Nb)_0$ of $(1.7 \pm 0.6) \times 10^{-5}$ (Iizuka et al., 2016). However this slope does not agree with the higher initial $(^{92}Nb/^{93}Nb)_0$ ratio of $\sim 10^{-3}$ (Münker et al., 2000; Sanloup et al., 2000), defined by bulk isochrons. As discussed in precious studies, this discrepancy could be because of the heterogeneous distribution in the initial $(^{92}Nb/^{93}Nb)_0$, or variation in Zr isotopic composition or analytical artifacts (Iizuka et al., 2016). However, the initial $(^{92}Nb/^{93}Nb)_0$ calculated by our data agrees with the internal isochrons of differentiated meteorites, which are also verified using a long-lived radiochronology technique like U-Pb dating (Schonbachler et al., 2002; Iizuka et al., 2016). Our data

suggest that live ^{92}Nb was injected into either the molecular cloud or CAI forming region, before formation of most of the CAIs. The initial $(^{92}Nb/^{93}Nb)_{0,}$ is in agreement with the initial $(^{92}Nb/^{93}Nb)_0$ calculated by the internal isochrons of differentiated meteorites, hence it was homogenously distributed into the early Solar System and could be used as a relative chronometer.

5.6. Conclusion

The Zr isotopic composition of 11 Allende CAIs and 4 CAIs from different carbonaceous chondrites is reported here. Our results suggest that the CAI-forming region was mostly homogenous with respect to Zr isotopes and enriched in stellar material derived from a neutron-rich environment. The enrichment in the r-process isotope ^{96}Zr is consistent with a model of systematic *r*-process enrichments and depletions following previous work on the same sample set for the isotopic systems of Sr, Mo, Ba, Nd, Sm, Gd, and Dy (Brennecka et al., 2013; Brennecka et al., 2014a). One inclusion Homer, reported here shows lesser enrichment in ^{96}Zr, suggesting either some degree of isotopic heterogeneity in the CAI forming region or later formation of this inclusion, that may have recorded incomplete mixing of later injected material. Homer also shows excess in ^{92}Zr that correlates with Nb/Zr ratios, recording in situ decay of short-lived ^{92}Nb. The bulk isochron defined by the Simpson CAIs shows the initial $(^{92}Nb/^{93}Nb)_0$ ratio of $(1.31 \pm 0.72) \times 10^{-5}$, which is in agreement with the internal isochrons defined by differentiated meteorites.

CHAPTER 6

Mg AND U ISOTOPIC SYSTEMATICS IN ALLENDE CAIs: IMPLICATIONS FOR THE ORIGIN OF URANIUM ISOTOPIC VARIATIONS IN THE EARLY SOLAR SYSTEM

6.1 Introduction

Determining absolute ages of CAIs using long-lived radiogenic chronometers such as Pb-Pb, and relative ages using short-lived radiogenic chronometers such as ^{26}Al-^{26}Mg, is important for establishing the chronology of early Solar System events and timescales of formation of meteoritic parent bodies. The long-lived Pb-Pb chronometer has been utilized extensively for precise absolute age dating of early Solar System objects (e.g., (Amelin et al., 2002; Bouvier and Wadhwa, 2010; Connelly et al., 2012). In earlier studies, this method assumed a constant ratio of ^{238}U/^{235}U (=137.88). However, recent studies have shown that the U isotopic composition varies in early Solar System materials, particularly in CAIs (Amelin et al., 2009; Brennecka et al., 2010). In Allende CAIs, the U isotopic variation was attributed to the decay of short-lived ^{247}Cm to ^{235}U ($t_{1/2}$ ~15.6 Ma) based on the observed correlation of the ^{238}U/^{235}U ratios with the Th/U or Nd/U ratios (as Nd and Th are anticipated to have similar geochemical behavior to Cm during nebular fractionation processes) (Brennecka et al., 2010).

Other possibilities, such as the presence of nucleosynthetic anomalies or isotopic fractionation (during evaporation/condensation or secondary alteration processes) in the early Solar System are also plausible explanations for the variation in U isotopes in CAIs (Amelin et al., 2009; Brennecka et al., 2010; Connelly et al., 2012). However, because U has only two primordial isotopes, it is difficult to distinguish between these processes. To evaluate whether isotopic fractionation during the thermal processing of CAIs is a primary driver for U isotopic variations in

the CAIs, we analyzed the Mg isotopic composition of 11 CAIs from the Allende CV3 carbonaceous chondrite that were previously measured for U isotopes (Brennecka et al., 2010). If isotopic fractionation due to thermal evaporation or condensation was the primary cause of the U isotope variation in these CAIs, then we expect a correlation in the $^{238}U/^{235}U$ and $^{25}Mg/^{24}Mg$ ratios, thereby providing clues to the origin of U isotopic variation in CAIs.

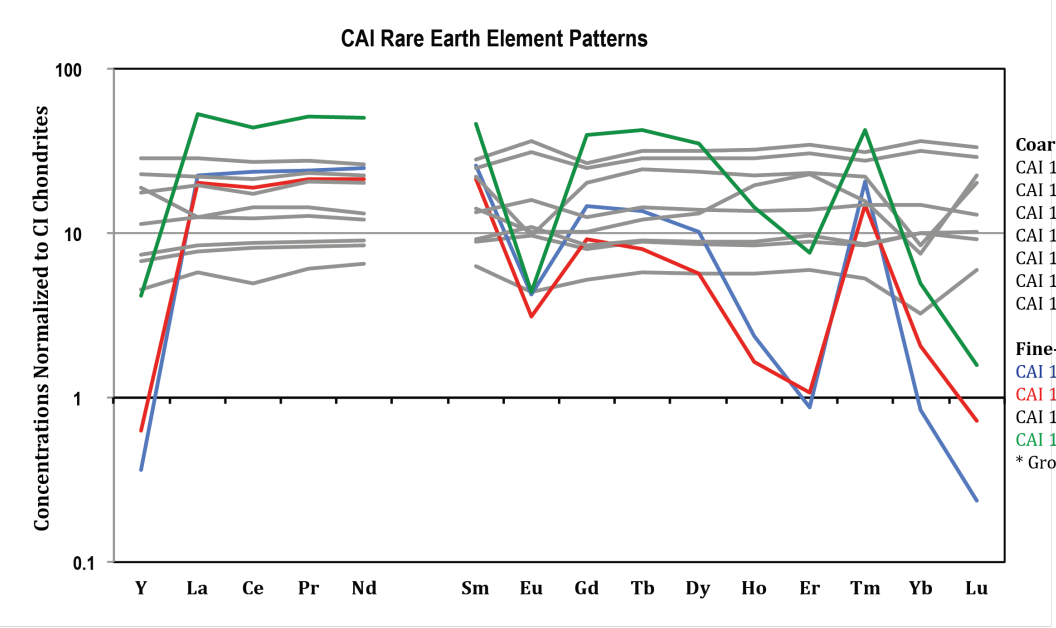

Figure 6.1. Trace Element Abundances of Allende CAIs (Brennecka et al., 2010)

6.2. Sample Description

Eleven CAIs from Allende (164, 165, 166, 167, 168, 170, 171, 172, 173, 174, and 175) were analyzed for their Mg isotopic composition. CAIs 166, 167, and 175 are fine-grained that show Group – II Rare Earth Element (REE) pattern (Brennecka et al., 2010) (Figure 6.1), suggesting formation from a fractionated reservoir (Fahey et al., 1987). CAIs 164, 165, 168, 170, 171, 172, 173, and 174 are coarse grained, with flat REE patterns (Group III) (Brennecka et al., 2010) (Figure 6.1). This Group –

III pattern is consistent with condensation from a Solar nebula of CI composition (Mason and Taylor, 1982).

6.3 Methods

Sample processing and isotopic analysis was performed under clean laboratory conditions in the Isotope Cosmochemistry and Geochronology Laboratory (ICGL) at Arizona State University (ASU). The Mg isotopic compositions of the Allende CAIs were measured using procedures adapted from (Spivak-Birndorf et al., 2009; Bouvier et al., 2011). A ~5% aliquot of each dissolved CAI (equivalent to ~6-16 µg Mg) was passed through a cation exchange column (packed with AG x8 200-400 mesh resin), and Mg was eluted in 1N HNO_3. This column procedure was repeated three times for each sample to assure complete separation of Mg from Al, Ca, and other interfering cations, and ensured recovery of >98% of the Mg for each sample. In order to test if there was any isotopic fractionation during column calibration, a matrix addition test was performed, where an Mg-free matrix of Allende was doped with DSM-3 Mg standard and was processed through the columns. The purified Mg was then analyzed for its isotopic composition. Allende whole rock (WR) and the terrestrial basalt standard BCR-2 were also processed through the same column chemistry procedure and analyzed along with the CAIs to verify the accuracy and precision of our analytical protocols. Prior to Mg isotopic analysis of the purified samples, a small portion of the samples (~1%) were analyzed for interfering cations, such as Ca, Ti, Al, and Fe, using Thermo X7 Series quadrupole ICP MS in the Keck Foundation Laboratory for Environmental biochemistry at ASU. This test was performed to make sure that the abundance of these elements was much below the level that could affect the Mg isotopic composition as shown by the doping tests.

Magnesium isotopic analyses were determined on the Thermo-Finnigan Neptune Multicollector Inductively Coupled Plasma Mass Spectrometer (MC-ICP-MS) in ICGL at ASU. The purified Mg samples, diluted to 250 ppb Mg in 3% HNO_3 were introduced into the mass spectrometer with a flow rate of 100 µl/min using an ESI APEX® dissolvating nebulizer system. The sensitivity achieved at ^{24}Mg was ~22-25V. The mass spectrometer was operated in medium resolution mode ($m/\Delta m = 5000$), in order to separate molecular interferences of $^{12}C^+$, $^{12}C^{14}N^+$ and $^{24}MgH^+$. The instrumental mass bias was corrected using the sample-standard bracketing method, where DSM-3 was used as a bracketing standard. The concentrations of the samples and standards were matched to ~10%. Each measurement cycle consisted of 20 integrations of 8 s each. Each measurement was repeated 3 times. The errors reported here are 2 s.d of the three repeat measurements of every sample. The isotopic ratios are expressed in per mil units (‰). The radiogenic $^{26}Mg^*$ excess was calculated by internally normalizing $^{26}Mg/^{24}Mg$ to $^{25}Mg/^{24}Mg = 0.12663$ (Catanzaro et al., 1966) using the exponential law ($\beta = 0.5128$) (Davis et al., 2015).

Presence of interfering elements can generate matrix effects and significantly affect the accuracy and precision of Mg isotopic measurements. Results of the elemental doping tests suggest that element/Mg > 0.1 affects $\delta^{25}Mg$. Therefore presence of interfering elements below 25 ppb (in 250 ppb Mg solution), does not affect the isotopic ratios. Therefore, Mg samples analyzed here for Mg isotopic composition have typical matrix element/Mg < 0.005, which is well below the proportions that can affect the isotopic measurements.

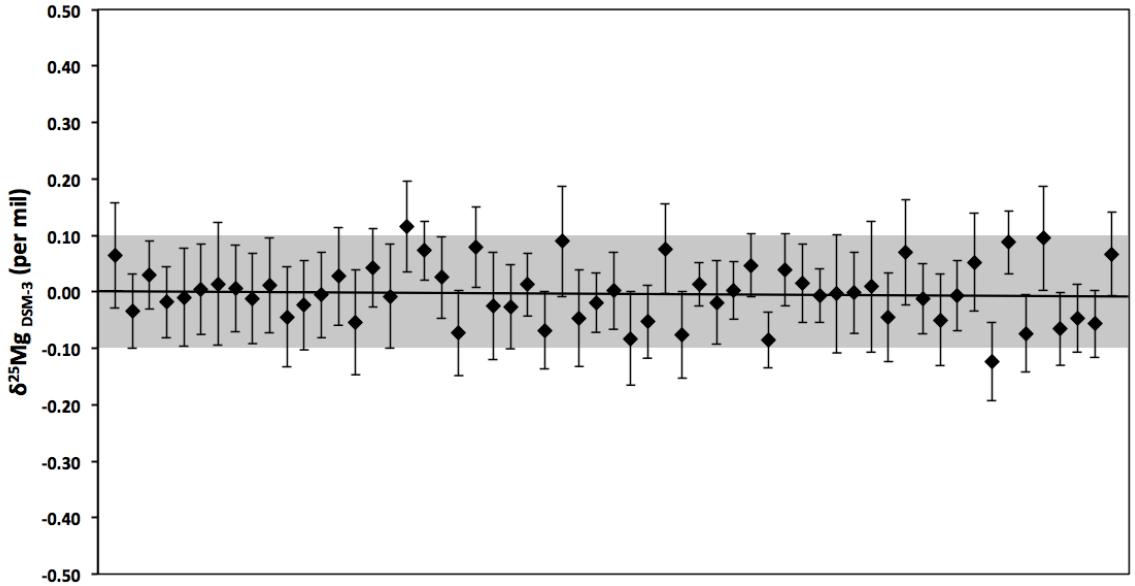

Figure 6.2. External reproducibility of DSM-3 Mg isotopic standard

The long-term reproducibility on DSM-3 internal standard is ±0.11‰ (Figure 6.2)**.** The terrestrial whole rock standard BCR-2 that was processed through the columns along with the CAIs shows δ^{25}Mg = -0.15 ± 0.11 ‰ and the whole rock Allende shows δ^{25}Mg = -0.05 ± 0.06 ‰. Both these values agree with previous studies (Baker et al., 2005; Bizzarro et al., 2005).

6.4 Results

The ^{25}Mg/^{24}Mg ratios (expressed relative to the DSM3 standard in parts per mil, or δ^{25}Mg) of the 11 Allende CAIs, Allende WR, and BCR-2 are reported in Table 6.1. Also presented in Table 1 are the U isotope compositions of each of these samples from (Brennecka et al., 2010) (but corrected for the updated U isotope composition of the SRM950a standard (Richter et al., 2007)). The δ^{25}Mg values for

the Allende CAIs range from +4.80 to -1.28 ‰. Figure 6.3 shows the U isotope compositions of these CAIs versus their δ^{25}Mg values.

Table 6.1

Mg isotopic compositions of the 11 Allende CAIs. U isotope composition are from (Stirling et al., 2007; Brennecka et al., 2010), and are corrected for the updated SRM950a standard value ($^{238}U/^{235}U$ = 137.837(Richter et al., 2010)).

Sample	***δ^{25}Mg***	***2SD***	***δ^{238}U***	***2SD***
Allende	-0.15	0.09	-0.45	0.11
BRC-2	-0.05	0.07	-0.27	0.19
CAI 164	3.32	0.09	-0.30	0.12
CAI 165	4.13	0.06	-0.33	0.11
CAI 166	-0.50	0.05	-3.42	0.28
CAI 167	-0.99	0.05	-1.76	0.30
CAI 168	4.80	0.06	0.04	0.11
CAI 170	3.54	0.06	-0.51	0.28
CAI 171	3.04	0.04	-0.56	0.22
CAI 172	4.02	0.06	-0.31	0.28
CAI 173	-0.54	0.05	-0.61	0.28
CAI 174	4.35	0.07	-0.23	0.11
CAI 175	-1.28	0.09	-1.45	0.22

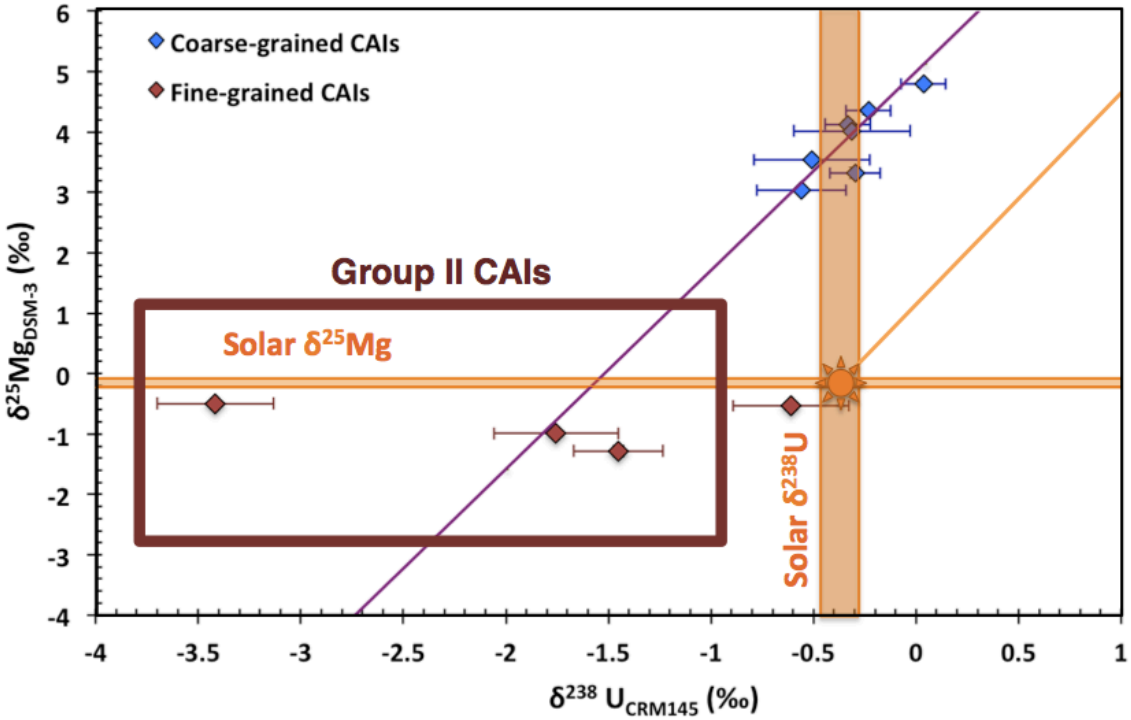

Figure 6.3. δ^{25}Mg and δ^{238}U of the 11 CAIs from Allende. The orange symbols represent fine-grained CAIs whereas the blue symbols represent coarse-grained CAIs. Group II CAIs have been identified in a box. The U isotopic composition is from (Brennecka et al., 2010). The orange rectangles show bulk Solar isotopic composition. The orange line passing through the bulk Solar composition defines behavior of these isotopic systems during Rayleigh fractionation. The purple line is a regression line defined by the coarse grained CAIs.

6.5. Discussion

It has recently been suggested that isotopic fractionation during CAI-forming processes may have contributed to some, if not all, of the U isotope variation in CAIs (Brennecka et al., 2010). As can be seen in Figure 6.3, coarse-grained Allende CAIs, which have undergone melting and thermal processing, show a weak correlation (correlation coefficient $R^2 = 0.73$) between δ^{238}U and δ^{25}Mg. This correlation suggests that isotopic fractionation during thermal processing contributed to the U isotope variation in this subset of samples. It is interesting to note that the

regression line passing through these coarse-grained inclusions (Figure 6.3) also passes through two fine grained inclusions, indicating that the precursors of the coarse grained inclusions may have had different starting Mg isotopic composition than the Bulk Solar System.

On the other hand, fine-grained Allende CAIs (166, 167, 173, and 175), which did not undergo melting, are characterized by relatively light Mg isotopes (i.e., δ^{25}Mg values between -0.5 and -1.5‰). These CAIs show a much larger range of U isotopic compositions than the coarse-grained CAIs, which do not correlate with δ^{25}Mg. Therefore the U isotope variation in these samples may be dominated either by ^{247}Cm decay or by the presence of nucleosynthetic anomalies. Previous work on the same sample set for the isotopic systems of Sr, Mo, Ba, Nd, Sm, Gd, and Dy, are consistent with a CAI source reservoir that was homogenous (at the level of precision of these analyses), yet distinct from the terrestrial composition (Brennecka et al., 2013), thus suggesting that large isotopic variation among "normal" (i.e., non-FUN) CAIs due to nucleosynthetic anomalies in U may be unlikely.

It is notable that three of the fine-grained Allende CAIs (166, 167 and 175) are also classified as group II inclusions (highlighted by a brown box in Figure 6.3). The previously reported correlation of U isotopes with Th/U and Nd/U in Allende CAIs (Brennecka et al., 2010) is dominated by the compositions of these group II inclusions and is additionally suggestive of ^{247}Cm decay as being the dominant cause of the U isotope variation in these fine-grained CAIs. Another possible process that could cause relatively large variations (>1‰) in the U isotope composition without systematically affecting the Mg isotope composition may be secondary alteration under different redox environments. Uranium is a redox-sensitive element, which shows significant isotopic fractionation effects under variable redox conditions in terrestrial systems e.g., (Stirling et al., 2007; Weyer et al., 2008). In contrast, Mg is

not redox sensitive, and different redox conditions would not affect its isotopic composition. Further detailed investigations of redox indicators in fine-grained inclusions along with their U isotope compositions will be required to rigorously evaluate this possibility.

6.5 Conclusions

The mass dependent Mg isotopic composition of 11 CAIs from Allende CV3 carbonaceous chondrite was determined. These CAIs show evidence for mass dependent fractionation in Mg isotopes, possibly caused by thermal processes such as evaporation and condensation in the solar nebula. However, mass dependent Mg isotopic variation does not correlate with the U isotopic variation observed in the same set of CAIs, implying that the mass dependent fractionation due to thermal processes was not the major cause of U isotopic variation in Allende CAIs. Therefore, to explain U isotopic variation in Allende CAIs, other mechanisms such as in situ decay of live ^{247}Cm, nucleosynthetic anomalies in U isotopes and redox controlled isotopic fractionation should be considered.

REFERENCES

Abbas, M. M., Kandadi, H., LeClair, A., Achterberg, R. K., Flasar, F. M., Kunde, V. G., Conrath, B. J., Bjoraker, G., Brasunas, J., Carlson, R., Jennings, D. E., & Segura, M. (2010). D/H ratio of Titan from observations from Cassini composite infrared spectrometer. *The Astrophysical Journal*, *278*, 342-353.

Aléon, J., (2016). Oxygen isotopes in the early protoplanetary disk inferred from pyroxene in a classical type B CAI. *Earth and Planetary Science Letters, 440*, 62-70.

Alexander, C. M. O'D., Bowden, R., Fogel, M. L., Howard, K. T., Herd, C. D. K., & Nittler, L. R., (2012). The provenance of asteroids and their contributions to the volatile inventories of the terrestrial planets. *Science, 337,* 721-723.

Alpher, R. A., Bethe, H., & Gamow, G. (1948). The origin of chemical elements. *Physical Review, 73*, 803-804.

Akram, W., Schönbächler, M., Sprung, P., & Vogel, N. (2013). Zirconium—Hafnium Isotope Evidence from Meteorites for the Decoupled Synthesis of Light and Heavy Neutron-Rich Nuclei. *The Astrophysical Journal, 777*, 169.

Amelin, Y., Krot, A.N., Hutcheon, I.D., & Ulyanov, A.A. (2002). Lead isotopic ages of chondrules and calcium-aluminum-rich inclusions. *Science, 297*, 1678-1683.

Amelin, Y., Connelly, J., Zartman, R. E., Chen, J. H., Göpel, C., & Neymark, L. A. (2009). Modern U–Pb chronometry of meteorites: Advancing to higher time resolution reveals new problems. *Geochimica et Cosmochimica Acta, 73(17),* 5212-5223.

Amelin, Y., Kaltenbach, A., Iizuka, T., Stirling, C.H., Ireland, T.R., Petaev, M., & Jacobsen, S.B., (2010). U–Pb chronology of the Solar System's oldest solids with variable 238U/235U. *Earth and Planetary Science Letters, 300*, 343-350.

Anders, E., & Zinner, E. (1993). Interstellar grains in primitive meteorites: Diamond, silicon carbide, and graphite*. Meteoritics, 28*, 490-514.

Andreasen, R., Sharma, M., (2006). Solar nebula heterogeneity in *p*-process samarium and neodymium isotopes. *Science, 314*, 806-809.

Aoudjahane, H. C., Avice, J., Barrat, J. A., Boudouma, A., Chen, G., Duke, M. J. M., Franchi, I. A., Gattacecca, J., Grady, M. M., Greenwood, R. C., Herd, C. D. K., Hewins, R., Jambon, A., Marty, B., Rochette, P., Smith, C. L., Sautter. V., Verchovsky, A., Weber, P., & Zanda, B. (2012). Tissint martian meteorite: A fresh look at the interior, atmosphere and surface of Mars. *Nature, 338*, 785-788.

Arlandini, C., Käppeler, F., Wisshak, K., Gallino, R., Lugaro, M., Busso, M., & Straniero, O. (1999). Neutron capture in low-mass asymptotic giant branch stars: cross sections and abundance signatures. *The Astrophysical Journal, 525*, 886.

Aubaud, C., Withers, A. C., Hirschmann, M. M., Guan, Y., Leshin, L. A., Mackwell, S. J., & Bell, & D. R. (2007). Intercalibration of FTIR and SIMS for hydrogen

measurements in glasses and nominally anhydrous minerals. *American Mineralogist, 92(5-6)*, 811-828.

Bake,r V. R. (1982). The channels on Mars. University of Texas Press, Austin.

Balsiger, H., Altwegg, K., & Geiss, J. (1995). D/H and $^{18}O/^{16}O$ ratio in the hydronium ion and in neutral water from in situ ion measurements in comet Halley. *Journal of Geophysical Reviews*, *100,* 5827–5834.

Balta, J. B., Sanborn, M. E., Udry, A., Wadhwa, M., & McSween, H. Y. (2015). Petrology and trace element geochemistry of Tissint, the newest shergottite fall. *Meteoritics & Planetary Science, 50(1)*, 63-85.

Basu Sarbadhikari, A., Day, J. M. D., Liu, Y., Rumble, D., & Taylor, L. A. (2009). Petrogenesis of olivine-phyric shergottite Larkman Nunatak 06319: Implications for enriched components in martian basalts. *Geochimica et Cosmochimica Acta, 73(7),* 2190-2214.

Baziotis, I. P., Liu, Y., DeCarli, P. S., Melosh, H. J., McSween, H. Y., Bodnar, R. J., & Taylor, L. A. (2013). The Tissint martian meteorite as evidence for the largest impact excavation. *Nature Communications, 4*, 1404.

Beck, P., Ferroir, T., & Gillet P. (2007). Shock-induced compaction, melting, and entrapment of atmospheric gases in Martian meteorites. *Geophysical Research Letters, 34*, L01203.

Beckers, J. M., (1975). A search for deuterium on the Sun. *The Astrophysical Journal*, *195*, L43-L45.

Bindeman, I. N., Kamenetsky, V. S., Palandri, J., & Vennemann, T. (2012). Hydrogen and oxygen isotope behaviors during variable degrees of upper mantle melting: Example from the basaltic glasses from Macquarie Island. *Chemical Geology, 310-311*, 126-136.

Birck, J.L., & Allègre, C.J., (1985). Evidence for the presence of ^{53}Mn in the early Solar System. *Geophysical Research Letters, 12*, 745-748.

Birck, J.L. (2004). An overview of isotopic anomalies in extraterrestrial materials and their nucleosynthetic heritage. *Reviews in Mineralogy and Geochemistry, 55*, 25-64.

Biver, N., Bockelée-Morvan, D., Crovisier, J., Lis, D. C., Moreno, R., Colom, P., Henry, F., Herpin, F., Paubert, G., & Womack, M. (2006). Radio wavelength molecular observations of comets C/1999 T1 (Mc Naught- Hartley), C/2001 A2 (LINEAR) and 153/P Ikeya-Zhang. *Astronomy and Astrophysics*, *449*, 1255–1270.

Bizzarro, M., Baker, J.A., & Haack, H. (2004). Mg isotope evidence for contemporaneous formation of chondrules and refractory inclusions. *Nature, 431*, 275-278.

Bjoraker, G. L., Mumma, M. J., & Larson, H. P. (1989). Isotopic abundance ratios for hydrogen and oxygen in the martian atmosphere. *Bulletin of American Astronomical Society*, *21*, 991.

Bockelée-Morvan, D., Gautier, D., Lis, D. C., Young, K., Keene, J., Phillips, T., Owen, T., Crovisier, J., Goldsmith, P. F., Bergin, E. A., Despois, D., & Wootten, A. (1998). Deuterated water in comet C/1996 B2 (Hyakutake) and its implication for the origin of comets. *Icarus*, *133*, 147–162.

Boctor, N. Z., Alexander, C. M. O'D., Wang, J., & Hauri, E. (2003). The source of water in martian meteorites: Clues from hydrogen isotopes. *Geochimica et Cosmochimica Acta*, *67***,** 3971-3989.

Bogard, D. D., Clayton, R. N., Marti, K., Owen, T., & Turner, G. (2001). Martian volatiles: isotopic composition, origin and evolution. *Chronology and Evolution of Mars, 96***,** 425-458.

Bolser, D., Zega, T.J., Asaduzzaman, A., Bringuier, S., Simon, S.B., Grossman, L., Thompson, M.S., & Domanik, K.J. (2016). Microstructural analysis of Wark-Lovering rims in the Allende and Axtell CV3 chondrites: Implications for high-temperature nebular processes. *Meteoritics & Planetary Science, 51*, 743-756.

Borg, L. E. & Draper, D. S. (2003). A petrogenetic model for the origin and compositional variation of the martian basaltic meteorites. *Meteoritics and Planetary Science, 38(12)*, 1713-1731.

Bouvier, A., & Wadhwa, M., (2010). The age of the Solar System redefined by the oldest Pb–Pb age of a meteoritic inclusion. *Nature Geoscience, 3*, 637-641.

Bouvier, A., Spivak-Birndorf, L. J., Brennecka, G. A., & Wadhwa, M. (2011). New constraints on early Solar System chronology from Al–Mg and U–Pb isotope systematics in the unique basaltic achondrite Northwest Africa 2976. *Geochimica et Cosmochimica Acta,* 75(18), 5310-5323.

Brandon, A. D., Puchtel, I. S., Walker, R. J., Day, J. M. D., Irving, A. J., & Taylor, L. A. (2012). Evolution of the martian mantle inferred from the ^{187}Re–^{187}Os isotope and highly siderophile element abundance systematics of shergottite meteorites. *Geochimica et Cosmochimica Acta 76*, 206-235.

Brennecka, G.A., Weyer, S., Wadhwa, M., Janney, P.E., Zipfel, J., & Anbar, A.D., (2010). ^{238}U/^{235}U variations in meteorites: extant ^{247}Cm and implications for Pb-Pb dating. *Science, 327*, 449-451.

Brennecka, G.A., Borg, L.E., & Wadhwa, M. (2013). Evidence for supernova injection into the solar nebula and the decoupling of *r*-process nucleosynthesis. *Proceedings of the National Academy of Sciences of the United States of America, 110,* 17241-17246.

Brennecka, G., Borg, L., & Wadhwa, M., (2014a). The Gadolinium and Dysprosium isotopic composition of a supernova injection inferred from Allende CAIs, *Lunar and Planetary Science Conference*, 2280.

Brennecka, G. A., Borg, L. E., & Wadhw,a M. (2014b). Insights into the Martian mantle: The age and isotopics of the meteorite fall Tissint. *Meteoritics & Planetary Science 49(3*), 412-418.

Burkhardt, C., Kleine, T., Oberli, F., Pack, A., Bourdon, B., & Wieler, R. (2011). Molybdenum isotope anomalies in meteorites: constraints on solar nebula evolution and origin of the Earth. *Earth and Planetary Science Letters, 312,* 390-400.

Burles, S., Nollett, K.M., & Turner, M.S. (2001). Big bang nucleosynthesis predictions for precision cosmology. *The Astrophysical Journal*, *552*, L1–L5.

Catanzaro, E. J., Murphy, T. J., Garner, E. L., & Shields, W. R. (1966). Absolute isotopic abundance ratio and atomic weight of Magnesium. *Journal of Research of the National Bureau of Standards - A. Physics and Chemistry, 70A*(6), 6.

Carr, M. H. (1990). D/H on Mars: Effects of floods, volcanism, impacts and polar processes. *Icarus, 87*, 210-227.

Catling, D. C., & Zahnle, K. J. (2009). The planetary air leak. *Scientific American, (May 2009*), 36-43.

Chaffin, M. S., Chaufray, J. Y., Deighan, J., Schneider, N. M., McClintock, W. E., Stewart, A. I. F., Thiemann, E., Clarke, J. T., Holsclaw, G. M., Jain, S. K., & Crismani, M. M. (2015). Three-dimensional structure in the Mars H corona revealed by IUVS on MAVEN. *Geophysical Research Letters, 42*, 9001–9008.

Chaussidon, M., Sheppard, S. M., & Michard, A. (1991). Hydrogen, sulphur and neodymium isotope variations in the mantle beneath the EPR at 12 50'N. In *Stable Isotope Geochemistry: A Tribute to Samuel Epstein No.3, edited by Taylor H. P., O'Neil J. R., and Kaplan I. R. Geochemical Society*, 325-337.

Chen, J., Papanastassiou, D., & Wasserburg, G., (2010). Ruthenium endemic isotope effects in chondrites and differentiated meteorites. *Geochimica et Cosmochimica Acta, 74*, 3851-3862.

Chen, J., Schauer, S., & Hervig, R. (2013). Normal-incidence Electron Gun alignment method for negative ion analysis on insulators by magnetic sector SIMS. Nuclear Instruments and Methods. *Physics Research Section B: Beam Interactions with Materials and Atoms, 295*, 50-54.

Chen, Y., Liu, Y., Guan, Y., Eiler, J. M., Ma, C., Rossman, G. R., & Taylor, L. A. (2015). Evidence in Tissint for recent subsurface water on Mars. *Earth and Planetary Science Letters, 425,* 55-63.

Clayton, R.N., (1993). Oxygen isotopes in meteorites*. Annual Review of Earth and Planetary Sciences, 21*, 115-149.

Clayton, R.N., Grossman, L., & Mayeda, T.K., (1973). A component of primitive nuclear composition in carbonaceous meteorites. *Science, 182*, 485-488.

Clog, M., Aubaud, C., Cartigny, P., & Dosso, L. (2013). The hydrogen isotopic composition and water content of southern Pacific MORB basalt: a reassessment of

the D/H ratio of the depleted mantle reservoir. *Earth and Planetary Science Letters*, *381*, 156-165.

Connelly, J.N., Bizzarro, M., Krot, A.N., Nordlund, A., Wielandt, D., & Ivanova, M.A. (2012). The absolute chronology and thermal processing of solids in the solar protoplanetary disk. *Science, 338*, 651-655.

Connerney, J. E. P., Acuña, M. H., Wasilewski, P. J., Kletetschka, G., Ness, N. F., Rème, H., Lin, R. P., & Mitchell, D. L. (2001). The global magnetic field of Mars and implications for crustal evolution. *Geophysical Research Letter*, *28*, 4015-4018.

Cosarinsky, M., McKeegan, K., Hutcheon, I., Weber, P., & Fallon, S., (2005). Magnesium and oxygen isotopic study of the Wark-Lovering Rim around a fluffy type-A inclusion from Allende, *36th Annual Lunar and Planetary Science Conference*, 2105.

Crozaz, G., & Wadhwa, M. (2001). The terrestrial alteration of Saharan Shergottites Dar al Gani 476 and 489: A case study of weathering in a hot desert environment. *Geochimica et Cosmochimica Acta, 65(6)*, 971-978.

Dauphas, N. & Pourmand, A. (2011). Hf-W-Th evidence for rapid growth of Mars and its status as a planetary embryo. *N*ature, *473(7348),* 489-92.

Davis, A.M., MacPherson, G.J., & Hinton, R.W. (1986). Rims revealed-ion microprobe analysis of individual rim layers in a Vigarano type A inclusion. *Meteoritics, 21,* 349.

Davis, A., Simon, S., & Grossman, L. (1994). Alteration of Allende type B1 CAIs: When, where, and how, *Lunar and Planetary Science Conference*, 315.

Davis, A., Pellin, M., Lewis, R., Amari, S., & Clayton, R., (1999). Molybdenum and Zirconium isotopic compositions of supernova grains. *Meteoritics and Planetary Science Supplement, 34*, A30.

Davis, A. M., Richter, F. M., Mendybaev, R. A., Janney, P. E., Wadhwa, M., & McKeegan, K. D. (2015). Isotopic mass fractionation laws for magnesium and their effects on ^{26}Al–^{26}Mg systematics in solar system materials. *Geochimica et Cosmochimica Acta, 158*, 245-261.

De Hoog, J. C. M., Taylor, B. E., & Van Bergen, M. J. (2009). Hydrogen isotopic systematics in degassing basaltic magma and applications to Indonesian arc basalts. *Chemical Geology, 266*, 256-266.

Debaille, V., Yin, Q. Z., Brandon, A. D., & Jacobsen, B. (2008). Martian mantle mineralogy investigated by the ^{176}Lu–^{176}Hf and ^{147}Sm–^{143}Nd systematics of shergottites. *Earth and Planetary Science Letters, 269(1-2),* 186-199.

Deloule, E., Albarède, F., & Sheppard, S.M.F. (1991). Hydrogen isotope heterogeneities in the mantle from ion probe analysis of amphiboles from ultramafic rocks. *Earth and Planetary Science Letters, 105*, 543–553.

Demény, A., Vennemann, T. W., Harangi, S., Homonnay, Z., & Fórizs, I. (2006). H_2O-δD-FeIII relations of dehydrogenation and dehydration processes in magmatic amphiboles. *Rapid Communications in Mass Spectrometry, 20(5)*, 919-925.

Desch, S.J., Morris, M.A., Connolly, H.C., & Boss, A.P., (2012). The importance of experiments: Constraints on chondrule formation models. *Meteoritics & Planetary Science, 47,* 1139-1156.

Donahue, T., Hoffman, J.H., & Watson, A.J. (1982). Venus was wet: a measurement of the ratio of deuterium to hydrogen. *Science*, *216*, 630–633.

Draine, B. T., (2006). Can dust explain variations in the D/H ratio? *Astrophysics in the Far Ultraviolet: Five Years of Discovery with FUSE ASP Conference Series, 348*, Proceedings of the Conference held 2-6 August, 2004 in Victoria, British Columbia, Canada. Edited by G. Sonneborn, H. Moos, and B-G Andersson, 58.

Ebel, D.S., & Grossman, L., (2000). Condensation in dust-enriched systems. *Geochimica et Cosmochimica Acta, 64*, 339-366.

Fahey, A., Goswami, J., McKeegan, K., & Zinner, E. (1987). ^{26}Al, ^{244}Pu, ^{50}Ti, REE, and trace element abundances in hibonite grains from CM and CV meteorites. *Geochimica et Cosmochimica Acta, 51*, 329-350.

Franz, H. B., Kim, S.-T., Farquhar, J., Day, J. M. D., Economos, R. C., McKeegan, K. D., Schmitt, A. K., Irving, A. J., Hoek, J., & Iii, J. D. (2014). Isotopic links between atmospheric chemistry and the deep sulphur cycle on Mars. *Nature, 508(7496),* 364-368.

Frost, M.J., & Symes, R., (1970). A zoned perovskite-bearing chondrule from the Lance meteorite. *Mineralogical Magazine, 37*, 724-725.

Gattacceca, J., Hewins, R. H., Lorand, J.-P., Rochette, P., Lagroix, F., Cournède, C., Uehara ,M., Pont S., Sautter V., Scorzelli R. B., Hombourger C., Munayco P., Zanda B., Chennaoui H., & Ferrière L. (2013). Opaque minerals, magnetic properties, and paleomagnetism of the Tissint Martian meteorite. *Meteoritics & Planetary Science, 48(10*), 1919-1936.

Geiss, J., & Gloecker, G. (1998). Abundances of deuterium and helium in the protosolar cloud. *Space Science Reviews*, *84*, 239-250.

Gillet, P., Barrat, J. A., Deloule, E., Wadhwa, M., Jambon, A., Sautter, V., Devouard, D., Neuville, D., Benzerara, K., & Lesourd, M. (2002). Aqueous alteration in the Northwest Africa 817 (NWA 817) Martian meteorite. *Earth and Planetary Science Letters*, 203, 431-444.

Golombek, M.P., Phillips, R.J., Watters, T.R., & Schultz, R.A., (2009). Mars tectonics. 183-232.

Greenwood, J. P., Itoh, S., Sakamoto, N., Vicenzi, E. P., & Yurimoto, H. (2008). Hydrogen isotope evidence for loss of water from Mars through time. *Geophysical Research Letters*, *235*, L05203.

Greenwood, J. P., Itoh, S., Sakamoto, N., Warren, P., Taylor, L., & Yurimoto, H., (2011). Hydrogen isotope ratios in lunar rocks indicate delivery of cometary water to the Moon. *Nature Geoscience, 4*, 80-82.

Grossman, L., (1972). Condensation in the primitive solar nebula. *Geochimica et Cosmochimica Acta, 36,* 597-619.

Grossman, L., (1975). Petrography and mineral chemistry of Ca-rich inclusions in the Allende meteorite. *Geochimica et Cosmochimica Acta, 39,* 433-454.

Grossman, L., Davis, A., Olsen, E., & Santoliquido, P., (1977). Chemical studies of condensates in the Murchison Type 2 carbonaceous chondrite, *Lunar and Planetary Science Conference.*

Grossman, L., & Steele, I.M., (1976). Amoeboid olivine aggregates in the Allende meteorite. *Geochimica et Cosmochimica Acta, 40,* 149-155.

Hallis, L. J., Taylor, G. J., Nagashima, K., & Huss, G. R. (2012a). Magmatic water in the martian meteorite Nakhla. *Earth and Planetary Science Letters, 359-360,* 84-92.

Hallis, L. J., Taylor, G. J., Nagashima, K., Huss, G. R., Needham, A. W., Grady, M. M., & Franchi, I. A. (2012b). Hydrogen isotope analyses of alteration phases in the nakhlite martian meteorites. *Geochimica et Cosmochimica Acta, 97*, 105-119.

Hallis, L. J., Huss, G. R., Nagashima, K., Taylor, G. J., Stöffler, D., Smith, C. L., & Lee, M. R. (2014). D/H and Water Sources in Tissint (abstract). *Meteoritics and Planetary Science, 1800 (suppl.),* 5149.pdf.

Hallis, L. J., Huss, G. R., Nagashima, K., Taylor, G. J., Halldórsson, S. A., Hilton, D. R., Mottl M. J., & Meech, K. J. (2015). Evidence for primordial water in Earth's deep mantle. *Science, 350(6262*), 795-797.

Harper, Jr, C.L. (1996). Evidence for ^{92}Nb in the early solar system and evaluation of a new p-process cosmochronometer from ^{92}Nb/^{92}Mo. *The Astrophysical Journal, 466,* 437.

Hartogh, P., Lis, D. C., Bockelée-Morvan, D., Val-Borro, M. d., Biver, N., Küppers, M., Emprechtinger, M., Bergin, E. A., Crovisier, J., Rengel, M., Moreno, R., Szutowicz, S., & Blake, G. A., (2011). Ocean-like water in the Jupiter-family comet 103P/Hartley 2. *Nature*, *478,* 218-220.

Hauri, E. H., Wang, J., Dixon, J. E., King, P. L., Mandeville, C., & Newman, S. (2002). SIMS analysis of volatiles in silicate glasses 1. Calibration, matrix effects and comparisons with FTIR. *Chemical Geology, 183*, 99-114.

Hauri, E. H., Gaetani, G. A., & Green, T. H. (2006). Partitioning of water during melting of the Earth's upper mantle at H_2O-undersaturated conditions. *Earth and Planetary Science Letters, 248(3*), 715-734.

Herd, C. D. K., Borg, L. E., Jones, J. H., & Papike, J. (2002). Oxygen fugacity and geochemical variations in the martian basalts: Implications for martian basalt

petrogenesis and the oxidation state of the upper mantle of Mars. *Geochimica et Cosmochimica Acta, 66(11)*, 2025-2036.

Hinton, R. (1990). Ion microprobe trace-element analysis of silicates: Measurement of multi-element glasses. *Chemical Geology*, 83, 11-25.

Hirai, K., Ushikubo, T., & Hiyagon, H. (2002). Distribution of Oxygen Isotopes in the Wark-Lovering Rims in CAIs, *Lunar and Planetary Science Conference*, 1494.

Honma, H., Kusakabe, M., Kagami, H., Iizumi, S., Sakai, H., Kodama, Y., & Kimura, M. (1991). Major and trace element chemistry and D/H, $^{18}O/^{16}O$, $^{87}Sr/^{86}Sr$ and $^{143}Nd/^{144}Nd$ ratios of rocks from the spreading center of the Okinawa Trough, a marginal back-arc basin. *Geochemical Journal, 25(2),* 121-136.

Holden, N.E. (1990) Total half-lives for selected nuclides. *Pure and Applied Chemistry, 62*, 941-958.

Holst, J.C., Olsen, M.B., Paton, C., Nagashima, K., Schiller, M., Wielandt, D., Larsen, K.K., Connelly, J.N., Jørgensen, J.K., & Krot, A.N. (2013). $^{182}Hf–^{182}W$ age dating of a ^{26}Al-poor inclusion and implications for the origin of short-lived radioisotopes in the early Solar System. *Proceedings of the National Academy of Sciences, 110,* 8819-8823.

Honma, H., Kusakabe, M., Kagami, H., Iizumi, S., Sakai, H., Kodama, Y., & Kimura, M., (1991). Major and trace element chemistry and D/H, $^{18}O/^{16}O$, $^{87}Sr/^{86}Sr$ and $^{143}Nd/^{144}Nd$ ratios of rocks from the spreading center of the Okinawa Trough, a marginal back-arc basin. *Geochemical Journal, 25*, 121-136.

Hsu, W., Wasserburg, G.J., & Huss, G.R. (2000). High time resolution by use of the ^{26}Al chronometer in the multistage formation of a CAI. *Earth and Planetary Science Letters, 182,* 15-29.

Hu, S., Lin, Y., Zhang, J., Hao, J., Feng, L., Xu, L., Yang, W., & Yang, J. (2014). NanoSIMS analyses of apatite and melt inclusions in the GRV 020090 Martian meteorite: Hydrogen isotopic evidence for recent past underground hydrothermal activity on Mars. *Geochimica et Cosmochimica Acta, 140*, 321-333.

Hughes, J. M., Jolliff, B. L., & Gunter, M. E. (2006). The atomic arrangement of merrillite from the Fra Mauro Formation, Apollo 14 lunar mission: The first structure of merrillite from the Moon. *American Mineralogist 91(10),* 1547-1552.

Hughes, J. M., Jolliff, B. L., & Rakovan, J. (2008). The crystal chemistry of whitlockite and merrillite and the dehydrogenation of whitlockite to merrillite. *American Mineralogist, 93(8-9*), 1300-1305.

Hui H., Peslier A. H., Zhang Y., & Neal C. R. (2013). Water in lunar anorthosites and evidence for a wet early Moon. *Nature Geoscience, 6(3),* 177-180.

Hunten, D. M., (1982). Thermal and nonthermal escape mechanisms for terrestrial bodies. *Planetary and Space Science*, *30*, 773-783.

Hunten, D. M., & Donahue, T. M. (1976). Hydrogen loss from terrestrial planets. *Annual reviews of Earth and Planetary Sciences*, *4***,** 265-292.

Hunten, D. M., Pepin, R. O., & Walker, J. C. G. (1987). Mass fractionation in hydrodynamic escape. *Icarus, 69***,** 532-549.

Hutsémekers, D., Manfroid, J., Jehin, E., Zucconi, J.-M., & Arpigny, C., (2008). The OH/^{18}OH and OD/OH isotope ratios in comet C/2002 T7 (LINEAR). *Astronomy Astrophysics*, *490*, L31–L43.

Iizuka, T., Lai, Y.-J., Akram, W., Amelin, Y., & Schönbächler, M. (2016). The initial abundance and distribution of ^{92}Nb in the Solar System. *Earth and Planetary Science Letters, 439*, 172-181.

Ireland, T.R., Fahey, A., & Zinner, E. (1988). Trace-element abundances in hibonites from the Murchison carbonaceous chondrite: Constraints on high-temperature processes in the solar nebula. *Geochimica et Cosmochimica Acta, 52*, 2841-2854.

Irving, A. J., Kuehner, S. M., Tanaka, R., Herd, C. D., Chen, G., & Lapen, T. J. (2012). The Tissint depleted permafic olivine-phyric shergottite: petrologic, elemental and isotopic characterization of a recent martian fall in Morocco. 43rd Lunar and Planetary Science Conference, 2510.

Ito, M., & Messenger, S. (2008). O isotopic mapping of a Wark-Lovering rim in a type A CAI: Constraints on its formation process. *71st Meteoritical Society Meeting*, 5100.

Ito, M., & Messenger, S. (2010a). Thermal metamorphic history of a Ca, Al-rich inclusion constrained by high spatial resolution Mg isotopic measurements with NanoSIMS 50L. *Meteoritics & Planetary Science, 45*, 583-595.

Ito, M., Messenger, S., Keller, L.P., Rahman, Z.U., Ross, D.K., & Nakamura-Messenger, K., (2010b). FIB-NanoSIMS TEM coordinated study of a Wark-Lovering rim in a Vigarano type A CAI. *41st Lunar and Planetary Science Conference, 1177*.

Jacobsen, B., Yin, Q., Moynier, F., Amelin, Y., Krot, A.N., Nagashima, K., Hutcheon, I.D., & Palme, H. (2008). ^{26}Al–^{26}Mg and ^{207}Pb–^{206}Pb systematics of Allende CAIs: Canonical solar initial ^{26}Al/^{27}Al ratio reinstated. *Earth and Planetary Science Letters, 272*, 353-364.

Jakosky, B. M. (1990). Mars atmospheric D/H: Consistent with polar volatile theory? *Journal of Geophysical Reviews*, *95*, 1479-1480.

Jakosky B. M. (1991). Mars volatile evolution: Evidence from stable isotopes. *Icarus, 94***,** 14-31.

Jakosky, B. M., Grebowsky, J. M., Luhmann, J. G., Connerney, J., Eparvier, F., Ergun, R. Halekas J., Larson D., Mahaffy P., Mcfadden J., & Mitchell, D. F. (2015). MAVEN observations of the response of Mars to an interplanetary coronal mass ejection. *Science, 350(6261)*, aad0210.

Johnson, E. (2005). Magmatic water contents recorded by hydroxyl concentrations in plagioclase phenocrysts from Mount St. Helens, 1980-1981. *Geochimica et Cosmochimica Acta Supplement 69*, 743.

Johnson, E. A. (2006). Water in nominally anhydrous crustal minerals: speciation, concentration, and geologic significance. *In Reviews in Mineralogy and Geochemistry, 62(1)*, 117-154.

Johnson, R. E. (2010). Thermally driven atmospheric escape. *The Astrophysical Journal, 716*, 1573-1578.

Kawasaki, N., Itoh, S., Sakamoto, N., & Yurimoto, H. (2016). Chronological study of oxygen isotope composition for the solar protoplanetary disk recorded in a fluffy Type A CAI from Vigarano. *Geochimica et Cosmochimica Acta*.

Kazahaya K., & Matsuo S. (1986). D/H and $^{18}O/^{16}O$ fractionation in NaCl aqueous solution-vapor systems at elevated temperatures. *Terra Cognita*, 6, 262.

Keller, L., Needham, A., & Messenger, S., (2013). A FIB/TEM study of a complex Wark-Lovering rim on a Vigarano CAI. *76th Annual Meteoritical Society Meeting*, 5300.

Kingsley R. H., Schilling J.-G., Dixon J. E., Swart P., Poreda R., & Simons K. (2002). D/H ratios in basalt glasses from the Salas y Gomez mantle plume interacting with the East Pacific Rise: Water from old D-rich recycled crust or primordial water from the lower mantle? *Geochemistry, Geophysics, Geosystems 3(4),* 1-26.

Kita, N., Huss, G., Tachibana, S., Amelin, Y., Nyquist, L., & Hutcheon, I.D. (2005). Constraints on the origin of chondrules and CAIs from short-lived and long-lived radionuclides, *Chondrites and the Protoplanetary Disk*, 558.

Kita, N.T., Nagahara, H., Tachibana, S., Tomomura, S., Spicuzza, M.J., Fournelle, J.H., & Valley, J.W. (2010). High precision SIMS oxygen three isotope study of chondrules in LL3 chondrites: Role of ambient gas during chondrule formation. *Geochimica et Cosmochimica Acta, 74*, 6610-6635.

Krot, A.N., McKeegan, K.D., Leshin, L.A., MacPherson, G.J., & Scott, E.R. (2002). Existence of an ^{16}O-rich gaseous reservoir in the solar nebula*. Science, 295*, 1051-1054.

Kruijer, T., Touboul, M., Fischer-Gödde, M., Bermingham, K., Walker, R., & Kleine, T., (2014a) Protracted core formation and rapid accretion of protoplanets. *Science, 344*, 1150-1154.

Kruijer, T.S., Kleine, T., Fischer-Gödde, M., Burkhardt, C., & Wieler, R., (2014b). Nucleosynthetic W isotope anomalies and the Hf–W chronometry of Ca–Al-rich inclusions. *Earth and Planetary Science Letters 403,* 317-327.

Kuchka, C. R., Herd, C. D. K., & Walton, E. L. (2014). Hematite in Tissint shock melt glass: investigating the possibility of a Martian near-surface component in shergottites. *45th Lunar and Planetary Science Conference*, 2693.

Kulikov, Yu. N., Lammer, H., Lichtenegger, H. I. M., Terada, N., Ribas, I., Kolb, C., Langmayr, D., Lundin, R., Guinan, E. F., Barabash, S., & Biernat, H. K. (2006). Atmospheric and water loss from early Venus. *Planetary and Space Science*, *54, 425-1444.*

Kyser, T. K., & O'Neil J. R. (1984). Hydrogen isotope systematics of submarine basalts. *Geochimica et Cosmochimica Acta, 48,* 2123-2133.

Lammer H., Kasting, J. F., Chassefière, E., Johnson, R. E., Kulikov, Y. N., & Tian, F. (2008). Atmospheric escape and evolution of terrestrial planets. *Space Science Reviews*, *139*, 399-436.

Larsen, K.K., Trinquier, A., Paton, C., Schiller, M., Wielandt, D., Ivanova, M.A., Connelly, J.N., Nordlund, Å., Krot, A.N., & Bizzarro, M. (2011). Evidence for Magnesium isotope heterogeneity in the Solar protoplanetary disk. *The Astrophysical Journal, 735,* L37.

Lécuyer, C., Gillet, P., and Robert, F. (1998). The hydrogen isotope composition of sea water and the global water cycle. *Chemical Geology*, *145*, 249-261.

Lee, T., Papanastassiou, D., & Wasserburg, G. (1976). Demonstration of ^{26}Mg excess in Allende and evidence for ^{26}Al. *Geophysical Research Letters, 3*, 41-44.

Leshin L. A. (2000). Insights into martian water reservoirs from analyses of martian meteorite QUE94201. *Geophysical research Letters*, *27***,** 2017-2020.

Leshin, L. A., Mahaffy, P. R., Webster, C. R., Cabane, M., Coll, P., Conrad, P. G., Archer, P. D. Jr., Atreya, S. K., Brunner, A. E., Buch, A., Eigenbrode, J. L., Flesch, G. J., Franz, H. B., Freissinet, C., Glavin, D. P., McAdam, A. C., Miller, K. E., Ming, D. W., Morris, R. V., Navarro-González, R., Niles, P. B., Owen, T., Pepin, R. O., Squyres, S., Steele, A., Stern, J. C., Summons, R. E., Sumner, D. Y., Sutter, B., Szopa, C., Teinturier, S., Trainer, M. G., Wray, J. J., Grotzinger, J. P., & MSL Science Team (2013). Volatile, isotope and organic analysis of martian fines with the Mars Curiosity Rover. *Science, 341***,** 1238937-1-1238937-9.

Linsky, J. L. (2007). D/H and nearby interstellar cloud structures. *Space Science Reviews*, *130*, 367-375.

Linsky, J. L. (2004). What is (are) the total D/H ratio(s) within 1 kpc of the Sun? *Astrophysics in the Far Ultraviolet: Five Years of Discovery with FUSE*, ed. Sonneborn, Moos, and Andersson, ASP Conference Series, *348***,** 70.

Linsky, J. L. (2002). Atomic deuterium/hydrogen in the galaxy. *Space Science Reviews, 95/96*, 1-12.

Liu, M.-C., Chaussidon, M., Göpel, C., & Lee, T. (2012). A heterogeneous solar nebula as sampled by CM hibonite grains. *Earth and Planetary Science Letters, 327*, 75-83.

Ma, C., Tschauner, O., Beckett, J. R., Liu, Y., Rossman, G. R., Zuravlev, K., Prakapenka, V., Dera, P., & Taylor, L. A. (2015). Tissintite (Ca,Na)$AlSi_2O_6$: a

highly-defective, shock-induced, high-pressure clinopyroxene in the Tissint martian meteorite. *Earth and Planetary Science Letters, 422*, 194-205.

MacPherson, G., Grossman, L., Beckett, J., & Allen, J. (1982). Origin of rims on coarse-grained inclusions in the Allende meteorite, *Lunar and Planetary Science Conference Proceedings,* 1079-1091.

Macpherson, G.J., & Davis, A.M. (1993). A petrologic and ion microprobe study of a Vigarano Type B refractory inclusion: Evolution by multiple stages of alteration and melting. *Geochimica et Cosmochimica Acta, 57*, 231-243.

MacPherson, G.J., Davis, A.M., & Zinner, E.K. (1995). The distribution of aluminum-26 in the early Solar System - A reappraisal. *Meteoritics, 30*, 365-386.

MacPherson, G.J. (2005). Calcium-aluminum-rich inclusions in chondritic meteorites. *Meteorites, Comets and Planets: Treatise on Geochemistry, Volume 1. Edited by AM Davis. Executive Editors: HD Holland and KK Turekian.* ISBN 0-08-044720-1. Published by Elsevier BV, Amsterdam, The Netherlands, 2005, 201 1, 201.

MacPherson, G.J., Bullock, E.S., Janney, P.E., Kita, N.T., Ushikubo, T., Davis, A.M., Wadhwa, M., & Krot, A.N. (2010). Early Solar nebula condensates with canonical, not supracanonical, initial $^{26}Al/^{27}Al$ ratios. *The Astrophysical Journal,* 711, L117-L121.

MacPherson, G.J., Kita, N.T., Ushikubo, T., Bullock, E.S., & Davis, A.M. (2012). Well-resolved variations in the formation ages for Ca–Al-rich inclusions in the early Solar System. *Earth and Planetary Science Letters, 331-332*, 43-54.

MacPherson, G.J. (2014). Calcium–Aluminum-Rich Inclusions *in Chondritic Meteorites. 139-179.*

Mahaffy, P. R., Donahue, T. M., Atreya, S. K., Owen, T. C., & Niemann, H. B. (1998). Galileo probe measurements of D/H and $^{3}He/^{4}He$ in Jupiter's atmosphere. *Space Science Reviews*, *84*, 251-263.

Mahaffy, P. R., Webster, C. R., Stern, J. C., Brunner, A. E., Atreya, S. K., Conrad, P. G., Domagal-Goldman, S., Eigenbrode, J. L., Flesch, G. J., Christensen, L. E., Franz, H. B., Freissinet, C., Glavin, D. P., Grotzinger, J. P., Jones, J. H., Leshin, L. A., Malespin, C., McAdam, A. C., Ming, D. W., Navarro-Gonzalez, R., Niles, P. B., Owen, T., Pavlov, A. A., Steele, A., Trainer, M. G., Williford, K. H., Wray, J. J., & Team t. M. S. (2015). The imprint of atmospheric evolution in the D/H of Hesperian clay minerals on Mars. *Science, 347(6220*), 412-414.

Mane, P., Romaniello, S., Brennecka, G., Williams, C., & Wadhwa, M. (2014). Zr isotope systematics of Allende CAIs. *LPI Contributions 1800*, 5403.

Mane, P., Torrano, Z., Romaniello, S., Brennecka, G., Shollenberger, Q., Borg, L., & Wadhwa, M. (2016). Zirconium and Chromium Isotopic Systematics of Non-Allende CAIs, *Lunar and Planetary Science Conference*, 2778.

Marti, K., Kim, J., Thakur, A., McCoy, T., & Keil, K. (1995). Signatures of the Martian atmopshere in glass of the Zagami meteorite. *Science, 267(5206),* 1981.

Mason, B., & Taylor, S.R., (1982). Inclusions in the Allende meteorite. Smithsonian *Contributions to the Earth Sciences, 1*, 30.

McCoy, T. J., Corrigan, C. M., & Herd, C. D. (2011). Combining meteorites and missions to explore Mars. *Proceedings of the National Academy of Sciences USA, 108(48)*, 19159-19164.

McCubbin, F. M., Steele, A., Hauri, E. H., Nekvasil, H., Yamashita, S., & Hemley, R. J., (2010). Nominally hydrous magmatism on the Moon. *Proceeding of National Academy of Science*, *27*, 11223-11228.

McCubbin, F. M., Hauri, E. H., Elardo, S. M., Vander Kaaden, K. E., Wang, J., & Shearer, C. K. (2012). Hydrous melting of the martian mantle produced both depleted and enriched shergottites. *Geology, 40(8)*, 683-686.

McCubbin, F. M., Shearer, C. K., Burger, P. V., Hauri, E. H., Wang, J., Elardo, S. M., & Papike, J. J. (2014). Volatile abundances of coexisting merrillite and apatite in the martian meteorite Shergotty: Implications for merrillite in hydrous magmas. *American Mineralogist, 99(7),* 1347-1354.

McCubbin, F. M., Boyce, J. W., Srinivasan, P., Santos, A. R., Elrado, S. M., Filiberto, J., Steele, A., & Shearer, C. K. Heterogeneous distribution of H_2O in the martian interior: Implications for the abundance of H_2O in depleted and enriched mantle sources. *Meteoritics and Planetary Science*.

McElroy, M. B., Prather, M. J., & Rodriguez, J. M., (1982). Escape of hydrogen from Venus. *Science*, *215*, 1614–1615.

McKeegan, K. D., Walker, R. M., & Zinner, E. (1985). Ion microprobe isotopic measurements of individual interplanetary dust particles. *Geochimica et Cosmochimica Acta, 49(9)*, 1971-1987.

McKeegan, K. D., (1987) Ion microprobe measurements of H, C, O, Mg, and Si isotopic abundances in individual interplanetary dust particles. *PhD thesis*, Washington Univ., St. Louis.

McKeegan, K.D., Leshin, L.A., Russell, S.S., & MacPherson, G.J., (1998). Oxygen isotopic abundances in calcium-aluminum-rich inclusions from ordinary chondrites: Implications for nebular heterogeneity. *Science, 280*, 414-418.

McKeegan, K.D., Kallio, A.P.A., Heber, V.S., Jarzebinski, G., Mao, P.H., Coath, C.D., Kunihiro, T., Wiens, R.C., Nordholt, J.E., Moses, R.W., Reisenfeld, D.B., Jurewicz, A.J.G., & Burnett, D.S., (2011). The Oxygen Isotopic Composition of the Sun Inferred from Captured Solar Wind. *Science, 332*, 1528-1532.

McSween H. Y. J. 1994. What we have learned about Mars from SNC meteorites. *Meteoritics, 29*, 757-779.

Meier, R., Owen, T. C., Matthews, H. E., Jewitt, D. C., Bockelée-Morvan, D., Biver, N., Crovisier, J., & Gautier, D., (1998). A determination of the HDO/H_2O ratio in comet C/1995 O1 (Hale-Bopp). *Science*, *279*, 842–844.

Mercer, C., Souders, A., Romaniello, S., Williams, C., Brennecka, G., & Wadhwa, M., (2015). Chromium and Titanium Isotope Systematics of Allende CAIs, *Lunar and Planetary Science Conference, 2920.*

Messenger, S., (2000) Identification of molecular-cloud material in interplanetary dust particles. *Nature*, *404*, 968-971.

Meyer, B., & Zinner, E., (2006). Nucleosynthesis. *Meteorites and the Early Solar System II,* 1, 69-108.

Minister, J., & Ricard, L.P., (1981). The isotopic composition of zirconium. *International Journal of Mass Spectrometry and Ion Physics, 37*, 259-272.

Minitti, M. E., Leshin, L. A., Dyar, M. D., Ahrens, T. J., Guan, Y., & Luo, S.-N. (2008a). Assessment of shock effects on amphibole water contents and hydrogen isotope compositions: 2. Kaersutitic amphibole experiments. *Earth and Planetary Science Letters, 266(3-4)*, 288-302.

Minitti, M. E., Rutherford, M. J., Taylor, B. E., Dyar, M. D., & Schultz, P. H. (2008b). Assessment of shock effects on amphibole water contents and hydrogen isotope compositions: 1. Amphibolite experiments. *Earth and Planetary Science Letters, 266(1-2)*, 46-60.

Morbidelli, A., Chambers, J., Lunine, J. I., Petit, J. M., Robert, F., Valsechhi, J. B., & Cyr, K. E., (2000). Source regions and timescales for the delivery of water to the Earth. *Meteoritics and Planetary Science*, *35,* 1309-1320.

Moos H. W., Cash W. C., Cowie L. L., Davidsen A. F., Dupree A. K., Feldman P. D., Friedman S. D., Green J. C., Green R. F., Gry C., Hutchings J. B., Jenkins E. B., Linsky J. L., Malina R. F., Michalitsianos A. G., Savage B. D., Shull J. M., Siegmund O. H. W., Snow T. P., Sonneborn G., Vidal-Madjar A., Willis A. J., Woodgate B. E., York D. G., Ake T. B., Andersson B-G., Andrews J. P., Barkhouser R. H., Bianchi L., Blair W. P., Brownsberger K. R., Cha A. N., Chayer P., Conard S. J., Fullerton A. W., Gaines G. A., Grange R., Gummin M. A., Hebrard G., Kriss G. A., Kruk J. W., Mark D., McCarthy D. K., Mory C. L., Murowinski R., Murphy E. M., Oegerle W. R., Ohl R. G., Oliveira C., Osterman S. N., Sahnow D. J., Saisse M., Sembach K. R., Weaver H. A., Welsh B. Y., Wilkinson E., & Zheng W., (2000) Overview of the Far Ultraviolet Spectroscopic Explorer Mission. *The Astrophysical Journal Letters*, *538*, L1-L6.

Mosenfelder, J. L., Voyer M. L., Rossman, G. R., Guan, Y., Bell, D. R., Asimow, P. D., & Eiler J. M., (2011). Analysis of hydrogen in olivine by SIMS: Evaluation of standards and protocol. *American Mineralogist, 96(11-12*), 1725-1741.

Münker, C., Weyer, S., Mezger, K., Rehkämper, M., Wombacher, F., & Bischoff, A., (2000). ^{92}Nb-^{92}Zr and the early differentiation history of planetary bodies. *Science, 289*, 1538-1542.

Murrell, M., & Burnett, D., (1986). Spinel-Perovskite Rims: Constraints on the Thermal Histories of Ca-Al Inclusions, *Lunar and Planetary Science Conference,* 589-590.

Newman, S., Epstein, S., & Stolper, E., (1988). Water, carbon dioxide, and hydrogen isotopes in glasses from the ca. 1340 A.D. eruption of the Mono craters, California: Constraints on degassing phenomena and initial volatile content. *Journal of Volcanology and Geothermal Research, 35*, 75-96.

Nicolussi, G.K., Davis, A.M., Pellin, M.J., Lewis, R.S., Clayton, R.N., & Amari, S., (1997). *s*-Process zirconium in presolar silicon carbide grains. *Science, 277*, 1281-1284.

Nicolussi, G.K., Pellin, M.J., Lewis, R.S., Davis, A.M., Clayton, R.N., & Amari, S., (1998). Zirconium and molybdenum in individual circumstellar graphite grains: New isotopic data on the nucleosynthesis of heavy elements. *The Astrophysical Journal, 504*, 492.

Norris, T.L., Gancarz, A.J., Rokop, D.J., & Thomas, K.W., (1983). Half-life of ^{26}Al. *Journal of Geophysical Research, 88*, B331.

Novak, R. E., Mumma, M. J., & Villanueva, G. L., (2011). Measurements of the isotopic signatures of the water on Mars; Implications for studying methane. *Planetary and Space Science*, *59*, 163-168.

Ogliore R. C., Huss G. R., & Nagashima K. (2011). Ratio estimation in SIMS analysis. *Nuclear Instruments and Methods in Physics Research Section B: Beam Interactions with Materials and Atoms, 269(17)*, 1910-1918.

Ohmoto, H., & Skinner, B. J., (1983). The Kuroko and similar volcanogenic massive sulfide deposits. *Economic Geology Monograph*, *5***,** 604.

Ohmoto, H., (1986). Stable isotope geochemistry of ore deposits. *Reviews in Mineralogy, 16***,** 491-560.

Owen, T., Maillard, J. P., de Bergh, C., & Lutz, B. L., (1988). Deuterium on Mars: The abundance of HDO and the value of D/H. *Science, 240*, 1767-1770.

Pathare, A., & Paige, P., (1997). A reexamination of deuterium fractionation on Mars. *Bulletin of American Astronomical Society*, 29.

Pellin, M., Savina, M., Calaway, W., Tripa, C., Barzyk, J., Davis, A., Gyngard, F., Amari, S., Zinner, E., & Lewis, R., (2006). Heavy metal isotopic anomalies in supernovae presolar grains, 37th Annual Lunar and Planetary Science Conference.

Pepin, R. O., (1991). On the origin and early evolution of terrestrial planet atmospheres and meteoritic volatiles. *Icarus, 92***,** 2-79.

Pichavant, M., Herrera, J. V., Boulmie,r S., Briqueu, L., Joron, J. L., Juteau, M., & Vernet, M. (1987). The Macusani glasses, SE Peru: evidence of chemical fractionation in peraluminous magmas. *Magmatic Processes: Physicochemical Principles, 1*, 359-373.

Pineau, F., Shilobreeva, S., Hekinian, R., Bideau, D., & Javoy, M. (2004). Deep-sea explosive activity on the Mid-Atlantic ridge near 34°50'N: a stable isotope (C, H, O) study. *Chemical Geology, 211(1–2)*, 159-175.

Poreda R., Schilling J. G., & Craig H. (1986). Helium and hydrogen isotopes in ocean-ridge basalts north and south of Iceland. *Earth and Planetary Science Letters, 78(1)*, 1-17.

Rehkämper, M., Schönbächler, M., & Stirling, C.H., (2001). Multiple Collector ICP-MS: Introduction to Instrumentation, Measurement Techniques and Analytical Capabilities. *Geostandards Newsletter, 25*, 23-40.

Richter, F. M., Janney, P. E., Mendybaev, R. A., Davis, A. M., & Wadhwa, M. (2007). Elemental and isotopic fractionation of Type B CAI-like liquids by evaporation. *Geochimica et Cosmochimica Acta, 71*(22), 5544-5564.

Richter, S., Eykens, R., Kühn, H., Aregbe, Y., Verbruggen, A., & Weyer, S., (2010). New average values for the $^{238}U/^{235}U$ isotope ratios of natural uranium standards. *International Journal of Mass Spectrometry, 295*, 94-97.

Robert, F. (2001) The origin of water on Earth. *Science*, *293***,** 1056-1057.

Robert, F. (2006) Solar System deuterium/hydrogen ratio. *Meteorites and the early Solar System II* Editors: Lauretta D. S., McSween H. Y. Jr, 341-351.

Ryerson, F.J., & McKeegan, K.D. (1994). Determination of oxygen self-diffusion in åkermanite, anorthite, diopside, and spinel: Implications for oxygen isotopic anomalies and the thermal histories of Ca-Al-rich inclusions. *Geochimica et Cosmochimica Acta, 58,* 3713-3734.

Saal, A. E., Hauri, E. H., Cascio, M. L., Van Orman, J. A., Rutherford, M. J., & Cooper, R. F., (2008). Volatile content of lunar volcanic glasses and the presence of water in the Moon's interior. *Nature*, *454*, 192-195.

Saal, A. E., Hauri, E. H., Van Orman, J. A., & Rutherford, M. J., (2013). Hydrogen isotopes in lunar volcanic glasses and melt inclusions reveal a carbonaceous chondrite heritage. *Science, 340*, 1317-1320.

Sahijpal, S., & Goswami, J. (1998). Refractory phases in primitive meteorites devoid of ^{26}Al and ^{41}Ca: Representative samples of first solar system solids? *The Astrophysical Journal Letters, 509,* L137.

Sanloup, C., Blichert-Toft, J., Télouk, P., Gillet, P., & Albarède, F., (2000). Zr isotope anomalies in chondrites and the presence of ^{92}Nb in the early Solar System. *Earth and Planetary Science Letters, 184*, 75-81.

Sarafian, A. R., Nielsen, S. G., Marschall, H. R., McCubbin, F. M., & Monteleone, B. D. 2014. Early accretion of water in the inner solar system from a carbonaceous chondrite–like source. *Science, 346(6209),* 623-626.

Savin, M. S., & Epstein S., (1970). The oxygen and hydrogen isotope geochemistry of ocean sediments and shales. *Geochimica et Cosmochimica Acta*, *34*, 43-63.

Schönbächler, M., Rehkamper, M., Halliday, A.N., Lee, D.C., Bourot-Denise, M., Zanda, B., Hattendorf, B., & Gunther, D., (2002). Niobium-zirconium chronometry and early solar system development. *Science, 295*, 1705-1708.

Schönbächler, M., Lee, D.-C., Rehkämper, M., Halliday, A.N., Fehr, M.A., Hattendorf, B., & Günther, D., (2003). Zirconium isotope evidence for incomplete admixing of r-process components in the solar nebula. *Earth and Planetary Science Letters, 216*, 467-481.

Schönbächler, M., Rehkämper, M., Fehr, M.A., Halliday, A.N., Hattendorf, B., & Günther, D., (2005). Nucleosynthetic zirconium isotope anomalies in acid leachates of carbonaceous chondrites. *Geochimica et Cosmochimica Acta, 69*, 5113-5122.

Sharp, Z. D., McCubbin, F. M., & Shearer, C. K. (2013). A hydrogen-based oxidation mechanism relevant to planetary formation. *Earth and Planetary Science Letters, 380*, 88-97.

Sheppard, S. M. F., & Harris, C., (1985) Hydrogen and oxygen isotope geochemistry of Ascension Island lavas and granites: variation with crystal fractionation and interaction with seawater. *Contribution to Mineralogy and Petrology, 91*, 74-81.

Shollenberger, Q., Brennecka, G., & Borg, L., (2015). The Strontium, Barium, Neodymium, and Samarium isotopic compositions of non-Allende CAIs, Lunar and Planetary Science Conference, 2593.

Shollenberger, Q., Brennecka, G., & Borg, L., (2016). Clues to the Isotopic Evolution of the Solar System from Er and Yb in Allende CAIs, *Lunar and Planetary Science Conference*, 1964.

Simon, J.I., Young, E.D., Russell, S.S., Tonui, E.K., Dyl, K.A., & Manning, C.E., (2005). A short timescale for changing oxygen fugacity in the solar nebula revealed by high-resolution ^{26}Al–^{26}Mg dating of CAI rims. *Earth and Planetary Science Letters, 238*, 272-283.

Simon, J.I., Hutcheon, I.D., Simon, S.B., Matzel, J.E., Ramon, E.C., Weber, P.K., Grossman, L., & DePaolo, D.J., (2011). Oxygen isotope variations at the margin of a CAI records circulation within the solar nebula. *Science, 331,* 1175-1178.

Simon, J.I., Matzel, J.E., Simon, S.B., Ross, D.K., Weber, P.K., & Grossman, L., (2016). Oxygen isotopic variations in the outer margins and Wark-Lovering rims of refractory inclusions. Geochimica et Cosmochimica Acta.

Sleep, N. H. (1994). Martian plate tectonics. *Journal of Geophysical Research: Planets*, *99*, 5639-5655.

Spivak-Birndorf L., Wadhwa M., & Janney P. (2009). ^{26}Al–^{26}Mg systematics in D'Orbigny and Sahara 99555 angrites: Implications for high-resolution chronology using extinct chronometers. *Geochimica et Cosmochimica Acta, 73*(17), 5202-5211.

Squyres S. W., (1989). Water on Mars. *Icarus*, *79*, 229-288.

Srinivasan, G., Ulyanov, A., & Goswami, J., (1994). Ca-41 in the early solar system. *The Astrophysical Journal, 431*, L67-L70.

Stanley B. D., Hirschmann M. M., & Withers A. C. (2014). Solubility of COH volatiles in graphite-saturated martian basalts. *Geochimica et Cosmochimica Acta, 129*, 54-76.

Stirling C. H., Andersen M. B., Potter E.-K., & Halliday A. N. (2007). Low-temperature isotopic fractionation of uranium. *Earth and Planetary Science Letters, 264(*1-2), 208-225.

Stroud, R., Zega, T., Cosarinsky, M., & McKeegan, K., (2007). FIB-TEM Investigation of an Allende Type A CAI Interior and the Associated Wark-Lovering Rim, *Chronology of Meteorites and the Early Solar System*, 160-161.

Symes S. J. K., Borg L. E., Shearer C. K., & Irving A. J. (2008). The age of the martian meteorite Northwest Africa 1195 and the differentiation history of the shergottites. *Geochimica et Cosmochimica Acta, 72(6),* 1696-1710.

Tartèse R., Anand M., Barnes J. J., Starkey N. A., Franchi I. A., & Sano Y. (2013). The abundance, distribution, and isotopic composition of Hydrogen in the Moon as revealed by basaltic lunar samples: Implications for the volatile inventory of the Moon. *Geochimica et Cosmochimica Acta, 122,* 58-74.

Taylor B. E., Eichelberger J. C., & Westrich H. R., (1983). Hydrogen isotopic evidence of hydrogen magma degassing during shallow intrusion and eruption. *Nature*, *306*, 541-545.

Taylor B. E., (1986). Magmatic volatiles: isotopic variation of C, H and S. *Reviews in Mineralogy*, *16*, 185-220.

Taylor, B.E., Eichelberger, J.C., & Westrich, H.R., (1983). Hydrogen isotopic evidence of rhyolitic magma degassing during shallow intrusion and eruption. *Nature, 306, 541-545.*

Taylor H. P. Jr., (1979). Oxygen and Hydrogen isotope relationships in hydrothermal mineral deposits. *Geochemistry of hydrothermal ore deposits, 2nd edition*. H. L. Barnes, ed., J Willey and Sons, New York, 236-277.

Tenner T. J, Hirschmann M. M., Withers A. C., & Hervig R. L. (2009). Hydrogen partitioning between nominally anhydrous upper mantle minerals and melt between 3 and 5 GPa and applications to hydrous peridotite partial melting. *Chemical Geology, 262*(1-2), 42-56.

Tenner, T.J., Ushikubo, T., Kurahashi, E., Kita, N.T., & Nagahara, H., (2013). Oxygen isotope systematics of chondrule phenocrysts from the CO3.0 chondrite Yamato 81020: Evidence for two distinct oxygen isotope reservoirs. *Geochimica et Cosmochimica Acta, 102*, 226-245.

Thrane, K., Bizzarro, M., & Baker, J.A., (2006). Extremely brief formation interval for refractory inclusions and uniform distribution of ^{26}Al in the early solar system. *The Astrophysical Journal Letters 646*, L159.

Toppani, A., Libourel, G., Robert, F., & Ghanbaja, J., (2006). Laboratory condensation of refractory dust in protosolar and circumstellar conditions. *Geochimica et Cosmochimica Acta, 70*, 5035-5060.

Travaglio, C., Röpke, F., Gallino, R., & Hillebrandt, W., (2011). Type Ia supernovae as sites of the p-process: two-dimensional models coupled to nucleosynthesis. *The Astrophysical Journal, 739,* 93.

Treiman A. (2003). Chemical compositions of martian basalts (shergottites): Some inferences on basalts formation, mantle metasomatism, and differentiation in Mars. *Meteoritics and Planetary Science, 38(12),* 1849-1864.

Trinquier, A., Elliott, T., Ulfbeck, D., Coath, C., Krot, A.N., & Bizzarro, M., (2009). Origin of nucleosynthetic isotope heterogeneity in the solar protoplanetary disk. *Science, 324*, 374-376.

Tyburczy J. A., Xiaomei X., Ahrens T. J., & Epstein S. (2001). Shock-induced devolatilization and isotopic fractionation of H and C from Murchison meteorite: some implications for planetary accretion. *Earth and Planetary Science Letters 192*, 23-30.

Usui T., Sanborn M., Wadhwa M., & McSween H. Y. (2010). Petrology and trace element geochemistry of Robert Massif 04261 and 04262 meteorites, the first examples of geochemically enriched lherzolitic shergottites. *Geochimica et Cosmochimica Acta, 74(24)*, 7283-7306.

Usui T., Alexander C. M. O. D., Wang J., Simon J. I., & Jones J. H. (2012). Origin of water and mantle–crust interactions on Mars inferred from hydrogen isotopes and volatile element abundances of olivine-hosted melt inclusions of primitive shergottites. *Earth and Planetary Science Letters, 357-358*,119-129.

Usui T., Alexander C. M. O. D., Wang J., Simon J. I., & Jones J. H. 2015. Meteoritic evidence for a previously unrecognized hydrogen reservoir on Mars. *Earth and Planetary Science Letters, 410*, 140-151.

Villanueva G. L., Mumma M. J., Bonev B. P., DiSanti M. A., Gibb E. L., Böhnhardt H., & Lippi M., (2009). A sensitive search for deuterated water in comet 8P/Tuttle. *The Astrophysical Journal Letters*, *690*, L5–L9.

Villeneuve, J., Chaussidon, M., & Libourel, G., (2009). Homogeneous distribution of ^{26}Al in the solar system from the Mg isotopic composition of chondrules. *Science, 325*, 985-988.

Wadhwa M. (2001). Redox State of Mars' Upper Mantle and Crust from Eu Anomalies in Shergottite Pyroxenes. *Science, 291(5508)*, 1527-1530.

Walsh K. J., Morbidelli A., Raymond S. N., O'Brian D. P., & Mandell A.M., (2012) A low mass for Mars from Jupiter's early gas driven migration. *Nature*, *475*, 206-209.

Walton E. L., Sharp T. G., Hu J., & Filiberto J. (2014). Heterogeneous mineral assemblages in martian meteorite Tissint as a result of a recent small impact event on Mars. *Geochimica et Cosmochimica Acta, 140*, 334-348.

Wasserburg, G., Lee, T., & Papanastassiou, D., (1977). Correlated O and Mg isotopic anomalies in Allende inclusions: II. Magnesium. *Geophysical Research Letters, 4*, 299-302.

Watson L. L., Hutcheon I. D., Samuel E., & Stopler E. M., (1994) Water on Mars: clues from deuterium/hydrogen and water contents of hydrous phases in SNC meteorites. *Science*, 265, 86-90.

Wark, D., & Boynton, W.V., (2001). The formation of rims on calcium-aluminum-rich inclusions: Step I—Flash heating. *Meteoritics & Planetary Science, 36*, 1135-1166.

Wark, D.A., & Lovering, J.F., (1977). Marker events in the early evolution of the Solar System: Evidence from rims on Ca-Al-rich inclusions in carbonaceous chondrites. Proc Lunar Sci. Conf. 8th.

Webster C. R., Mahaffy P. R., Flesch G. J., Niles P. B., Jones J. H., Leshin L. A., Atreya S. K., Stern J. C., Christensen L. E., Owen T., Franz H., Pepin R. O., Steele A., & the MSL Science Team (2013). Isotope ratios of H, C and O in CO_2 and H_2O of the martian atmosphere. *Science, 341*, 260-263.

Weyer S., Anbar A. D., Gerdes A., Gordon G. W., Algeo T. J., & Boyle E. A. (2008). Natural fractionation of $^{238}U/^{235}U$. *Geochimica et Cosmochimica Acta,* 72(2), 345-359.

Yin, Q.Z., Jaconsen, S.B., McDonough, & W.F., Horn, I., (2000). Supernova sources and the ^{92}Nb-^{92}Zr p-process chronometer. *The Astrophysical Journal, 536*, L49-L53.

Yoshitake, M., Koide, Y., & Yurimoto, H., (2005). Correlations between oxygen-isotopic composition and petrologic setting in a coarse-grained Ca, Al-rich inclusion. *Geochimica et cosmochimica Acta, 69*, 2663-2674.

Young, E.D., & Galy, A., (2004). The isotope geochemistry and cosmochemstry of magnesium. *Reviews in Mineralogy and Geochemistry, 55*, 197-230.

Yung, Y. L., Wen, J-S., Pinto, J. P., Allen, M., Pierce, K. K., & Paulson, S., (1988) HDO in martian atmosphere: implications for the abundance of crustal water. *Icarus, 76*, 146-159.

Waite J. H., Lewis, W. S., Magee, B. A., Lunine, J. I., McKinnon, W. B., Glein, C. R., Mousis O., Young D. T., Brockwell T., Westlake J., Nguyen M-J., Teolis B. D., Niemann H. B., McNutt R. L. Jr, Perry M., & Ip W.-H., (2009) Liquid water on Enceladus from observations of ammonia and ^{40}Ar in the plume. *Nature*, *460,* 487-490.

Zega, T., Cosarinsky, M., Stroud, R., & McKeegan, K. (2007). FIB-TEM Study of a Wark-Lovering Rim in an Allende Type-A CAI. *Meteoritics and Planetary Science Supplement, 42*, 5289.

Zhang, J., Dauphas, N., Davis, A.M., & Pourmand, A. (2011). A new method for MC-ICPMS measurement of titanium isotopic composition: Identification of correlated isotope anomalies in meteorites. *Journal of Analytical Atomic Spectrometry, 26,* 2197-2205.

Zinner, E., & Crozaz, G. (1986). A method for the quantitative measurement of rare earth elements in the ion microprobe. *International Journal of Mass Spectrometry and Ion Processes, 69*, 17-3.

Zinner, E.K., (2003). Presolar grains. *Treatise on Geochemistry, 1*, 17-39.